Krisztina Zajki-Zechmeister, BSc.

Dynamic Macromolecule Adsorption on Structured Cellulose Surfaces

MASTER'S THESIS

to achieve the university degree of

Diplom-Ingenieur

Master's degree programme: Advanced Materials Science

Submitted to

Graz University of Technology

Supervisor

Ass.Prof. Priv.-Doz. Dipl.-Ing. Dr.techn., Harald Plank

Institute of Electron Microscopy and Nanoanalysis

Co-supervisor

Assoc.Prof. Mag.rer.nat. Dr.rer.nat., Stefan Spirk

Institute of Paper, Pulp and Fibre Technology

Graz, February 2018

AFFIDAVIT

I declare that I have authored this thesis independently, that I have not used other than the declared sources/resources, and that I have explicitly indicated all material which has been quoted either literally or by content from the sources used. The text document uploaded to TUGRAZonline is identical to the present master‘s thesis.

_____ _____

Date Signature

Abstract

Bioprocesses involving macromolecules such as proteins are fundamental for living organisms. One of the most important processes base on antigen-antibody reactions as defence mechanisms in human bodies and living creatures in general. A deep understanding of such processes on surfaces paves the way to numerous applications in life science or medicine. The role of cellulose as a substrate for such applications increases because of its favourable properties. Due to its biocompatibility, disposability, low toxicity and its abundant availability in nature, it represents an interesting alternative to other kinds of substrates. Being highly hydrated, hydrophilic and slightly negatively charged, nonspecific binding of macromolecules, such as proteins, is limited, which is favourable regarding the desire to adsorb only specific molecules in bio sensing applications. In recent years, investigations regarding protein immobilization on model cellulose surfaces have revealed essential insights into the selective tunability of such films. The *in situ* observation of such interactions could complement consisting knowledge, regarding bonding sites and interaction abilities. Furthermore, exploring the possibility to fabricate sensing surfaces on a small scale could result in further nanotechnology applications beyond current concepts. For a long time, electron and / or fluorescence based microscopy have successfully been used for accessing interaction mechanism and their consequences on material systems. However, the former often lacks dynamic studies, while the latter is limited in its lateral resolution. During the last decade, atomic force microscopy (AFM) in liquid environments has attracted significant attention as it enables dynamic studies in close-to-nature conditions with molecular resolution. In this thesis, protein coated cellulosic surfaces are explored. Cellulose thin films are obtained via spin coating of a cellulose derivative, trimethylsilyl cellulose (TMSC), followed by conversion with hydrochloric vapours back to cellulose. The obtained surface is further processed with a linker molecule, carboxymethyl cellulose (CMC), and activated with succimide esters to enhance covalent protein bonding. Adsorption and bonding behaviour of macromolecules are investigated via surface plasmon resonance, contact angle measurements and infrared spectroscopy. Liquid Atomic Force Microscopy is applied for high resolution studies of various modified cellulose thin films and complements spectroscopy results. While the first part demonstrates a reliable and reproducible protocol for irreversibly immobilization of proteins on cellulose, the second part focuses on the fabrication of local cellulose fabrication via focused electron beam induced conversion (FEBIC). The search for the optimal dose led to new insights about spatial cellulose conversion with electrons, laying the groundwork for further investigations. Combining the two main results from this work, fabrication of sub-micron sized, cellulose biosensors comes into reach.

Acknowledgements

First, I would like to thank Prof. DI Dr. Ferdinand Hofer (*Institute of Electron Microscopy; Graz University of Technology*) and Prof. DI Dr. Wolfgang Bauer (*Institute of Paper, Pulp and Fibre Technology; Graz University of Technology*) for the opportunity to write my master in collaboration with both institutes.

Also, I would like to thank my first supervisor Harald Plank, for giving me the opportunity to do my master's thesis in his group. He simultaneously supported me with helpful remarks and inspired discussions and left me room to explore and work autonomously. I am very grateful for his motivation, vast knowledge and guidance. Especially in demanding situations, he had my back and reliably helped me as best he could and he moved mountains to ensure the finishing of this thesis in time. I also really appreciate our nice chats about life in general, during the breaks.

Furthermore, I would like to thank my second supervisor Stefan Spirk, who also welcomed me in his group. Whether with small writing workshops or helpful discussions, he taught me a lot. He also encouraged me to participate in a conference for the first time, giving me the opportunity to get to know the scientific work environment better. Without him, I wouldn't have had the chance to get to know the world and way of work of chemists to this extend. I am very grateful for this experience.

I am very grateful for the help and support from the members of the nanofabrication team. I want to thank Jürgen, who always took the time to help and encourage me. His way of teaching enabled a fast but profound understanding regarding the used devices as well as the fundamental aspects behind them. I also really appreciate the friendship that emerged during the time of my thesis. Also I want to thank Robert, who helped me with the FEBIC measurements. Although he often was busy himself, he took the time to carefully think the experiments through and look for errors with me.

I also would like to thank Harald Fitzek who helped me with the Raman and IR measurements, often times until the evening. His critical interpretation of the data contributed immensely to the quality of the results.

Furthermore, I would like to thank my comrades-in-arms, Jakob, Benedikt and Daniel. I enjoyed their company very much and every fancy Diplomanden-dinner we had. Also a big thank you to everyone else at the FELMI institute I had the opportunity to meet. It was great to work in such an enjoyable environment.

I also would like to thank the people in the AG Spirk. Werner immensely helped me to find my way around the labs. Although he was extremely busy with his own work, I could always turn to him for advice and he answered the 100th chemistry question as patiently as the first ones. Furthermore, I would like to thank Mathias and Michael for helping me in the lab.

I am so grateful to have met the amazing "Munchkins" Carina, Stefanie and Gundula during the course of my thesis. Carinas dedication and limitless helpfulness is much appreciated. From hour long speculating about the peculiarities in SPR spectroscopy to relaxing together after work, I enjoyed every interaction with her. Stefi also helped me kindly in the lab and it was really fun working together with her. Gundula helped me getting started with the SPR and was always supportive when needed. I enjoyed our late night discussions and the cooperative work environment. I am very thankful for the friendship we formed and I am looking forward to many more hilarious ventures.

Additionally, gratitude has to be given to my friends who had to put up with me during the more intense times of my work. I would like to thank Martin and Roman, for always supporting me when needed and

for the lots of amazing adventures we had and hopefully will have in the future. Furthermore, I want to thank Lisa, my perpetual cheerleader who always lifted me up and was there for me, in good was well as challenging times. In addition, I would like to give thanks to Sebastian, who encouraged me to reach out to Harald for a thesis and has helped me with his input during the course of my studies.
Without my friends, the time of my studies would not have been nearly as enjoyable as it was.

Last, but definitely not least, I thank my continually supporting family. Considering the efforts of my parents Laszlo and Zsuzsanna they put into creating the opportunity for me to undertake my studies I want to express my gratitude to them. They not only helped me financially but also with their advice in a variety of questions concerning my professional and personal life. I am proud to be their daughter. Furthermore, I would like to thank my brother Tibor, who I always could count on.

Table of Content

1 Introduction

A major part of bioprocesses in living organisms is based on protein interactions. Many of those processes are the result of a long last evolution in nature and reached a highly mature state. As such, they often act as paradigm in science and technology, which, however, requires an initial understanding of their physical and chemical mechanisms. This master thesis is focused on one small aspect in the bigger context of cellulose-based bio sensing at the micro-, meso- and nanoscale.

The central element of this study is the immobilization of protein macromolecules onto cellulose surfaces. The major driving force behind protein adsorption on surfaces is rooted in entropic effects. On the one hand, adsorbed water molecules and salt ions are released back in solution, resulting in a partial dehydration of the macromolecule as well as the surface. On the other hand structural changes within the dehydrated protein and its's optimization of hydrophilic and hydrophobic interaction with the surface increase the entropy. Covalent attachment can lead to structural changes or denaturation of proteins. In addition, the absorbing amount and likelihood for interaction with other proteins can be influenced, altered and even hindered by the substrate material, its morphology and the inner structure. Successful and defined bonding can only be achieved if both materials fit together in most of the aforementioned aspects. For protein immobilization, cellulose turned out to be a suitable base material. The limited ability for proteins to adsorb on cellulose (selectivity) and the possibility of functionalizing the surface (specificity) can be used as advantage and pave the way towards tuneable substrates for biosensors. While the former stems from the highly hydrated and slightly negatively charged property of cellulose, the latter is achievable by assisted conjugation of suitable linking molecules (carboxymethyl cellulose) and activation with succcimide esters (EDC/NHS). Although cellulose is one of the most abundant material on earth, its direct application is complicated due to structural peculiarities and very challenging routes to bring those materials to the region of interest. Using model cellulose thin films provides a morphologically and chemically defined environment, which can be exploited to study surface interactions and adsorption of proteins. One elegant way to generate thin cellulosic substrates is to employ soluble cellulose derivatives, e.g. trimethylsilyl cellulose (TMSC), generating thin films, e.g. via spin coating followed by a back-conversion into pure cellulose. The latter can be achieved via exposure to acidic vapours, in the specific case of TMSC hydrochloric acid is used for a fast and defined conversion.[1] Hydrolysing the TMSC results in ultra thin and smooth films and entails chemical property changes as well. The wettability of the thin film changes due to having hydrophobic silyl ether as substituents in the case of TMSC and hydrophilic hydroxyl groups in the case of cellulose. Furthermore, both functional groups are infrared sensitive, resulting in a traceable difference in the obtained spectra. Although excellent in applicability and also remarkably simple, back-conversion is done globally. To exploit this technique further, in the context of bio sensing, defined local areas on the macro-, micro- and nanoscale are highly interesting. Different techniques such as using UV etching, masking during the exposure to the acidic vapours and soft lithography in combination with enzymes are reported attempts to down scale the cellulose areas. However, it turned out to be complicated, when feature dimensions get smaller and smaller. An alternative method was introduced by Ganner et al. in 2016, where instead of acidic vapour or photons, electrons are used to locally convert the cellulose derivate back to cellulose. By that, feature sizes in the micro-, meso- and even nano-range was demonstrated in principle, while fundamental processes were not studied in detail. A gap, which is partly closed by this master thesis.

Once the cellulose substrate is prepared and functionalized, accurate characterization of the proteins and their interactions with each other is indispensable. There exists a variety of measurement techniques, which are dedicated for application on sensitive soft matter and even living organisms.

Contact angle measurements represent a method, which allows access to a broad range of relevant thin film characteristics such as hydrophobicity, roughness or surface energy. To access quantitative information about adsorption or interaction behaviour of macromolecules, surface plasmon resonance spectroscopy is a powerful tool. The behaviour of optically excited surface plasmons can be exploited to study kinetics between different molecule species (e.g. surface adsorbed proteins) as well as surface mass concentrations after adsorption. Infrared and Raman spectroscopy are complementary techniques for unraveling chemical peculiarities of bio-based materials although the latter technique is somewhat stressful for the samples as high local temperatures can arise. All of the mentioned techniques found are used in this study as well to gain complementary insights in cellulose film formation and its consecutive surface modification on the route towards protein adsorption. While the aforementioned techniques share the characteristic of being integral methods, atomic force microscopy is often used to access laterally resolved information on surface morphology and correlated surface properties. State-of-the-art machines allow furthermore operation in liquid environments to establish close-to-nature conditions during investigations. Its superb resolution down to the molecular level, is often indispensably needed to complement spectroscopic data for a comprehensive insight in bioprocesses. This master thesis used this technology in almost every stage, which indicates its high relevance although analytically blind.

After introducing materials and techniques in more detail, the study then splits into two parts. First, a protocol is derived, which allows controlled, reliable and reproducible fabrication of a multilayer system starting with cellulose and ending with BSA proteins. Each single step is studied with the full variety of techniques for a comprehensive insight, indispensably needed for every subsequent step performed. The full dataset therefore not only enabled the formulation of the preparation protocol but also give explanation for the underlying formation processes. In the second part, the aspect of local instead of global conversion is in the centre. The main objective of that part is the understanding of the conversion process and reveals a higher complexity as initially thought in 2016 by Ganner et al. By that, a new, more profound baseline is provided on which further research can be built on.

2 Basic Principles

In the first section of this chapter, basic physical considerations are presented to aid understanding of the obtained results. A brief introduction of interatomic forces and how they are used in atomic force microscopy is followed by a description of explanations regarding contact angle measurements and surface plasmon resonance. In the second part, chemical considerations, concerning the used molecules, are presented.

2.1 Basic Physical Considerations

Essential concepts regarding interatomic interactions, contact angle measurements and surface plasmon resonance spectroscopy are explained.

2.1.1 Interatomic Forces in the Context of Atomic Force Microscopy

The distance that is between two particles determines the kind of interaction they are having with one another. In the case of large distances, electromagnetic forces contribute the most to the interaction. At shorter ranges, approximately around 10 nm, attractive forces, manly in the form of Van der Waals forces, cause attraction between the atoms. At distances smaller than 0.2 nm strong repulsive forces occur, because of electron-electron repulsion. The latter two can be described with the Lennard-Jones-Potential, see equation 1.

$$V(r) = \frac{b}{r^{12}} - \frac{a}{r^{6}} \tag{1}$$

where a and b are material specific constants, and r is the interatomic distance. Figure 1 shows a graph of the Lennard Jones Potential.

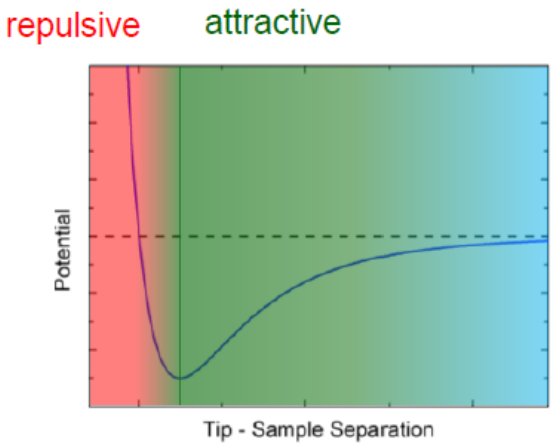

Figure 1: Potential energy versus distance between two atoms (in this case sample atoms and tip atoms). At short distances repulsive forces are present, whereas at a certain length attractive forces are predominant.[2]

Atomic force microscopy uses the force induced by this potential to observe the behaviour of a sharp tip with a surface and recreating an image of it, as explained in 3.3.6. The measurements can be done in attractive or repulsive regime, depending on the specimen, measurement environment and control parameter used. If the measurement happens in the attractive regime, it is called “non contact mode”, if the force applied lays in the repulsive regime, it is called “contact mode”. Besides these static techniques, there is also the possibility to measure dynamically resulting in an intermittent method called “tapping mode”, see 3.3.6.3. As stated there, in tapping mode a change in both, amplitude or phase is measured. The origin of this effect can be described theoretically, by modelling the probe and the surface with a spring system, where the resonance frequency of the undamped cantilever is

$$\omega_0 = \frac{c_0}{m} \tag{2}$$

where c_0 is the spring constant of the free cantilever and m is the mass. The complex potential of surface atoms can be approximated to a harmonic oscillator, and its negative derivative represents a mechanical force in such a paraboloid potential, see the following equations.

$$V = \frac{c*z^2}{2} \qquad \rightarrow F = -\frac{\partial V}{\partial z} = -c * z \tag{3}$$

where V is the potential, c the spring constant, z the distance and F the force. Another derivation leads to the effective spring constant

$$c_{eff} = c_0 - \frac{\partial^2 V}{\partial z^2} \tag{4}$$

Meaning that the 1 dimensional force gradient influences the effective spring constant. To get a better understanding of the force regimes, the surface potential has to be considered in more detail. As mentioned above, the repulsive force stems from electron-electron repulsion and the attractive force from van der Waals forces. The latter consists furthermore of three separate contributing effects: Permanent dipole momentums (polarization), induced dipole momentums (induction) and spontaneous polarization caused by fluctuations in the position of the electrons (dispersion). Looking at equations 3 and 4 and considering that attractive forces translate to positive force gradients, it is evident that a shift of the resonance frequency to smaller value has to follow. Similarly, in the case of repulsive interaction, a negative force gradient results in a resonance frequency shifted to larger values. This means that the change of the frequency at which resonance happens indicates a change of working distance or regime. But the information about which regime one is measuring in is not apparent by only detecting the frequency shift. The change of cantilever phase lag can be measured to access this information, because the sign of the phase shift shows if attractive or repulsive interactions are happening. Both, resonance and phase shift are shown in Figure 2.

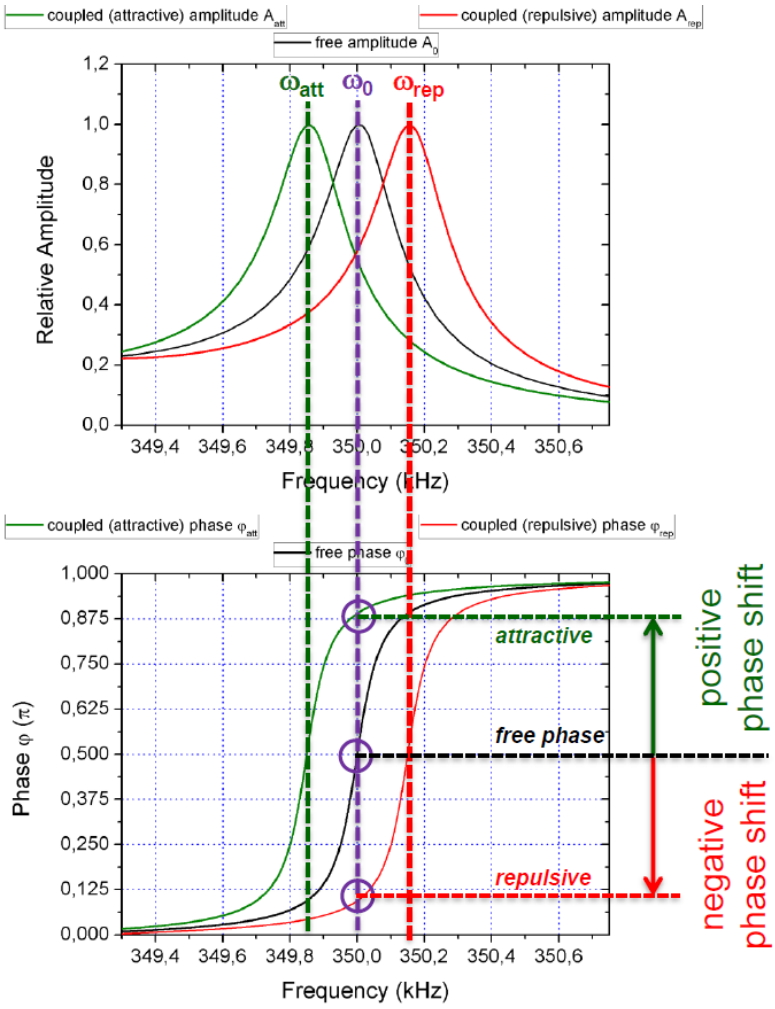

Figure 2: Top: Shift of the resonance frequency due to attractive (green) or repulsive (red) interactions. It is not possible to determine which regime is present by only evaluating the decaying amplitude. Bottom: Shift of the phase lag. Determination of the regime is possible with the sign.[2]

The phase lag can be approximated by following equation

$$\Delta\phi \approx \sqrt{A} * E \tag{5}$$

where A is the average area of contact and E is a material specific constant (effective modulus). Large contact areas occur with soft samples and large effective moduli with hard materials. Therefore, the phase is able to provide more information than just the regime. Distinction between different materials, properties and interaction areas are possible

When working in liquid environment, additional force considerations are necessary. In solution the attractive capillary forces are negligible, instead other effects arise. Because of mobile ions in the solution, which tend to screen charged surfaces, the so-called **electric double layer** results. This affects the interaction between tip and sample immensely. The solution molecules can also cause an oscillation in force due to steric considerations, resulting in the **solvation force**. Figure 3 shows both effects.

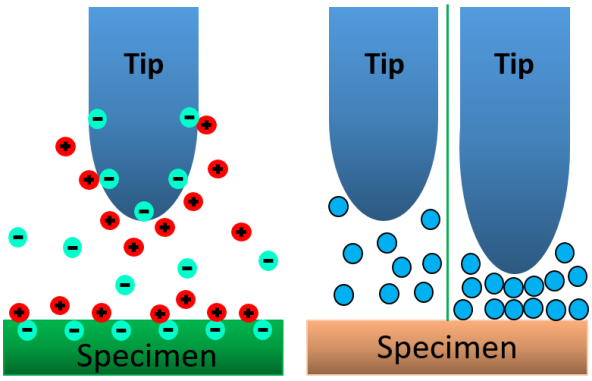

Figure 3: Left: Schematic illustration of the electric double layer force. Right: Schematic depiction of the solvation force.

2.1.2 Liquid Solid Interfaces

Surface tension has its origin in the cohesion energy of surface molecules. In the bulk, the molecules are embedded in their neighbour interactions, but the ones on the surface miss this due to the interface. Energetically, a small interface area of total interface is favoured, explaining why liquids form droplets. The macroscopic consequence is a force acting parallel to the surface to minimize the surface area. If the interface is liquid to gaseous it is called **surface tension**, if it is at a liquid to liquid interface it is called **interfacial tension** and if it is between solid and liquid or solid and gaseous it is called **surface energy**. Their unit is that of energy per unit area, being usually given in mJm^{-2}.

One way to determine the surface energy is to place a liquid droplet onto it and investigate its contact angle. With this angle (θ) the surface tension of the liquid (γ_L) and the interfacial tension between surface and liquid (γ_{SL}) the surface energy is defined through the equation of Young, see equation below.

$$\gamma_S = \gamma_L cos\theta + \gamma_{SL} \tag{6}$$

Figure 4 shows a droplet on a surface schematically, labelled with the parameters from the young equation.

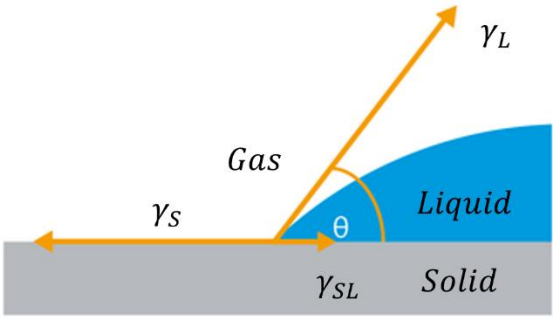

Figure 4: Schematic representation of the variables in the equation of young.[3]

The problem is that only the surface tension of the liquid and the contact angle can be obtained experimentally. Two well established methods are known to work around this problem, namely the method of Zisman and the method of Owens and Wendt. The software used to calculate the surface energies uses the latter, therefore, only this approach is described here.

Owens et al.[4] introduced the separation of acting forces according to their origin. The distinction is made between dispersion forces (d) and hydrogen bonds (h) of the liquid, $\gamma_L = \gamma_L^d + \gamma_L^h$. This results in two cases, either only dispersion forces are present or both. Using again the young equation results in an equation where every variable is known, see formula 7.

$$\gamma_{SL} = \gamma_S + \gamma_L - 2\sqrt{\gamma_S^d \gamma_L^d} \rightarrow cos\theta = 2\sqrt{\gamma_S^d}\frac{\sqrt{\gamma_L^d}}{r\gamma_L} - 1 \quad . \qquad (7)$$

Only the contact angle has to be measured, γ_L and γ_L^d are known for specific liquids. In the case that dispersion and hydrogen bond forces are present, the equation above becomes formula 8.

$$\gamma_{SL} = \gamma_S + \gamma_L - 2\sqrt{\gamma_S^d \gamma_L^d} - 2\sqrt{\gamma_S^h \gamma_L^h} \rightarrow cos\theta = 2\sqrt{\gamma_S^d}\frac{\sqrt{\gamma_L^d}}{r\gamma_L} + 2\sqrt{\gamma_S^h}\frac{\sqrt{\gamma_L^h}}{r\gamma_L} - 1 \qquad (8)$$

Here experiments are needed for θ and γ_L, γ_L^d and γ_L^h are known. Typically, used liquids are water and diiodomethane.

2.1.3 Surface Plasmon Resonance

To generate surface plasmons, free electrons need to be present at an interface of two materials. Because of this requirement, it is apparent that one of this materials should be a metal, providing lots of free conducting electrons. This property results of describing the metal dielectric interface via Maxwell's equation, leading to the possibility to regard surface plasmons as discrete electron densities or electromagnetic waves, propagating along the surface.

Considering a wave refracting at an interface between two media, its k vector can be written as

$$k = \sqrt{k_x^2 + k_y^2 + k_z^2} = \frac{n2\pi}{\lambda} = \frac{n\omega}{c} \qquad (9)$$

with λ being the wavelength, n the refractive index, ω the angular frequency and c the velocity. Choosing the direction of the light beam that $k_z = 0$, leads to an only 2 dimensional problem. The refractive indices of the two media are described with Snell's law

$$n_1 \, sin\alpha = n_2 \, sin\beta \tag{10}$$

where α and β are the incident and resulting angles at an interface and. Figure 5 shows this schematically.

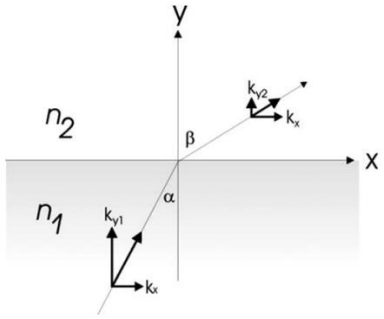

Figure 5: x- and y-component of a wave refracted at an interface between two media.

From this it also can be seen that, $k_{x_1} = k_{x_2} = k_x$, and the wave vector component perpendicular to the surface can be expressed by

$$k_{y_2}^{\,2} = n_1^2 \left(\frac{2\pi}{\lambda}\right)^2 \left(\frac{n_2^2}{n_1^2} - \sin^2\alpha\right) \tag{11}$$

If $n_1 > n_2$, the expression for k_y becomes imaginary, resulting in a wave propagating only parallel along the surface. Its electric field is described as

$$E = E_0 e^{\kappa_{y_2} y} e^{i\omega t - ik_x x} \tag{12}$$

where E_0 is the amplitude and κ the attenuation index. It can be seen, that the amplitude is decreasing exponentially in y direction. With this the depth of penetration can be calculated, which reveals the high sensitivity of the interface because only close to it, the E-field and therefore the changing dielectric property (refractive index) are present. Plasmons are able to generate such an evanescent field, which can be exploited for measurements.

To obtain the dispersion relation for surface plasmons, it is firstly necessary to look at the complex reflection coefficient, described by the means of Fresnel's equation

$$r_P = \frac{E_I}{E_R} = |r_P| e^{i\varphi} = \left|\frac{\tan(\alpha-\beta)}{\tan(\alpha+\beta)}\right| e^{i\varphi} \tag{13}$$

with E_I being the electric field of the incident wave, E_R the reflected field and φ the phase, which is dependent on the refractive indices of the two materials. From this the reflectance can be defined as

$$R_P = |r_P|^2 \tag{14}$$

Looking at the fraction in equation 13, two special cases arise. Either $\alpha + \beta = \frac{\pi}{2}$ causes R_P to become 0 and this describes the occurance of the Brewster angle. Or $\alpha - \beta = \frac{\pi}{2}$ causes R_P to be infinitive, this corresponds to the effect called resonance. From this deduction of the dispersion relation is possible leading to the following equations for the x and y component of the propagating wave.

$$k_x = \frac{\omega}{c}\sqrt{\frac{\varepsilon_1\varepsilon_2}{\varepsilon_1+\varepsilon_2}} \tag{15}$$

$$k_{y_i} = \frac{\omega}{c}\sqrt{\frac{\varepsilon_a^2}{\varepsilon_1+\varepsilon_2}} \tag{16}$$

Here ε_1 and ε_2 are the dielectric constants of the materials and $a = 1, 2$. If medium 2 is a metal and a 3rd medium with low refractive index is introduced. This medium holds a high amount of free electrons and at angular frequencies, which are smaller than the so called plasma frequency ($\omega < \omega_P$), its dielectric constant becomes negative. Both can be found in the following equations.

$$\omega_P = \sqrt{\frac{4\pi n_e e^2}{m_e}} \tag{17}$$

$$\varepsilon(\omega) = 1 - \frac{\omega_P^2}{\omega^2} \tag{18}$$

Where n_e is the free electron density, e is the electron charge and m_e the electron mass. The dielectric constant being negative leads to the implication that no E-field can travel in the metal. Assumed, that $\varepsilon_2 > -\varepsilon_1$, k_{y_i} is imaginary and k_x real, resulting in an wave traveling along the surface. Introducing molecules, which can adsorb on the water/metal interface, it can be considered as replacement of water molecules with the adsorbing ones. Because the new molecules are most likely to have dielectric constants different from water, the properties of the E-field will change, which is detectable.

2.2 Basic Chemical Considerations

In this section, the used molecules and materials are described briefly and characterized.

2.2.1 Cellulose

Cellulose is a versatile and abundant biopolymer found mainly in cell walls of different woody parts of plants, but also in alga and bacteria. Its molecular structure causes different properties and is therefore important to understand. Similar to other polysaccharides, cellulose consists of monosaccharide units, in more detail D-glucose, linked together through glycosidic linkages. Depending on the spatial orientation of these bonds, they can be classified as either α (hydroxyl group on the carbon labelled 1 (C1) is parallel to the hydroxyl group on C6) or β (hydroxyl group of C1 is perpendicular to the hydroxyl group on C6). The former is often associated with energy storage functions, while the latter supports scaffold forming. Being often in cell walls, cellulose has β bonds between the C1 of one glucose unit and the C4 of the neighbouring one (notation: β-D-1→4 Glucose). Figure 6 shows the monosaccharide basic unit with the numbering of the carbons.[5]

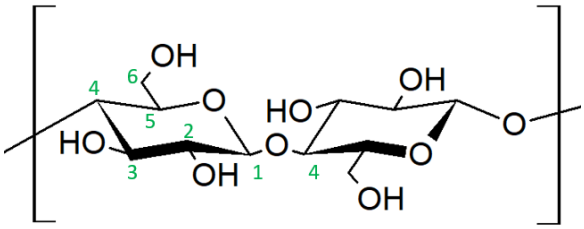

Figure 6: Schematic structure of a cellulose dimer unit.

Linked together, these units form long linear polymer chains, because each has three hydroxyl groups resulting in a high number of hydrogen bonds. This influences its mechanical properties, because parallel arrangement of these chains, lead to a high degree of stability, which is important for the stabilizing element in plants. Besides this crystalline structures, also amorphous ones can be found. The alternating occurrence of crystalline and amorphous structures constitute the so-called elementary fibrils, which lengths are reported to be between 1.5 nm and 3.5 nm. Elementary fibrils again make up microfibrils with reported widths of 10-30 nm and lengths in the range of hundreds of nm.[6] Together with lignin and hemicelluloses, they aggregate to a cellulose fibre which are found in the wall of plant cells. Therefore, this hierarchical structure provides strengths through the crystalline and ordered regions on one hand and flexibility due to the amorphous regions and the mixture of lignin and hemicellulose on the other hand. Figure 7 shows the described structure.

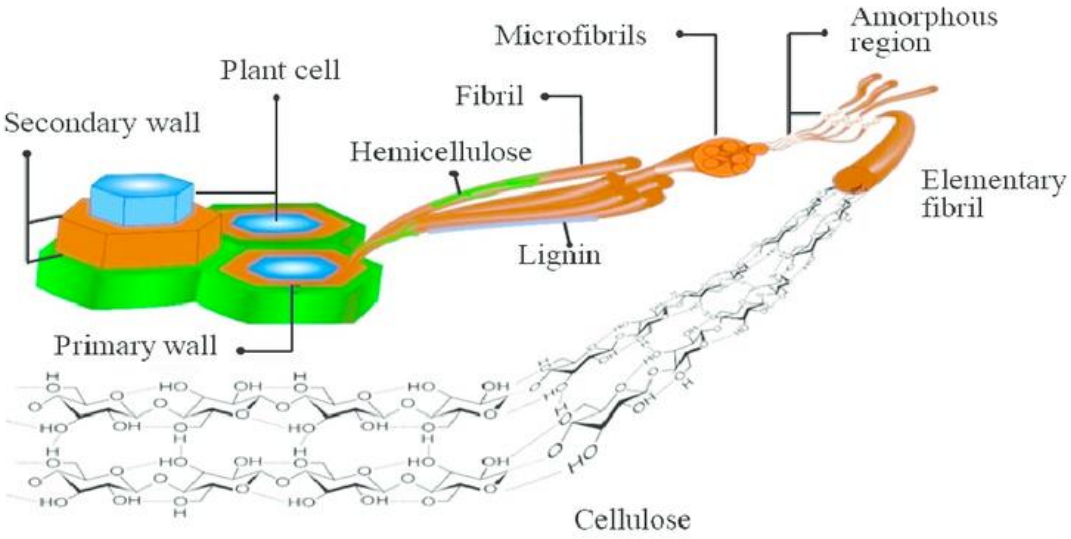

Figure 7: Hierarchical structure of cellulose, reproduced from reference [7].

2.2.2 Cellulose Derivatives

Investigating cellulose is challenging because of its insolubility in water and other often used solvents. One possible work around is to use cellulose derivatives which display the desired dissolution. The main idea is to substitute the hydroxyl groups with another functional group, which prevents interactions between hydrogen bonds. The property "degree of substitution" describes the ratio between the number of substituted hydroxyl groups and the total amount of hydroxyl groups, e.g. a degree of substitution of 1 means one of the three hydroxyl groups is replaced by another functional group One possible substitution is carried out with trimethylsilyl groups. The resulting trimethylsilyl cellulose (TMSC) is soluble in organic solvents such as chloroform, toluene and xylene. The resulting solution can be further employed for spin coating, producing thin and flat surfaces. Followed by the back transformations with acid hydrolysis, a return to formal cellulose is possible.[8] The structure of TMSC can be seen in Figure 8, a.

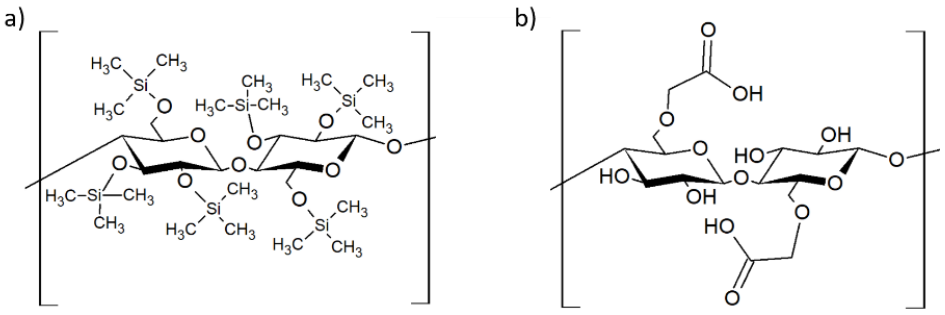

Figure 8: Trimethylsilyl cellulose (a) and carboxymethylcellulose (b).

Another cellulose derivative is carboxymethyl cellulose, where some of the hydroxyl groups are substituted with carboxyl methyl groups. Although it has a wide variety of applications in the food

industry, medicine and textile industry, in this contribution it is used to introduce carboxyl groups on a thin cellulose layer. It is reported to adsorb irreversibly on cellulose in a salt containing solution increasing the negative charge on cellulose fibrils.[9] Its structure can be seen in Figure 8, b.

2.2.3 Bovine Serum Albumin (BSA) and Anti-BSA

Proteins are a special kind of polymers consisting of many amino acids building up an ordered macromolecule structure. They have unique properties and functions utilized in enzymes, antibodies, collagens. Proteins are built with three main components, which are bonded together, forming long chains: Amino groups, carboxyl groups and α-amino acid with varying side chains. Figure 9 shows the fundamental structure.

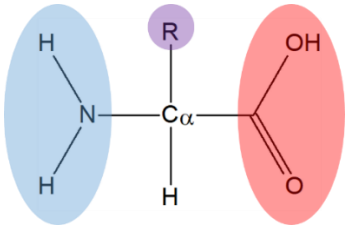

Figure 9: Schematic building blocks of proteins. Amino acids with a rest group (violet) are linked together through peptide bonds between amino groups (blue) and carboxyl groups (red).

The exact sequence of the amino acids is called the primary structure. The secondary structure describes the three dimensional arrangement of these polypeptide chain. The most common structures are α helices and β sheets. The tertiary structure depicts the higher arrangement of the helices and sheets in the protein. The possibility for folding within one protein is 10^N where N is the number of amino acids, but how specific conformations are formed from a polypeptide chain is still unknown. Interactions between charges and the pH value of a given environment have an influence on the folding behaviour. The stability of a tertiary structure is accomplished with different bonds such as ionic bonds, hydrogen bonds and hydrophobic bonding. The adsorption behaviour of proteins onto surfaces is likewise dependent on the charge of the protein and surface, the isoelectric point and the pH value of the solution.

The nature of the peptide bonds enable detector with infrared spectroscopy, because of the copious vibrational modes. Two identifiably bands are classified as amide I and amide II. The first stems from C=O, C=N stretching and N-H bending. The measurable band is a sum of overlapping vibrations related to hydrogen bonding and can be correlated to the proteins secondary structure.[10,11] The latter stems from C-C stretching and is reported to being less sensitive to hydrogen bonds.[10]. Bovine serum albumin (BSA) is a protein found in the blood serum of cattle. Its spheroid dimensions are reported to be 4 nm x 4 nm x 14 nm in solution.[12] Via different techniques such as Raman spectroscopy, infrared spectroscopy and x ray diffraction the secondary structure is described as being conformed of 54 % - 68 % of α-helices.[12,13] These structures lead to a band around 1655 cm^{-1} in infrared spectroscopy. Because the structural stability of BSA is described as moderate, conformational changes can happen during adsorption or bonding on a surface. BSA is commonly used as a protein standard for unspecific adsorption studies. If BSA does not adsorb onto a surface, similar behaviour is expected from other proteins.[14] Anti-BSA is an antibody directly recognizing BSA. This specificity can be exploited in bio sensor applications.[15]

3 Methods

In this section, a detailed description of the used methods can be found. Firstly, the overall approach of building a suitable layer system for protein adsorption is outlined and discussed in detail. The kind of substrates and molecules as well as their appropriate handling are presented in the second part. The measurement techniques used to investigate the prepared samples are described in the last part of this chapter.

3.1 Immobilization Layer Concept

To create highly attractive adsorption sites for investigated proteins, e.g. Bovine Serum Albumin, a multilayer system was built up step by step. The basis of this system is represented by a thin cellulose layer. It represents a suitable substrate for such kind of studies. The highly hydrated hydrogel structure results in unfavourable non-specific interaction for proteins (caused by entropic effects[16]). A commonly used method to create thin films is spin coating. However, this requires the desired substance to be dissolved. Cellulose is difficult to dissolve, it is insoluble in water and in most common organic solvents. To overcome this circumstance, a more soluble cellulose derivate is used in the spin coating process, e.g. Trimethylsilyl cellulose (TMSC), and regenerated back to cellulose. A common procedure to convert TMSC to cellulose is accomplished by careful exposure of TMSC to gaseous hydrochloric acid[17]. Another, more novel method for this conversion is Focused Electron Beam Induced Conversion (FEBIC)[18]. The former approach results in the conversion of the entire surface of the thin film, whereas the latter allows for locally confined regeneration sites, which are quite tuneable in shape and size. Both approaches are used. Figure 10 shows this step schematically.

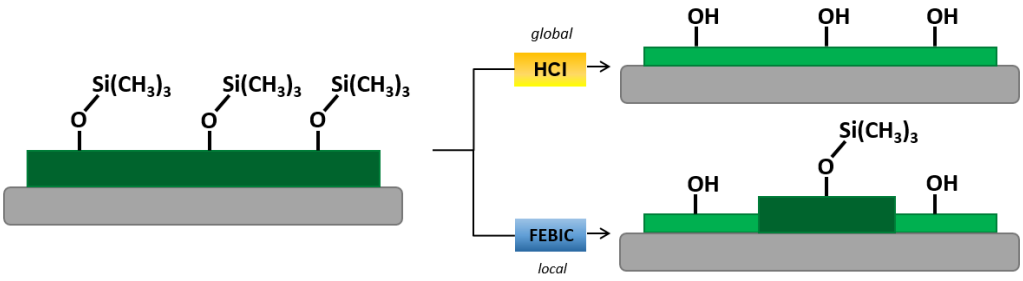

Figure 10: Schematic representation of the two methods for cellulose regeneration from the cellulose derivate Trimethylsilylcellulose. The conversion either is done globally with hydrochloric acid or locally with a focused electron beam.

It is possible to adsorb proteins or other macromolecules on cellulose surfaces, but with low surface concentration densities.[19] Due to the effects of hydration and charging of the cellulose. Therefore, a linker molecule can aid with the conjugation. Hence, in the next step a layer of another cellulose derivate, namely carboxymethyl cellulose (CMC), is deposited on the surface, interacting with the functional groups of the cellulose. At this point sufficient protein bonding would be possible. Through additive elimination, the amide group on the protein would bond itself to the carboxyl group. To promote covalent attachment on the CMC surface, a commonly used method is the crosslinking of immobilization molecules, in this case 1-Ethyl-3-(3-dimethylaminopropyl)carbodiimid (EDC).[20] The

covalent bonds, which can be formed between EDC and proteins, have highly stable physical and chemical characteristics. At this point, an even more enough protein bonding would happen upon exposure. The addition of N-Hydroxysuccinimide (NHS) can furthermore increase the likelihood of bonding events. This ester describes an intermediate which overcomes still present steric limitations and prevents the premature reaction of EDC. This reactive group can interact with the amide group of a protein. With the immobilized protein, in this case BSA, on the surface, the system can be immersed in an aqueous environment, adding its counterpart, anti-BSA. All the steps for the sample preparation are summarized schematically in Figure 11.

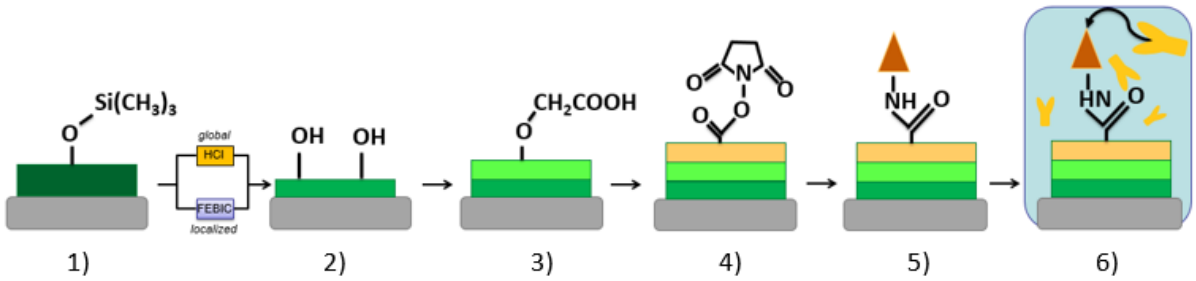

Figure 11: Schematical steps of the sample preparation. 1) Spin coating of TMSC onto a substrate. 2) Regeneration to cellulose, either through HCl or an electron beam. 3) Coating with CMC. 4) Coating with EDC/NHS. 5) Immobilization of the protein, here the antigen Bovine serum albumin (BSA), onto the surface. Exposure to a liquid environment with another protein in solution, here the antibody anti-BSA.

3.2 Used Materials and Molecules

A detailed description of the used materials is presented in this section. The documentation of their handling and purpose is also included.

Trimethylsilyl cellulose (DS = 2.8-3, M_W = 185 000 $gmol^{-1}$, from Avicel) was obtained from Thüringisches Institut für Textil und Kunststoffforschung e. V.. Sodium carboxymethyl cellulose (M_W ~700,000), Chloroform (≥99 %), PVDFC filter (0.45 µm), BSA (≥ 96 %, lyophilized powder), EDC (≥98 %) and NHS (≥98 % (HPLC)) were brought from Sigma Aldrich Austria. Anti-BSA was kindly provided by Dr. Kargl, of the University of Maribor. Xylene (Isomere, ROTIPURAN ≥ 99 %) was purchased from Carl Roth, Toluene from Merck Millipore. MilliQ water (17.8 MΩ at 20 °C) was gotten from a Millipore water purification system. Parafilm (PM-996) was purchased from Bemis. SPR slides (Metal sensor slides AU) were from Cenibra. Conventional silicon substrates were cut and either used directly or sputtered with 10 nm chromium followed by 100 nm gold.

3.2.1 Substrates

The different measurement techniques used for characterization of the samples in this thesis, require different substrate properties.

AFM: For the main parts of the AFM measurements and contact angle measurements, approximately square 1 x 1 cm were cut from a Silicon disc. The roughness of the substrate is heavily influencing these measurement techniques. Therefore, cleansing of the substrates was performed to remove contaminations. The cleaning steps were as follows: Wiping the substrate with an acetone soaked filter paper. Dying with CO_2 or N_2 spaying. Wiping with isopropanol soaked filter paper until no streaks or

particles were visible. Submerging in an isopropanol filled beaker and put in an ultrasonic bath for 20 min. Drying with either CO_2 or N_2 and immediate spin coating of the desired film.

FEBIC: For the FEBIC experiments, which were further investigated by AFM, ATR-IR and Raman spectroscopy, either a pre-cut silicon wafer was handled under a dust free environment or and spin coated directly, or the slide was beforehand sputtered with a 10 nm chromium and 100 nm gold layer.

SPR: The SPR measurements require a specific kind of substrate and dimension (1 x 2 cm) due to the instruments substrate holder. So, purchased, pre-cut substrates from Cenibra were used. The slides were glass substrates sputtered with a chromium and gold layer. It is important to check the slides surface quality before spin coating. Scratches, in particular, on the flow cell area can have a significant and detrimental influence on the measurement results. Therefore, caution when handling the slides with a tweezer was needed, they should be grabbed on the edge. Figure 12 shows a slide with the flow cell areas (a), which must be impeccable and a damaged slide, which cannot be used any more (b).

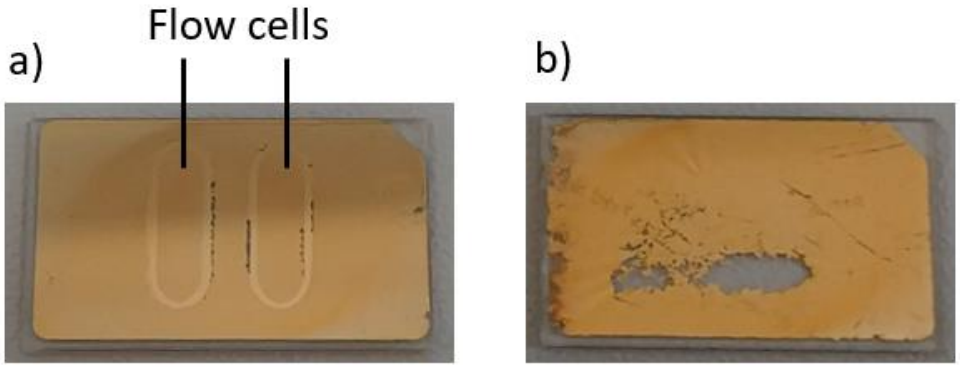

Figure 12: a) SPR slide with the two ellipsoid flow cell areas. b) Damaged slide, which is unsuited for SPR measurement.

The slides were reused and therefore need to be cleaned before every measurement. The gold/chrome layer starts to peel off, which is accelerated by too vigorous cleaning. Such slides were no longer suitable for SPR measurements but can still be used for FT-IR spectroscopy investigations of thin film samples. The cleaning steps, involving "Piranha acid", were as follows. This procedure was used to clean Si substrates as well as SPR slides:

- Mix concentrated H_2SO_4 with 30 % H_2O_2 in a volume ratio 3:1 (2:1 for silicon substrates)
- 6 min in the piranha mixture (15-20 min for silicon substrates)
- Rinsing with purified H_2O → dry with N_2
- 15 min in purified water
- Rinsing with purified H_2O → dry with N_2
- 15 min in purified water (new beaker)
- Ready for spin coating
- Take out of water, immediate dry with N_2

Please note, only stainless-steel tweezers were used, and it was made sure that no organic solvent residues were present. If the slides were not perfectly clean after the treatment, they were carefully wiped with optical tissues and the procedure was repeated. The spin coating process was performed immediately after the cleaning procedure.

3.2.2 Trimethylsilyl Cellulose (TMSC)

TMSC is a white solid powder dissolved in either chloroform, toluene or xylene. For determination of the concentration and needed quantities the volumetric mass density was used. TMSC solutions with all three solvents were produced in volume concentrations of 0.2 %, 0.5 %, 0.75 % and 1 %.
Additionally, solutions of TMSC in xylene were produced with concentrations of 2 %, 2.23 %[18] and 3%. Toluene and xylene have smaller densities and other molecular structures than Chloroform, therefore the thin film properties after spin coating were different (see results 4.4).

Glass vials, which were pre-treated in an oven at 100 °C to remove any residual water, were used as containers for dissolving the biopolymer. They were sealed with parafilm to prevent contamination and put in an ultrasonic bath for 15 - 30 min. As long as the solution contains visible particles, it was left to dissolve, and the ultrasonic bath step was repeated. The homogeneous mixture of TMSC and its solvent is crucial. Otherwise, the concentration becomes not properly defined. The particular batch TMSC used in this thesis dissolves in chloroform quickly, even at higher concentrations. Dissolving in toluene and xylene takes more time and ultrasonic bath steps.

The completely dissolved solution was filtered through a PVDFC filter with a pore size of 0.45 µm to prevent singular large particles having an undesirable impact during spin coating. The filtered solution was ready for spin coating. It can be stored for 2 - 3 days until the TMSC starts to coalesce and re-filtration is needed.

3.2.3 Regeneration to Cellulose

For localized regeneration see chapter 3.3.5. The global regeneration from TMSC to cellulose was done by desilylation with hydrochloric acid (HCl) vapour. The samples were placed in a small petri dish. HCl solution with 12 wght% was placed next to the slides in the container and the lid was closed. After 12 minutes the conversion was finished and the samples can be removed.
The cellulose slides were prepared for the next coating step by immersion in an acetate buffer solution for 12 h. The production steps for 1 L of the 10 mM sodium acetate buffer were as follows:

- Mixture of 1.36 g $NaOAc*3H_2O$ (10 mM) and 5.84 g NaCl (100 mM)
- Add 200 mL purified H_2O
- Adjust with glacial acetic acid until a pH = 4.5 is reached
- Add 800 mL purified H_2O

3.2.4 Carboxymethyl Cellulose (CMC)

Reaction with carboxymethyl cellulose is the first functionalization step on the cellulose surface. This specific biopolymer is chosen due to its properties. A certain interaction between CMC and cellulose originating from the similar structures between the polyelectrolyte and its derivative is reported in literature.[9] The carboxylic groups ensure the possibility of EDC / NHS chemistry. Under correct conditions, it adorbs irreversibly on cellulose by forming hydrogen and glycosidic bonds. Altered swelling and hydrogel like behaviour and hydration status improve the conditions for stable bonding of macromolecules, which prefer more hydrophilic surroundings.

The purification of CMC was carried out as follows. The white CMC powder was dissolved in purified water and dialyzed to remove salts with a dialysis tube in a purified water bath. After 1 h, 5 h and 12 h the bath water was renewed. The dialyzed solution was put in a beaker, covered with aluminium foil and freeze dried until complete sublimation. The wadding like product, the freeze-drying and the dialysis set up can be seen in Figure 13.

Figure 13: 1) Dialysis tube containing the CMC solution in a purified water bath. 2) Freeze drying of the salt free CMC. 3) Wadding like CMC structure after freeze-drying.

The purified CMC was dissolved in an acetate buffer solution with a concentration of 2 g/l. The cellulose film substrates were removed from the buffer bath, dried with N_2 and incubated with the CMC solution. After 20 min the films were carefully washed with buffer solution and dried again with N_2. Further steps were done carefully regarding the use of purified water, because desorption of the CMC layer was observed while rinsing with water.

3.2.5 Amine Coupling with EDC / NHS

Amine coupling is a widely used method to immobilize biomolecules. The preparation of the solution itself is rather straightforward. However, because of their reactiveness, the handling of the chemicals is challenging and yields many possibilities for errors.

EDC (N-(3-Dimethylaminopropyl)-N'-ethylcarbodiimide hydrochloride) is soluble in water, hygroscopic and unstable in air. Therefore, it needs to be stored and handled under inert conditions, e.g. in a glove box. It was weighed in a glass vial and the remaining EDC was stored in the refrigerator at -18 °C in the glove box. After taking the vial out of the glove box, its content was dissolved in water to yield a concentration of 0.04 M and either used immediately or stored at -18 °C. NHS (N-hydroxysuccinimide) was also stored in a glove box for precautionary measures, weighed in, taken out of the box and dissolved in water to a concentration of 0.01 M. A 1:1 mixture of both solutions was produced and ready for usage.[21]

3.2.5.1 EDC / NHS Chemistry

To understand why the amine-coupling step increases the number of chemical reactions with the amine group of the protein, the chemical reactions behind it are described below.
Different electronegativities of the atoms result in slight shifts of the involved electrons. For example, the electrons involved in a bond between oxygen (O) and carbon (C) will be closer to the O atom by a small amount. This causes little charges at the corresponding atoms, a partial negative charge on the O and partial positive charge on the C. If a reaction ("attack"), from another molecule, takes place at an atom with partial negative charge it is called electrophile. If it takes place at a partial positively charged atom, it is called nucleophile. When EDC reacts with the carboxyl group of the CMC, a nucleophilic addition happens. The schematic reaction and its result can be seen in Figure 14.

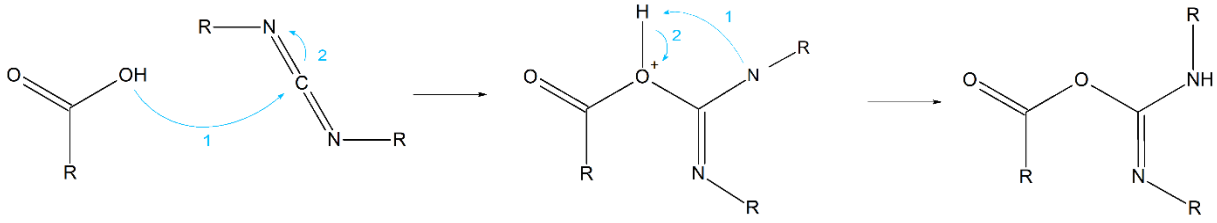

Figure 14: Reaction scheme between EDC and a carboxyl group.

The negatively charged O attacks the partially positive C and they bond. C can never have more than four bonds, therefore the electrons of one bond shift to one of the nitrogens (N). In the next step the N, because of its additional electron, will grab the nearby H, which is partially positively charged because of the O. The O keeps the electron, which was previously shared with the H. This ends the EDC reaction on the CMC surface. Already it would be possible to expose proteins to this new group, Figure 15 shows the reaction.

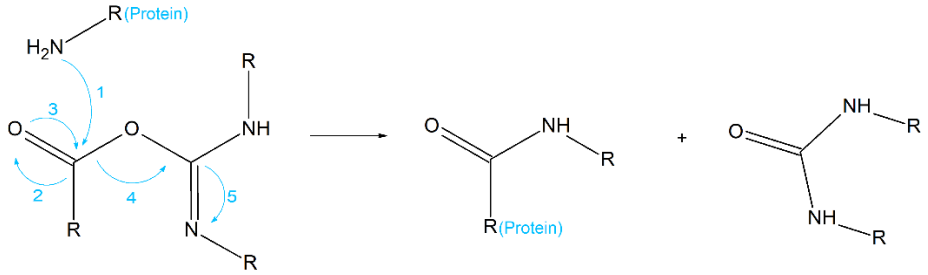

Figure 15: Reaction scheme between a protein and EDC.

The N from the protein attacks the C. One of the double bonds is going to "break" and shift towards the O, which now has three free electron pairs. A temporary tetrahedral state is present, with the amine group, the O with the EDC attachment, the O with three lone pairs and the CMC backbone. This configuration is labile due to the number of electronegative atoms attached to the C. Therefore, one group will leave. One of the three lone pairs reform the double bond resulting in the breaking of the bond between the O-EDC and the C. The newly formed double bond shifts the electrons in the leaving group so that the original double bond is forced to transform to a more stable configuration with an additional H.

Although this reaction already leads to bonding proteins, EDC is not the best choice because of steric considerations. Therefore, an intermediate step, where another leaving group, is introduced with NHS. The reaction can be seen in Figure 16.

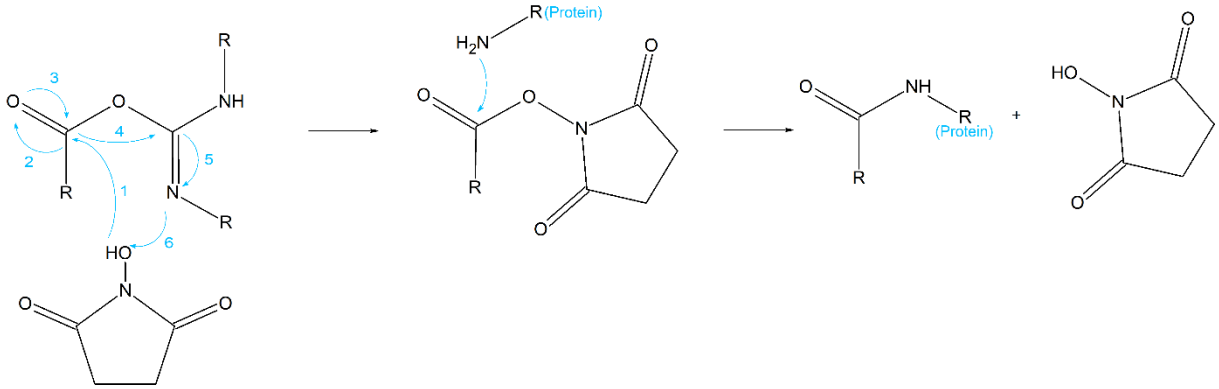

Figure 16: Reaction scheme between NHS and EDC followed by a substitution of a protein.

One of the free electron pairs from the oxygen attacks the central carbon. The electron shift and the structure change coming with it, happens similar as described above. At this point the first leaving group is replaced by the NHS. Again, the primary amide of the protein attacks the central carbon leading to covalent bonding between the oxygen from the carboxyl group and the protein and leaving of the second leaving group. The NHS group is much more reactive than e. g. the carboxyl group on CMC, therefore this step increases the bonding events of proteins on the surface immensely.

3.2.6 Proteins

The proteins used in this research are Bovine Serum Albumin (BSA) and Anti-Bovine Serum Albumin (Anti-BSA). Both protein solutions were prepared by similar methods but with different concentrations. The lyophilized BSA powder was dissolved in the acetate buffer with a concentration of 1 g/l. Anti-BSA was dissolved with a concentration of 50 µg/ml. The proteins are sensitive to too vigorous shaking, therefore, careful handling was required. To assist the dissolution process, gentle rolling of the vial was performed. The remaining protein powders were stored at +4 °C in a refrigerator. The amine activated samples were always incubated with BSA first.

3.3 Instruments and Procedures

In this section the used instruments and their set up is described. Moreover, the measurement procedures are portrayed. A spin coater was used to obtain the initial thin films. Contact angle measurements were carried out to investigate qualitatively the adsorption of the different layers. With infrared and Raman spectroscopy compositional information were gathered. Surface plasmon resonance spectroscopy was used to quantitatively investigate the adsorption of the different molecules. The nanofabrication was accomplished with a Focused Electron Beam. Topological information and dynamic processes were investigated with an atomic force microscope after they were found with a light microscope.

3.3.1 Spin Coating

Spin coating is the most common method to prepare thin films. The desired material is dissolved in a volatile solvent. A substrate, e.g. Si or SPR slide, is placed on the spin coaters chuck, held in place with a vacuum and wetted completely with the solution. The system is rotated. Due to centrifugal forces, the solution is evenly distributed over the substrate. Surplus solution is hurled away. The resulting film is dependent on various properties in four main ways: The materials themselves, concentration and viscosity of the solution as well as the vapour pressure of the used solvent influence the result. The substrates properties like wettability also play a role. And finally, the spin coating parameters itself, namely rotation speed, acceleration and spin time. Whilst analysing spin coated thin films, it is useful to keep some of the inevitable film characteristics in mind: Contaminations can cause comet-like appearance in the film around them. The properties of the thin film change near the edge of the substrate. Usage of not properly cleaned substrates can lead to wavy and uneven films.

In this thesis, two spin coaters were used. Spin coater I (Laurell, North Wales, USA) was used to generate the films used in the FEBIC experiments, spin coater II (Spin150i Spincoating, PUTTEN, The Netherlends) for everything else.

The substrates were dried with N_2 or CO_2 imminent to the spin coating. The slide was put over the suction hole. The vacuum pump was turned on and the solution was pipetted onto the substrate, until it was fully wetted (usually around 150 µl for silicon slides and 200 µl for gold slides). The lid was closed and the coating was run with either a rotational speed of 2500 rpm/s for 60 s or 3500 rpm for 60 s followed by 5000 rpm for 420 s.

3.3.2 Contact Angle Measurement

Static contact angle measurements were performed with a DSA100 drop shape analyser (Krüss, Hamburg, Germany). The sample was positioned between a light source and a camera. Contrast and focus settings were chosen to have a sharp depiction of the substrate. 2 µl of water or diiodomethane were dropped onto the surface. The droplet was recorded with the camera. The evaluation of the contact angle and the concluding surface energy were performed with software (Drop Shape Analysis) using the equations in 2.1.2.

3.3.3 Infrared and Raman Spectroscopy

The ATR-IR measurements of the layers were performed with an ALPHA FT-IR spectrometer (Bruker AXS, Santa Barbara, CA/USA). Every spectrum was measured with 48 scans. The baseline correction was performed with software (OPUS 7.2)

The ATR-IR measurements of the FEBIC structures were performed with a Tensor 27 FT-IR spectroscope (Bruker AXS, Santa Barbara, CA/USA). A single element MCT detector and a 20x ATR (Ge crystal) objective were used. 256 scans were recorded per spectrum. Baseline corrections was carried out with software (OPUS).

The Raman measurements were accomplished with a LabRAM HR 800 microscope (Horiba Jobin Yvon, Bensheim, Germany). The spectra were recorded using an objective with a magnification of 100 and a numerical aperture of 0.9, laser wavelengths of 633 nm and 473 nm and a laser power of 1.6 mW. The accumulation settings were chosen to be 2 s per scan with 16 scans.

3.3.4 Surface Plasmon Resonance Spectroscopy

Different SPR measuring systems can differ based on the optical configuration and level on development, but have in common that there are always three main components: Optics, liquid handling and the sensor chip.[22] Regarding the optical system, its primary goal is to measure the shift of the SPR angle (see 2.1.3). The excitation of the surface plasmons with a laser beam can be achieved through various optical components such as prisms, wave-guides or gratings. Instruments using prisms can either be in the so called Kretschmann, Otto or mixed hybrid configuration.[23] In the Kretschmann configuration, p-polarized light is coupled through a prism on the back of the SPR sensor and reflected onto a light sensitive detector. This specific polarization direction is necessary because only p-polarized light has an E-field perpendicular to the surface which is indispensable for plasmon excitation (s-polarized light would result in total reflection without plasmon excitation). The three most common ways to track the changes in refractive index are reflectivity shift over time, wavelength shift over time and angular shift over time. To obtain these signals different beam structures can be used, namely fixed angle, fan shaped and angular scanning. The device used in this thesis was of the angular scanning type, therefore only this configuration is explained here. With a scanning angle device, a certain broad range of angles can be passed through the laser beam. This is realized with a mirror, controlled to follow the SPR angle. At a particular angle the slide is in resonance.

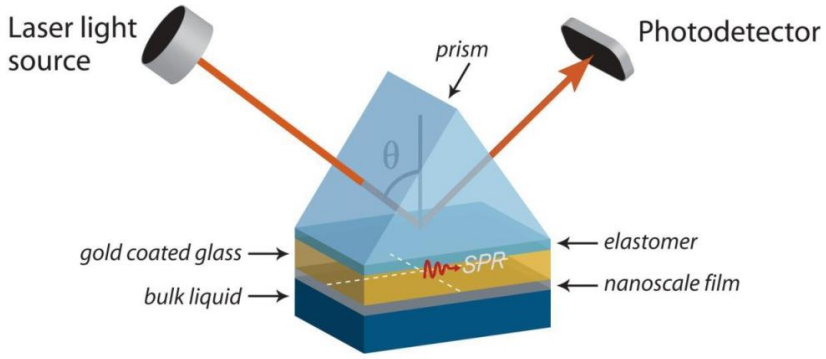

Figure 17: Schematic illustration of the measurement set up in a SPR.[24]

The used sensor was a slide shown in 3.2.1. It consists of several layers. A glass substrate is coated with an adhesion layer, chromium in this case. On top of that, a metal layer, e.g. gold, silver or copper, is coated. In this study only gold coated slides are used. An illustrative SPR intensity curve can be seen in Figure 18.

The angle where the intensity of the reflected laser becomes minimal is called “SPR angle”. At this particular angle, the surface plasmons on the metal layer are in resonance. If the chemical environment changes, so does the energy, which is needed to excite the plasmons into resonance. This phenomenon can be exploited to study adsorption processes, or other mechanisms where the physical chemical environment changes (Figure 18, 1). When measuring in fast fixed angle mode, the steepest slopes are the most sensible parameter that can be tracked (Figure 18, 2). The FWHM (Figure 18, 3), holds information about binding induced light adsorption, which enables investigations concerning coatings. The angle of total internal reflection (Figure 18, 4) contains information about bulk properties and can therefore be taken for the calculation of refractive index increments for different molecules. Tracking the shift of the SPR angle over time during an adsorption experiment, results in a sensorgram. How to evaluate the mass concentration per area is described in chapter 3.3.4.2.

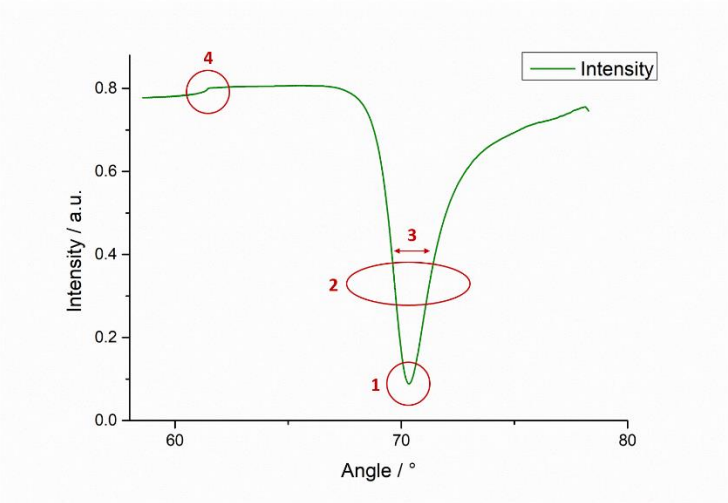

Figure 18: Intensity of the reflected laser beam versus the angle of incidence.

3.3.4.1 SPR Device and Handling

For the surface plasmon resonance measurements a MP-SPR Navi 210A from Bionavis Ltd. was used. It provides two laser wavelengths (λ = 670 nm and λ = 785 nm) and two flow cells. All measurements were performed under the maximum angular range of 39 °- 78 ° with a scanning speed of 8 °s^{-1} and a temperature of 25 °C. As sensor, specific gold slides were used, which are described in 3.2.1. The measurement procedure was carried out according to this: The sample was put in the sample holder. To ensure a dust free back of the sensor, the glass slide was wiped carefully with an isopropanol soaked cleaning tissue and gentle pressure until no visible particles were left. Also, the prism and the flow cells need to be cleaned and were wiped with isopropanol. The sample holder was placed in the device, the flow cell was closed and the temperature was set. An initial scan in air was started to equilibrate the system (the SPR peak should be around 45 °). The buffer pump can be started and was set to a flow rate of 100 µlmin^{-1} to minimize the risk of air bubbles. When the flow cell was completely filled, the angle shifts to angles above 60 °. Equilibration with the used solution, either buffer or high purity water (MilliQ), was achieved by rinsing. As soon as the signal was stable, injection of the analyte can take place, with a flow rate of 20 µlmin^{-1}. After every injection, the surfaces were rinsed with buffer solution again to regain the equilibrated state.

3.3.4.2 Data evaluation

De Feijter et al. described the relation between surface concentration and other surface properties as follows[25]

$$\Gamma = \frac{d*(n_1-n_2)}{\frac{dn}{dc}} \quad (19)$$

where Γ is the adsorbed material concentration on the surface, d is the thickness of the layer, n_1 the refractive index of the absorbed layer, given, that it is in linear relation to the solute concentration, n_2 the refractive index of the medium and $\frac{dn}{dc}$ the refractive index increment of the adsorbed species.

Through calibration of the instrument, a factor can be introduced, correlating angular information with refractive indices, as shown in formula 20

$$\Gamma = \frac{d*k*\Delta\Theta}{\frac{dn}{dc}} \tag{20}$$

where k is the calibration factor, which is only valid for a certain slide and wavelength configuration and Δθ is the shift of the SPR angle during adsorption, which is actually measured. For layers of a thickness below 100 nm, the $d * k$ term can be approximated to be constant[26]. For the used device, the values for water based buffers and gold slides are reported as $1.09 * 10^{-7} \frac{nm}{°}$ for a wavelength of 670 nm and as $1.90 * 10^{-7} \frac{nm}{°}$ for 785 nm.[27] Furthermore the refractive index increment for specific polymers at specific wavelengths can be gathered from literature, resulting in the mass concentration being a function only dependent on the angular shift.

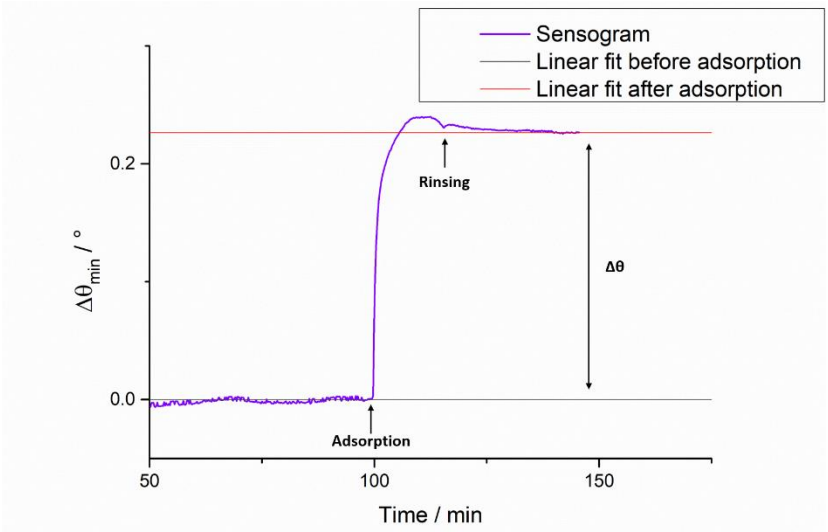

Figure 19: Procedure of the determination of the angular shift by reference to an adsorption experiment.

The measurement happens simultaneously in two different flow cells (FC1 and FC2), with the two laser wavelengths, 670 nm and 785 nm as mentioned above. Figure 19 shows a typical sensorgram of an adsorption measurement. The whole system has to be equilibrated, to ensure a stable measurement environment and base line prior to adsorption. For this, the flow cell is equilibrated with the appropriate buffer until the angular shift falls below ±0.005 ° per 10 minutes. The time the system needs to stabilize can vary between several minutes up to hours. After successful equilibration, the adsorbate can be injected and the shift of the SPR angle observed. If the angle saturates at a certain value, the injection can be stopped and rinsing with the same solution as before starts. Rinsing is an important step to clear the surface of loosely bound molecules. Again, equilibration of the system follows as described above. To determine the angular shift a linear fit is performed before and after adsorption, with lines having the same slope and were evaluated regarding their distance. Inserting the result in equation 20 leads to the estimated surface concentration of the adsorption experiment.
Refractive index increments were taken from literature and can be found in Table 1.

Table 1: List of the literature values for different refractive index increments.
P…Polymer species
RII…Refractive index increment

P	RII / mlg^{-1}
CMC	0.163[28]
BSA	0.187[29]
Anti-BSA	0.187[29]

These reference values are reported for configurations using a laser with a wavelength of 633 nm, therefore they are not completely accurate for the used system. However, the error, introduced through this is much smaller than the error from evaluating the shifted angle, therefore, it is neglected.[30]

3.3.5 Nano-Patterning with Focused Electron Beams

Ganner et al. describe an alternative method to convert TMSC back to cellulose.[18] Instead of using acidic vapours, to cut off the functional groups, electrons are utilized for this. Approaching the regeneration with this Focused Electron Beam Induced Conversion (FEBIC) enables high lateral control over regenerated areas. It has been shown, that electrons cause cleavage events during their transmission through the sample, resulting in radicals, which drive the conversion process. Figure 20 depicts this process schematically. The FEBIC measurements were done with a FIB Nova 200 microscope (FEI, Hillsboro, OR/USA). Figure 21 shows the vacuum chamber of the microscope and an already inserted specimen. The patterning parameters were chosen as follow: The used primary electron energy was 2 keV, the beam current was set to 53 pA. The point pitch was 10.39 nm and the beam overlap was chosen to be 50 %. Squares with defined electron doses were designed in the integrated patterning software of the microscope.

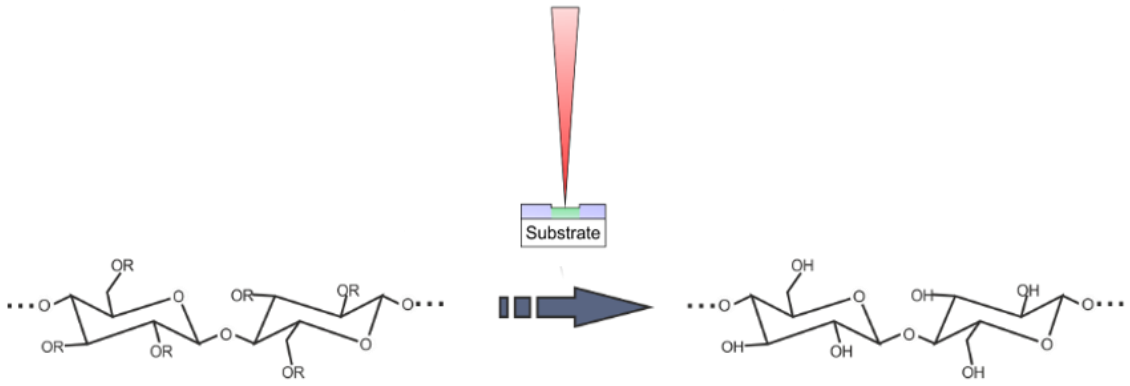

Figure 20: schematic principle of FEBIC. The trimethylsilyl groups are removed via electrons.[2]

The specimen was mounted on a SEM holder and fixed with double sided carbon tape. The holder was positioned inside the microscope and a fast beam blanker with largest aperture size (position 4) was installed. The chamber was pumped until a pressure of approximately $7*10^{-6}$ mbar was reached. Beam focusing/optimization was carefully done on the edge of the substrate to avoid unwanted exposure of the region of interest. However, at 2 keV acceleration voltage, the beam is rather broad and more

difficult to focus. The beam blanker has also an influence on the electron beam, since it is charged over time and then starts to deflect the beam. Nonetheless, the small voltage and the blanker are important, otherwise premature regeneration or over conversion of the TMSC film could happen. The working distance between the sample and the electron cone was 5 mm. Patterning was applied without prior inspection, since any electron could cause regeneration effects.[18] After treatment, the TMSC films were stored in a petri-dish for more characterization steps.

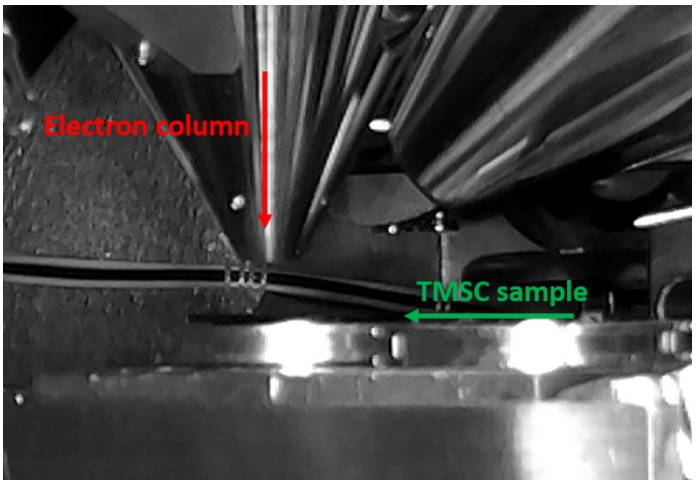

Figure 21: Experimental set up inside the vacuum chamber of the microscope.

3.3.5.1 Calculation of the electron dose and pattering designs

Calculations regarding the electron doses are based on the work of Thomas Ganner.[18] Formula 21 shows the equation.

$$D = \frac{I*t}{A} = \frac{4*\ I_{Beam}*DT*\ P}{A_{Beam}} = \frac{I_{Beam}*DT*P}{A_{POP}} \tag{21}$$

Assuming to be constant over time, the electric charge per area, further denoted as dose (D), is defined as current (I) times time (t) per area (A). Regarding the experimental setting, the dose can also be expressed as four times the current of the beam (I_{Beam}) times the dwell time (DT) times the passes (P) per beam diameter (A_{Beam}). The factor of four is due to the choice of a 50 % beam overlap, leading to 4 passes per beam quadrant. Another possibility is to calculate the dose via the area that is defined through the point pitch (A_{PoP}), which is a quarter of the beam area, also included in equation 21. The number of pixels in a 2 µm x 2 µm square with a point pitch of 10.39 nm corresponds to:

$$Pi = \left(\frac{2000\ nm}{10.39\frac{nm}{pixel}}\right)^2 \approx 193\ pixel \tag{22}$$

With the dwell time of 100 ns, which is defined as the time the electron beam stays on each point, and the current of 53 pA the dose can be calculated:

$$D = \frac{53*10^{-12}*193^2*100*10^{-9}}{4*10^{-12}} = 4.9 * 10^{-2}\,\frac{C}{m^2} \quad (23)$$

Therefore, 4.9 * 10^{-2} Cm^{-2} is the dose for one pass in a 2 µm x 2 µm square. To increase the dose, the number of passes per pixel was increased, so that the overall dose in this area increases. Ranging from 1 to 48 passes, a dose range of 4.9*10^{-2} Cm^{-2} to 2.3 Cm^{-2} can be achieved. As shown in Figure 22, a 4 x 4 array consisting of 16 individual squares with an area of 2 µm x 2 µm was set up Within an array, the dosages were varied from 1 to 16 passes and from 17 to 32 passes, respectively.

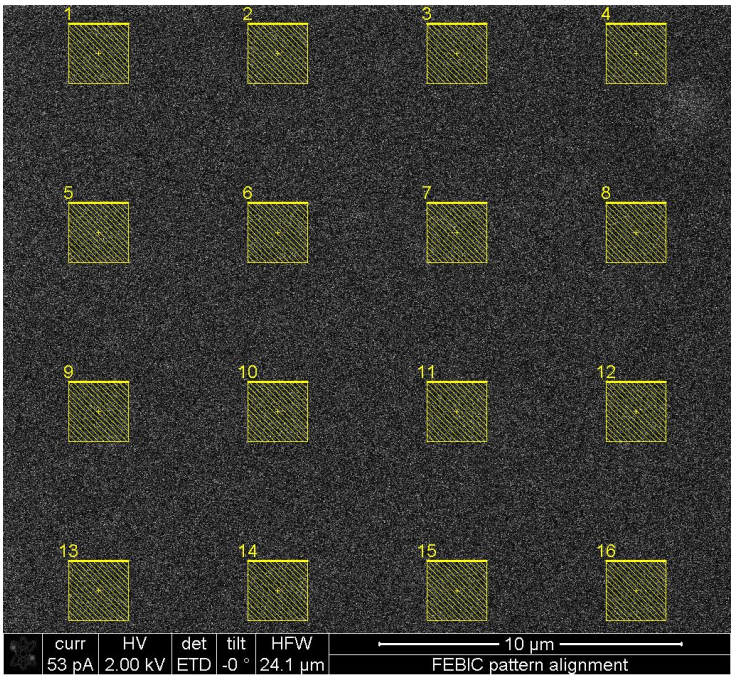

Figure 22: Alingment of 2 µm x 2 µm squares with a spacing of 6 µm (center-to-center)for the FEBIC experiments.

To investigate the conversion gradient, described in 4.7, a pattern was designed, which enables to associate the shape with a dose, even though the surrounding doses are missing. Isosceles triangles with a base of 2 µm were chosen. Sixteen such triangles were each rotated by multiples of 22.5 ° resulting in a unique degree of rotation for every dose.

For the ATR-IR measurements, the 4 μm^2 structure was too small, therefore two approaches were executed to generate bigger structures. The first approach (defined as window mode in this thesis) was to apply the dose by imaging for a defined time. This was accomplished by using the equation above, but calculating the amount of time the beam was directed onto the whole area and starting and stopping it by hand. By choosing the right magnification, areas of 100 µm x 100 µm can be generated in this fashion.

The second approach was to use the patterning engine. However, with a large number of patterning points, the system tends to overflow. Here, an alternative was to stack 1 µm x 1 µm squares next to each other until an area of 80 μm^2 is obtained.

The electron penetration depth in the conversion gradient investigations were performed through Monte Carlo simulations using the CASINO software (Casino, version 2).[31]

3.3.6 Atomic Force Microscopy

Atomic force microscopes (AFM) are a special kind of scanning probe microscopes (SPM). Through line by line scanning over the surface of a sample, occurring distance dependent forces are tracked and used to create an image. Because the images are obtained by touching the sample, the tip is the most important part of the microscope. To be able to deduce the information about the tips behaviour, it is placed on a cantilever, whose movement tracked via a laser beam focused on the back of the cantilever. Its reflection is measured by a four segmented detector, transducing the position of the beam to electrical signal. Different styles of tracing the tip surface interactions are possible, whether the tip and cantilever system (probe) is used statically or dynamically. In static measurements, the tip "scratches" over the surface, or hovering in a certain distance from it, causing the cantilever to deflect the laser beam corresponding to lateral and torsional forces. Depending on which interaction regime is used, it's called "contact" or "non contact" mode. In the dynamic measuring method, the cantilever oscillates whilst scanning the surface, resulting in varying changes in phase and amplitude additionally to the topological information. For the precise scanning movements piezoelectric materials are used, which can be either placed on the scan head or the stage. High precision electronics are used to communicate with the operating computer and control the piezoelectric material. Signal processing and controlling the system is done via software. AFM measurements are possible in various environments, temperatures and pressures. To measure in liquid environment, it is necessary to design some AFM parts to withstand wetting, especially the electrical constituents have to be protected to avoid failure.

3.3.6.1 Basic components

In this section, the basic components of a regular AFM are described. The probe is described generally and further aspects considering liquid measurements and soft samples are mentioned. The detection and movement systems are presented briefly.

Tip and Cantilever: While the tip actually interacts with the surface atoms, the cantilever enables to track this interaction. Material properties like stiffness and spring constant are chosen in regard to the investigated material, to minimize damage or alterations during measurement. Especially for soft matter (in liquid) a small spring constant is recommended, however the limitation for decreasing it is the elastic energy, which is increased by thermal energy of a cantilever in equilibrium with a thermal bath. The smaller the spring constant the higher the thermal noise amplitude. A very important property of mechanical systems, in this case cantilevers, is their resonance frequency. The possible imaging speed is determined by it. If a defined surface with corrugations of a specific dimension is measured in a defined resolution and time, a certain frequency of oscillation is necessary. To be able to detect corrugations, this oscillation has to be much higher, than a theoretically assumed frequency of the surface features. Fast scanning of soft matter is best with low stiffness and high resonance frequencies. Tips and cantilevers are typically produced with microfabrication techniques. There are a variety of different material and shape options, because the choice for the most appropriate tip and cantilever is dependent on the specific measurement.

In this thesis two different kinds of probes are used. Fast Scan A (Bruker AXS, Santa Barbara, CA/USA) for measurements in air and Fast Scan D (Bruker AXS, Santa Barbara, CA/USA) for measurements in liquid environment. Both can be seen in Figure 23.

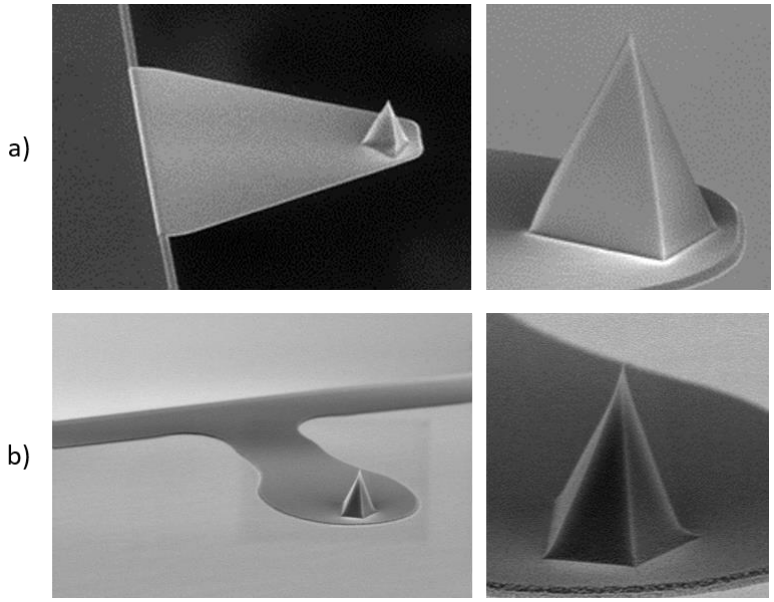

Figure 23: a) SEM Image of a Fast Scan A probe. At the end of the triangular cantilever rests a pyramioid tip. b) The cantilever has a spoon like shape with a pentagonal pyramid as a tip at the end.[32,33]

The cantilever of the FastScan A is made from silicon nitride, has a triangular cantilever and features a mean resonance frequency of 1400 kHz and a nominal spring constant of 18 N/m. The silicon tip of an unused probe has a radius of 5-12 nm.[32] The fast scan D probe is used only in liquid measurements. Its special geometry leads to resonance frequencies around 110 kHz and a spring constant of 0.25 N/m.[33] The sharpness of the tip is a direct limiting factor for image resolution. Generally, the sharper the tip, the better the resolution of the resolution image.

Because the image quality is dependent on the tip radius to such extend, the susceptibility for measuring errors due to tip changes is evident. Convolution and contaminations can lead to imaging artefacts. Furthermore, used tips tend to broaden in radius, decreasing the ability to detected small structures. A detailed description of these artefacts and possible solutions can be found in 3.6.4.

Measurements in different environments cause different occurring forces between the tip and the sample. While measuring in air, capillary forces are the main contributor in the tip-sample interaction, in liquid, electrostatic interaction play a much bigger role. The electronic double layer effect, see fundamentals, has a significant impact on the possible resolution. The presents of ions in the buffer solution means that to improve resolution, contact between tip and sample is inevitable. As already mentioned, for soft materials this kind of introduced lateral stress can be damaging. To enable high resolution imaging without damage, special soft cantilevers with high resonance frequencies, which allow for dynamic measuring, can be used. Summarizing, one can note, that the resulting image quality is dependent on the used buffer, as well as the concentration of charge carriers, and the mechanical properties of the cantilever used.

The cantilever oscillation in liquid also differs from that in air. The density of most liquids is higher than airs, therefore the effective mass of the oscillation system is always higher in solution than in air. This leads to a reduction in resonance frequency. The damping effect of the liquid also causes a lowering of the quality factor Q. These two effects have consequences regarding the cantilever oscillation.

Compared to harmonic and sinusoidal oscillation in air, in liquid it is asymmetric. Figure 24 shows the different resonance behaviours of the used AFM probes.

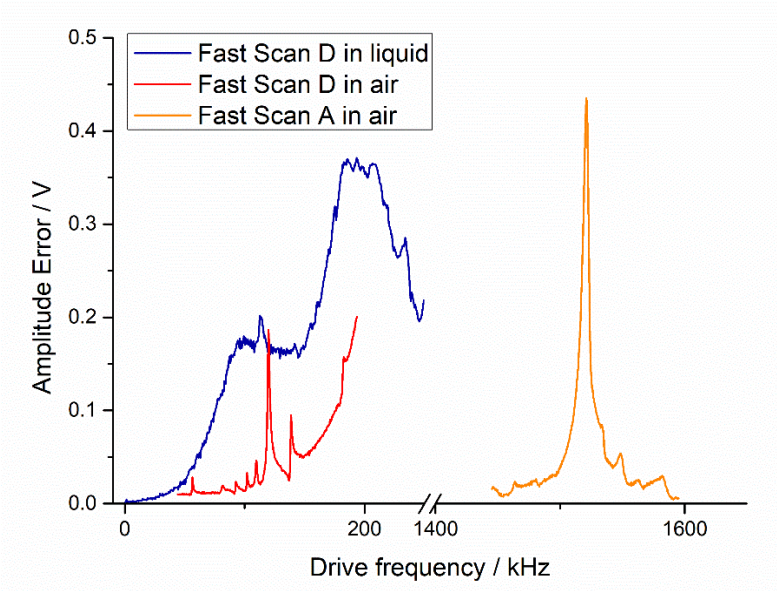

Figure 24: Resonance behaviour of different AFM probes.

It can be seen, that the resonance frequencies are different for the two cantilever designs and properties. The additional liquid contribution to the amplitude signal is evident as well, making the process of finding the "right" frequency more demanding than in air.

The liquids high viscosity can increase the imaging speed of the AFM, because the additional damping can have a positive effect on the decaying behaviour of the used (high) frequency. Figure 25 demonstrates this. The possibility of measuring with high speed in physiological conditions enables the in situ observation of biological processes.

Detection components: To track the cantilever movement, and therefore the interaction between tip and sample, a common method is to measure the deflection of a laser beam, focused on the back of the cantilever. A photodiode detector, which is split into four segments, converts the intensity of the incoming laser light to an electrical voltage. Voltage differences along the vertical axis of the detector correspond to vertical movement of the cantilever. Voltage changes in the horizontal axis indicate torsion and friction forces. This way of transducing the interaction has its strength not only in the simplicity of the set up but also in the measuring sensitivity. The smallest measurable deflection has been reported to be 1 Å [35], leading to atomic resolution in the best cases. A differential amplifier sends a magnified version of the incoming signal to the controller regulating the movement of the probe, to compensate the lateral or vertical alteration. When measuring in liquid, it is vital that the whole laser beam path is in the solution, because any liquid-air interface introduces refractive effects. The detected intensity of the beam is much smaller compared to in air, because of scattering effects. The minimal necessary amount of signal for proper measurement is 1.5 V for the used AFM to have a reasonable signal to noise ratio.

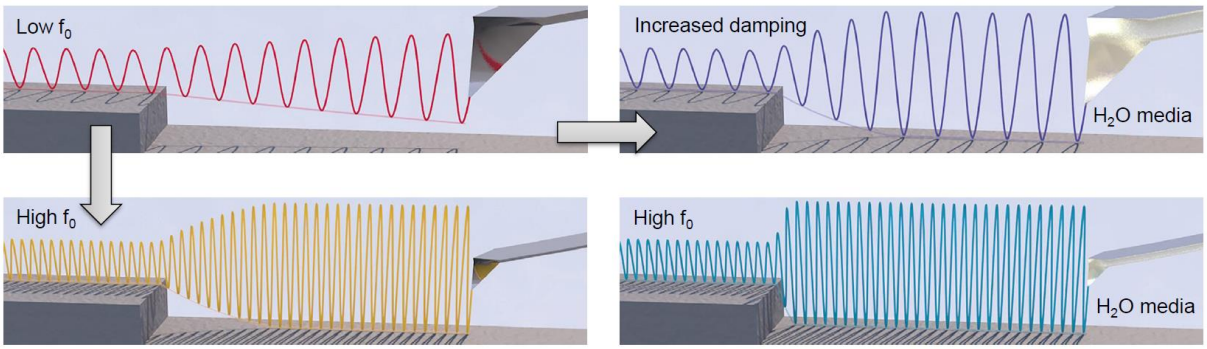

Figure 25: Oscillation behaviour of a cantilever in air (left top and bottom) and in liquid (right top and bottom).[34]

Piezoelectric components: Materials, which have piezoelectric properties, experience a change in potential as a response to applied stress. This effect is reversible, meaning that a change in potential results in a dimensional change of the material. This can be used to position the tip and the sample very precisely, thus scanning with an AFM is performed with piezoelectric ceramics. They can be either positioned to move the sample in respect to a fixed tip, or to move the tip in regard to a fixed sample. A common piezoelectric scanner set up is tube shaped. The tube is divided in four equal segments, with two opposing ones respectively. Electrodes are placed on each segments inner and outer wall. Opposing segments are responsible for movements in one dimension, e.g. +x, -x direction. To induce extraction or contraction, a voltage is applied to one of the inner electrodes and all the outer electrodes. This causes the tube to bend and therefore move the tip. An image is generated by a sequence of voltages applied to a fast direction and a slow direction. This tube bending can lead to a measurement artefact, see 3.6.4. Furthermore, these scanners are non linear and hysteresis effects can occur. Capacitive sensors can be built in to enable measurement of the position additionally to the voltage. With this, a closed-loop system can be implemented to counteract any nonlinear or hysteresis behaviour.

For measurements in liquid environment two aspects have to be considered. The piezo tubes are actuated by high voltages, so the contact with any liquid has to be prevented. To ensure long-term stability of the system, rubber is needed for further insulation to avoid wetting. To improve measurement speed and ensure the stability of the scanner tube it is more common to move the tip instead of the sample, because of the smaller added effective mass.

Feedback loop: The idea of a feedback loop in AFM is to keep one parameter constant, whilst a signal of this parameters change is measured during the scan of a surface. This parameter can either be height, amplitude or phase. The system strives to uphold e.g. a constant amplitude in dynamic mode by constantly comparing the actually measured amplitude to a predefined set point and adjusting other parameters such as height to maintain the amplitude value. Two parameters associated with optimizing the feedback loop system are integral gain and proportional gain. Correctly chosen, the feedback system reacts in the most optimized ways to the surface. Inaccurately set gains can result in artefacts and lost information.

3.3.6.2 Relevant Setting Parameter

The AFM image is generated by scanning line by line and for each line tracking the backward and forward movement of the tip. Therefore, one important set of parameters are the scan dimensions. The **Scan Size** defines the distance that the tip moves per line. It is limited by the range of the piezoelectric tube scanner, 30 µm is the possible range for the used FastScan Bio AFM (Bruker AXS, Santa Barbara, CA/USA). The **Scan angle** is the angle between the actual scan lines and the x-axis of the scanner. The **Aspect ratio** is defined as ratio between length of the fast axis and length of the slow axis.

Another important set of parameters are the scan rate and the tip velocity defining the imaging speed. The **Scan Rate** specifies how many back and forth scans ("trace" and "retrace") happen per second. The **Tip Velocity** is defined as the ratio between scan rate and scan size, resulting in the actual velocity with which the tip moves. The resolution of the generated digital image can also be influenced with parameters. How many **Lines** the scanner travels along the slow axis has to be defined. Also, how many data points are acquired per line is relevant to resolution considerations.

Parameter considering the feedback loop influence the quality of the image. For sufficiently fast responses of the loop, the error signal has to be minimized. The **Proportional Gain** is a value proportional to the magnitude of the error signal and can be specified by the user. The **Integral Gain** is proportional to the magnitude and duration of the error signal. A possible way to optimize both parameters is to look at the amplitude image whilst adjusting. Increasing the integral gain until the image starts to get noisy and then slowly decreasing yields a reliable way to find suitable values. A rule of thumb used with this specific device is that the proportional gain is a factor 5 bigger than the integral gain. With the **Amplitude Set Point** the voltage for the feedback loop and therefore the damping of the actual amplitude. It can control the force applied to the sample to a certain extend. The **Drive Frequency** is the frequency at which the cantilever is excited. The **Drive Amplitude** is the amplitude of the oscillating cantilever. Low drive amplitudes correspond to "soft" measuring, whilst higher chosen values, result in a firmer scanning manner.

3.3.6.3 Operating Modes

As mentioned at the beginning of this chapter, different operating modes are possible in AFM. Static modes use a tip, which slides over the surface being in direct contact with it. The cantilever bends as a result of the tip scanning over the surface and the feedback loop holds the deflection (position of the layer) constant. A major drawback of this technique is the amount of force which is applied upon the surface and the alteration of especially soft samples. Destruction, delamination or partial material removal can occur during scanning. This is accompanied by the faster wear down of tips, because they are exposed to the same forces. To overcome these difficulties, the dynamic mode presents a way of scanning with minimal damage.

In the dynamic mode, the probe is excited to oscillate at its resonance frequency whilst undamped and away from the sample. The appearance of the resonance peak is influenced by the cantilever stiffness and the components which are coupled to the vibrating system. The sharpness of the peak gives information about the quality factor, which in turn relates to the damping caused by the surrounding medium (air/liquid). If the oscillating system is approaching the surface of a sample, they couple to a new system, where the resonance frequency and thus the amplitude changes. The amplitude is continuously dampened during the approach until a certain pre-set value is reached. This amplitude set

point can be interpreted as the force that reduces the cantilever amplitude while tapping onto the surface. High set points equal small forces and vice versa. Topological features and material differences change the coupled oscillating system and result in an amplitude change. The feedback loop strives to balance these changes and corrects the amplitude back to the amplitude set point by changing the interaction distance (z-piezo element). Another relevant parameter is the phase difference between excitation of the cantilever and the signal that is detected. A material difference along the surface, causes a detectible phase lag because of a difference in stiffness, adhesion and ultimately electron densities. The possibility of simultaneously tracking height and qualitative material information represents a powerful tool in surface analysis.

3.3.6.4 Artefacts

Three main sources for measuring artefacts can be found in AFM. The geometry of the tip, the feedback loop and the piezo tube movement. The tip geometry heavily influences the quality of a scan. The dimensions of the AFM tip apex can lead to a phenomenon called convolution. This effect especially is relevant if the measured object is smaller than the tip. Objects are portrayed larger than they are. Additionally, contamination or damage can result in more than one apex. If both apexes are in contact with the surface, a copy of the measured structure can be imaged, where the distance of the copy and the original object is according to the distance of the apexes. This is known as a double tip effect. Figure 26 shows both phenomena schematically, while Figure 27 shows a double tip artefact.

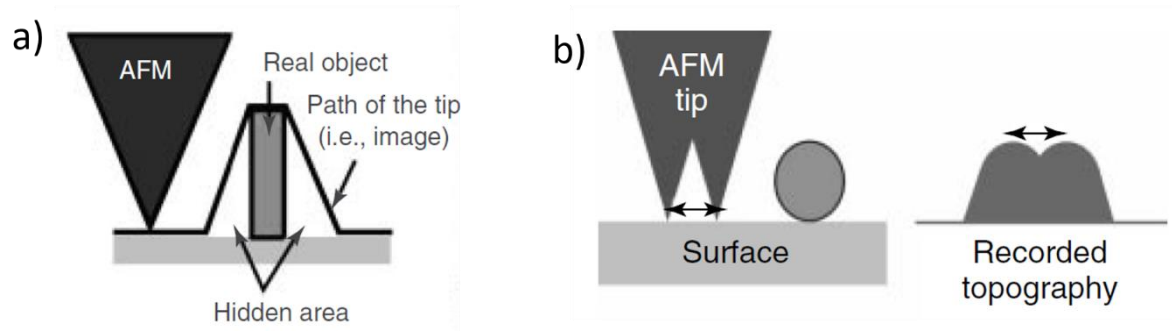

Figure 26: Tip geometry related artefacts in AFM imaging. a) Convolution. b) doubletip.[36]

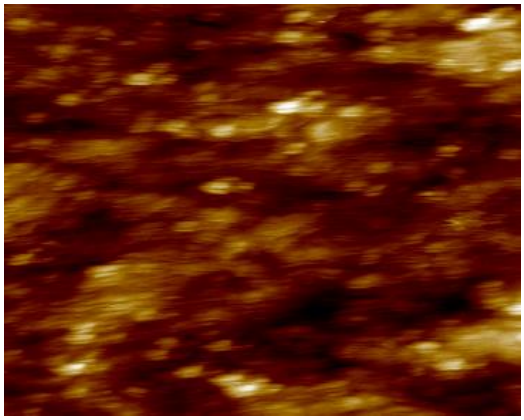

Figure 27: Demontration of the double tip artefact in an AFM image.

As mentioned above, the generation of an AFM image is tightly bound to the feedback loop. The choice of proportional and integral gain is dependent on many factors such as the used probe, the condition of the tip, vibrations caused by the surrounding building and the piezoelectric scanners. Incorrect adjustment of either parameter can either result in too slow responses of the system visualized by elongated objects and unequal images for forth and back scanning or an unstable system introducing high frequency oscillations, which can be mistaken for surface structures, see Figure 28.

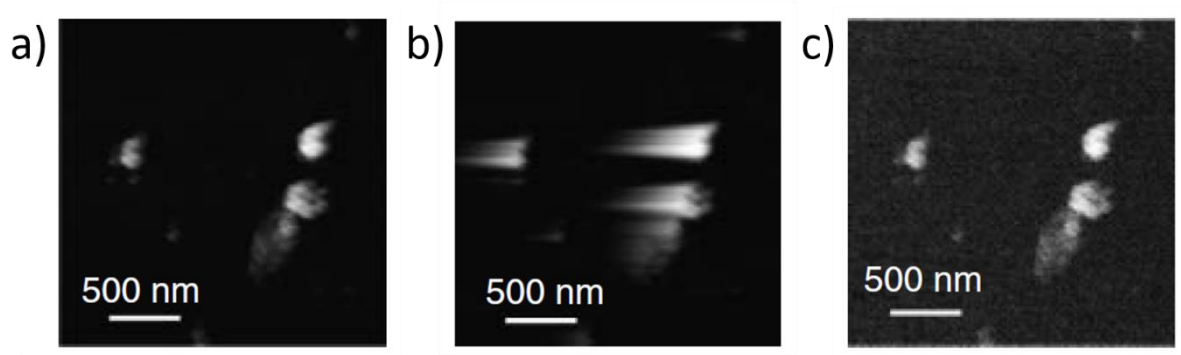

Figure 28: Artefacts related to the feedback loop and the corresponding parameters. a) Correctly set parameters. b) Too low feedback parameters, resulting in elongated features. c) Too high set parameters, resulting in a high frequency oscillation.[36]

Another effect is piezo tube bending. Instead of a plane, an arc can be measured because of the bending movement of the piezoelectric tube. This effect is compensated by a proper system calibration but has its limit. The effect magnifies in cases where large areas with comparably low heights are measured. To correct this occurrence, a polynomial function has to be subtracted from the data.

3.3.6.5 AFM Device and handling.

The measurements were carried out with a FastScan Bio AFM (Bruker AXS, Santa Barbara, CA/USA) which is handled by a Nanoscope V controller. For the investigations in air environment FastScan A (Bruker AXS, Santa Barbara, CA/USA) probes were used with a reported nominal spring constant of 18 N/m and a tip radius of 5 nm – 12 nm. For the liquid measurements FastScan D (Bruker AXS, Santa Barbara, CA/USA) probes were used with a nominal spring constant of 0.25 N/m and a tip radius of 5 nm - 12 nm as well. Both techniques were utilized under ambient temperature and pressure. The procedure for air measurement was as follows: The cantilever was tuned and set up regarding the laser and detection system. The sample was placed under the tip on the stage. Careful approaching was carried out utilizing a light microscope focused 1 mm about the sample surface. The scanning parameter were set and the approach was initialized. The approach was carried out by a system routine that engages the last 1 mm of distance to the sample automatically. When the tip was successfully approached the software starts scanning with the tip being in intermediate contact. At this point a surface tune was performed to account for the new oscillating system. The above-mentioned parameters were varied until the imaging quality was satisfying.

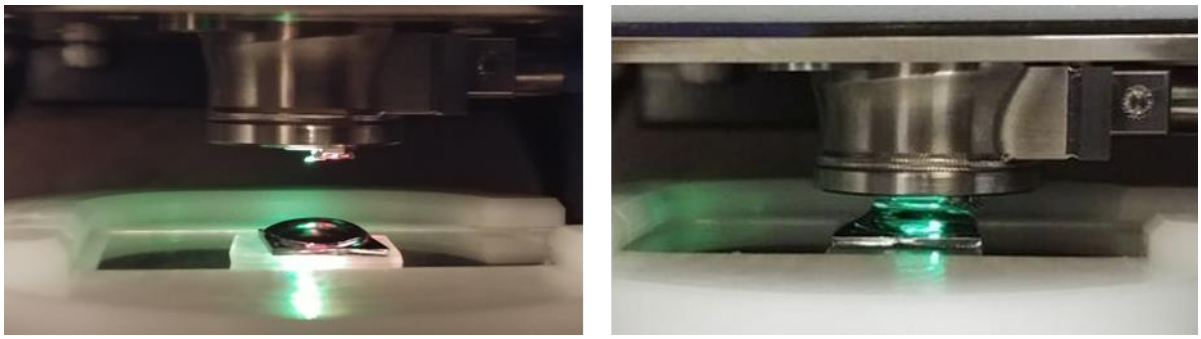

Figure 29: Immersion of the cantilever system into a solution drop.

To perform a measurement in liquid a droplet of the solvent was placed on the surface. It was important that the height of the droplet was sufficient to ensure full immersion of the cantilever laser system. The sample was placed under the tip. The scan head goes down until the system was wetted and the surface tension of the buffer causes a cylindrical liquid drop, fixed on both ends. The fully immersed cantilever has to be aligned again in liquid because of the changed refractive index. Figure 29 shows the dipping into the solution droplet. Depending on the wettability and surface energy of the drop-surface system, too low contact angles can result in too shallow drops to immerse the cantilever. As a work around, the substrate can be bordered with paraffin wax, preventing the droplet from dripping away. Figure 30 shows a gold slide, coated with cellulose, surrounded by paraffin wax to contain the liquid.

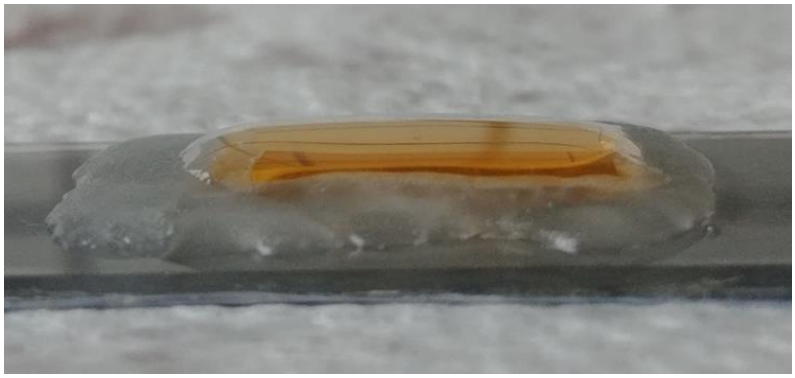

Figure 30: Substrate surrounded with paraffin wax to contain the liquid drop.

4 Results

In this section of the thesis, the evaluated results are presented and discussed. The AFM images were processed with NanoScope Analysis (Bruker NANO, 1.8) and Gwyddion (GPL, 2.51), while calculations and graphs were done with Origin (Electronic Arts, 9.0G).
In brief, primary AFM investigations were carried out on pristine TMSC and globally converted cellulose layers. This was followed by primary investigations of the surfaces after incubation with CMC and BSA. To investigate each adsorption step in detail, multiple measurement techniques were used. Static contact angle measurements and ATR-IR spectroscopy investigations were performed to qualitatively track chemical changes of the surfaces. To complement the obtained results with quantitative information, SPR spectroscopy was used. Followed by liquid AFM measurements, the rout of successful immobilization of BSA was confirmed.
Next, FEBIC was used for local TMSC-cellulose conversion. The treated areas were incubated with cellulase to investigate the amount of actually generated cellulose. The structures were examined via AFM, Raman and IR spectroscopy.

4.1 Primary Investigation via Liquid AFM Measurements

To investigate certain intricacies of measuring in liquid, a thin film of TMSC (1% in chloroform) was examined. A difference between an already used AFM probe and a new one, shows the massive effect of the tip quality regarding the results. Figure 31 shows the same thin film measured with a used (left) and a new probe (right).

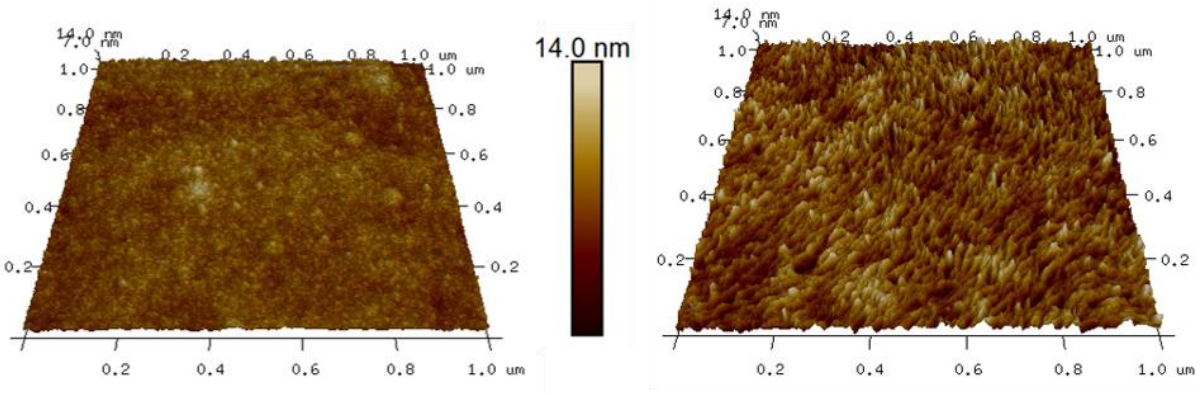

Figure 31: Surface of a TMSC thin film on a Si substrate obtained by liquid AFM measurements. Left: An old Fast Scan D was used. Right: A new probe was used to measure the same thin film. As can be seen, the tip quality influences the quality of the results.

It can clearly be seen, that certain surface structures are lost when using a worn probe. Although not unusual, the extend of the impact was slightly unexpected, which can be traced back on the small nature of individual features. The right image in Figure 31 shows the typical TMSC fibrils, which appear to have a preferential orientation. Thin films obtained by the used methods are reported to be amorphous.[17] They are on average between 5 nm and 15 nm wide and roughly about 80 nm long. With the average molar mass being given as 185000 $gmol^{-1}$ and the molecular mass of TMSC being 235 $gmol^{-1}$ (calculated

from the chemical formula), a degree of polymerisation of 787 can be estimated. Assumed the lengths of one cellubiose dimer is roughly 1 nm[37], one TMSC fibril should be about 790 nm long. Even though it is only approximated, the expected length is an order of magnitude bigger than the experimental results. However, the determination of the length was challenging, due to the absence of a clearly visible start and end of the fibrils. The overall RMS roughness of this section is 2 nm. In the left image, only the ends of the fibrils, which stick out the most, can be seen by the small, hemispherical features. The roughness of this section is approximately 1 nm, which was a result of a dull tip, not being sharp enough to measure between the fine structures.

The liquid measurement was done in a NaCl solution (0.5%) and eventually in buffer solution (NaOAc with pH 5). Therefore, it was explored how the structure of the TMSC fibrils change after having been already exposed to the salt solution, dried and rewetted. Figure 32 shows the same thin film, once freshly immersed in the solution (left column) and once remeasured after drying (right column).

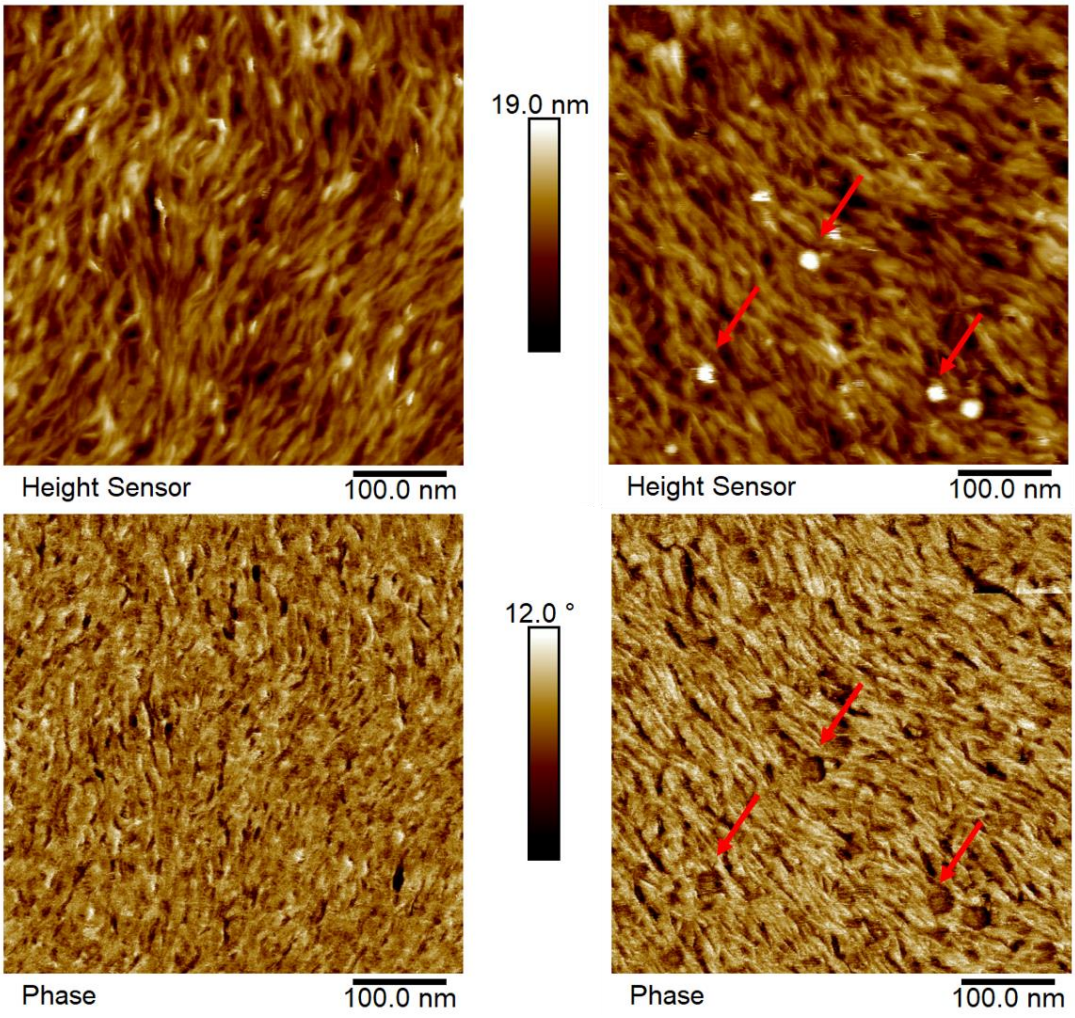

Figure 32: Liquid AFM measurement of TMSC thin film (1%) in NaCl solution (0.5%). Left column: height (top) and phase image (bottom) of a newly immersed TMSC film. Right column: height and phase image of the remeasured film.

In the newly measured TMSC, the fibrils can again be clearly seen. The phase image shows possible material differences or edges of the surface. The dark areas in the phase image correspond to deep

areas in the height image, indicating an edge effect. In the cases where the low phase signal occurs on sites where the height images shows a high feature, it could indicate some chemical residues, which surround the fibril. The white highlights also occur over the whole image, but in the most cases it looks similar to the rest, being on the right edge of a fibril. Also, a measuring artefact could cause such a result. However, some single spots seem individual in shape. It is possible, that the salt in the solution contaminates either the tip or the surface to a degree. Looking at the height and phase image of the remeasured film, overall the fibrils look similar, but two differences can be seen. Some round height features are present (red arrows), which are not visible in the newly measured film. This could stem from salt sedimentation during the drying period. NaCl should dissolve in contact with water quickly, but with significantly high salt concentration, dissolution can take longer than the AFM measurements lasts. Another indicator, that this is no TMSC structure, is the phase image, which clearly shows a difference in material. The phase signals align with the height image. The second difference is that it appears the phase image of the remeasured film has a higher resolution regarding the streaks on the fibrils themselves, which are absent in the first image. Comparing these images with reported structures of amorphous and crystalline cellulose, suggests a certain amount of crystalline structure.[38]

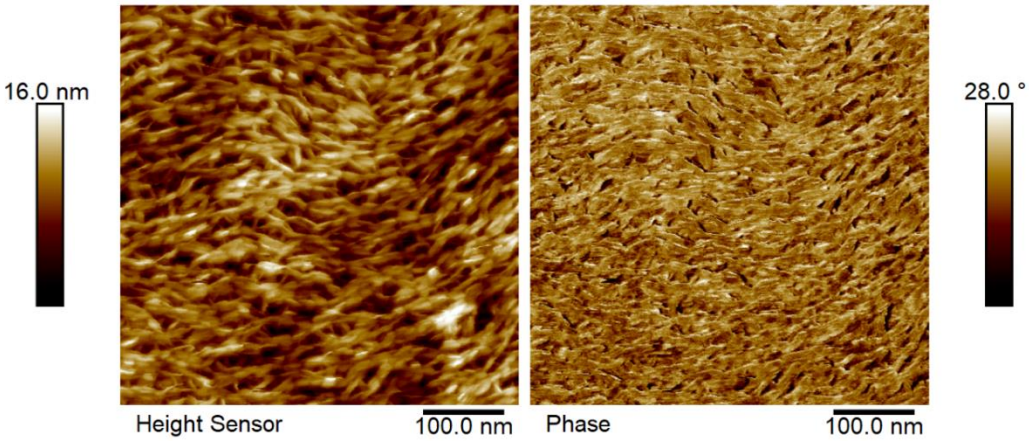

Figure 33 Liquid AFM measurement of converted cellulose in NaCl solution. Left: Height image. Right: Phase image.

Next, the TMSC films were regenerated to cellulose by global exposure to HCl vapours (created from a 12 % solution). AFM measurements of such converted cellulose films were done in same conditions as before and are shown in Figure 33 by height (left) and phase images (right). In contrast to TMSC (Figure 32), where ruffled looking fibrils lie anisotropically next to each other, the cellulose appears to consist more of bundles linked to one another. They are averagely 30 nm long and 8 nm wide. The decreased diameter, comparing to TMSC, could be attributed to the mass loss observed after conversion. However, the ratio between crystalline and amorphous fibrils is unclear, and swelling effects could broaden the measured width. The reported widths for cellulose nanocrystals correlate sufficiently with the measured data. However, the lengths are reported to be at least 70 nm ranging up to 2000 nm, being significantly longer than the observed structures.[39] Additionally, approximating the observed structures as cylinders and calculating the volume of one molecule leads to roughly 100 macromolecules per fibril. A certain amount of crystalline cellulose regions suggests itself, being in accordance with the contact angle measurements of cellulose. Because amorphous cellulose should swell much more than TMSC in water, the former was continuously measured for 70 minutes, selectively shown by height images in Figure 34.

Although a drift of the whole area of about 100 nm occurred, the directions and the dimensions of the bundles stay the same for the duration of the experiment. Declaration of swelling behaviour is challenging because the swelling could be smaller than the unavoidable tip convolution. Strong structural changes are reported to take place for similarly prepared cellulose thin films after exposure to water.[17] However, the AFM images in this citation were obtained under ambient conditions, leading to a limited comparability with the liquid images. A close look on the images suggests stabilization after about 10 minutes, which is important for subsequent experiments to establish stable conditions.

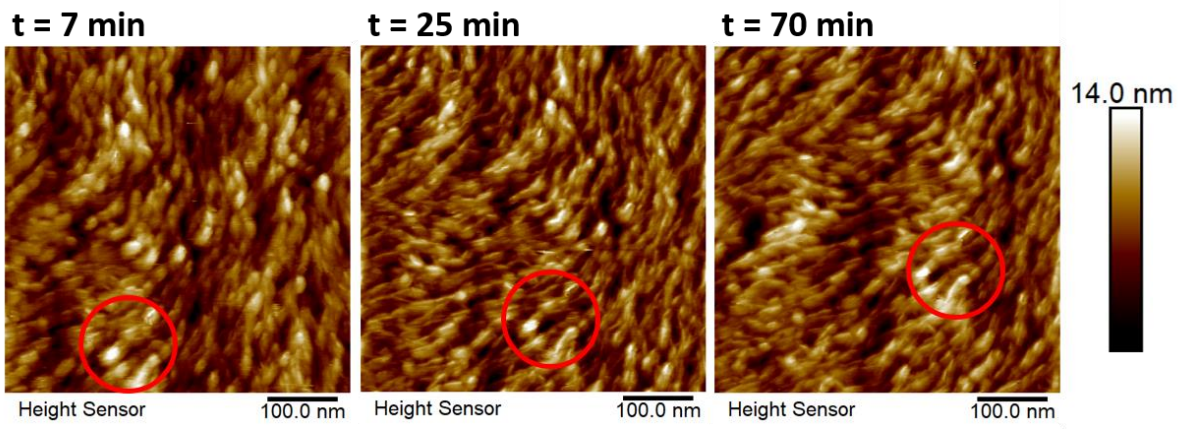

Figure 34: Liquid AFM measurement of converted cellulose in NaCl solution after 7 min. (left), 25 min. (centre) and 70 min. (right). The circle indicates the same feature for orientation.

Next, a 0.2 % CMC solution was dropped on the cellulose surface and incubated for a period of 10 minutes. The surface was then rinsed and carefully CO_2 blow dried. After that, BSA (0.1% in NaOAc buffer) was deposited onto the surface identical as the CMC solution. The corresponding AFM images can be seen in Figure 35.The structure of the CMC layer on cellulose appears similar to that of pure cellulose film (compare to Figure 34). However, this could stem from the similar molecular structure of both biopolymers, steric considerations regarding the carboxyl group on the CMC would nonetheless call for a more visible change in surface structure. Furthermore, the polyelectrolytic properties of CMC are reported to positively influence the formation of monolayers.[19]

Comparison of literature AFM images of a CMC surface suggests a certain similarity to the obtained data. The CMC used in this experiment has not undergone the dialysis, freeze-drying and dissolution in buffer. It is possible, that CMC, which was dissolved in a NaCl solution, indeed has adsorbed on the surface at one point, but was flushed away by either the rinsing or in the solution of the liquid measurement. However, the corresponding phase image does look different. The patchy areas indicate a different material, which possibly could be attributed to carboxyl methyl groups as expected. The central / right column in Figure 35 show the surface after incubation with BSA at different scan ranges (see scale bars). The change of morphology is clearly evident, strongly indicating adsorbed BSA. In more detail, the fine fibrillary features were reduced, which suggests preferred adsorption in the narrow inter-fibrillary trenches. This is supported by the widely homogenous phase images apart from morphology induced phase variations at edges. The right column shows a larger region, which confirms a homogeneous adsorption. Please note the larger particles, which often appear after incubation /

cleaning procedures. As the AFM is analytically blind, it would be too much speculation for an interpretation.

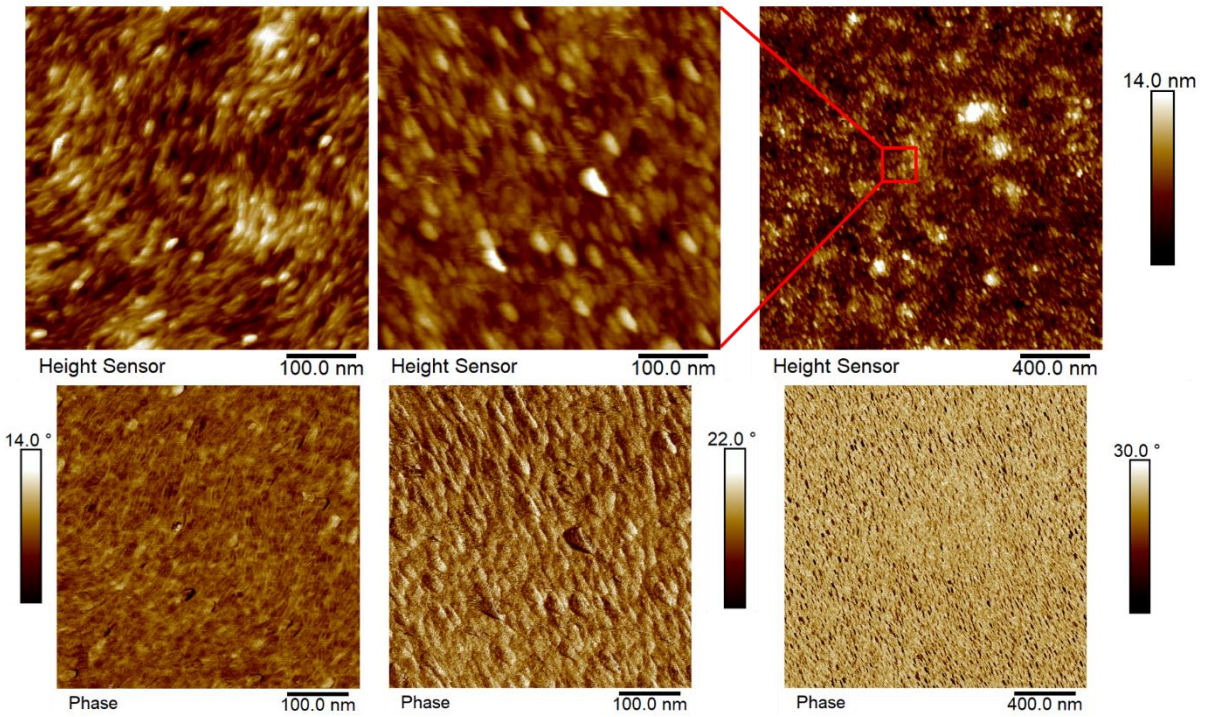

Figure 35: Liquid AFM height (upper row) and phase measurement (bottom row) in NaCl solution after CMC (left column) and BSA exposure (centre and right). The right column gives an overview image while other columns show small scans.

In conclusion, we have studied the surfaces of thin TMSC layers at different stages during cellulose conversion, CMC and BSA incubation. The result strongly suggests both, adsorption of CMC and BSE, which forms the basis for all further experiments. To verify these indications, further experiments are presented in the following chapters.

4.2 Static Contact Angle Measurements

Thin films of TMSC (2.23 % in xylene) were prepared and coated as described in 3.2.2. Contact angle measurements were carried out with three drops per slide and for 3 slides per layer to provide a certain amount of statistics. Figure 36 shows selected examples of water drops deposited on the different surfaces. It can be seen, that the high contact angle on TMSC (a) of (90 ± 3) °, gradually decreases for cellulose (b) to (46 ± 3) °. CMC (c) shows a contact angle of (23 ± 4) °. In addition, the EDC / NHS layer (d) and BSA (e) lead to small angles of (19 ± 2) ° and (20 ± 4) °. Interestingly, the anti-BSA layer (f) leads to higher angles of (50 ± 19) °. Variations are mostly due to the surface roughness which influences the wettability.

The high contact angle of TMSC can be explained by its apolar and hydrophobic functional groups, which minimize the amount of water they can interact with and is well reported to be (95.8. ± 2.8) °. [40] The contact angle for pure cellulose is reported to be half of the measured value, namely (25.0 ± 0.5) °[40], reasoned with the hydroxyl groups, which are polar and welcome interaction with water. The obtained

angle could indicate crystalline cellulose regions, which would be consistent with AFM measurements. CMC has additionally to hydroxyl groups sites with carboxyl groups, which are also polar and preferentially engage in hydrogen bonding, explaining why the even lower contact angle is reasonable. The EDC / NHS layer, which should consist of a monolayer of NHS also evoke a small angle, which is expected, because of the good solubility of this succinimide in water. The contact angles for BSA and anti-BSA, however, have to be taken with caution, because this technique is highly affected by surface roughness and it is not clear how the proteins arrange at the interface. This is further substantiated by the observation of very different angles between individual substrates. However, within one substrate consistently the same angles were found. Figure 37 sums up the contact angles, for every layer and both solvents (water and diiodomethane). The calculated surface energies are shown as well.

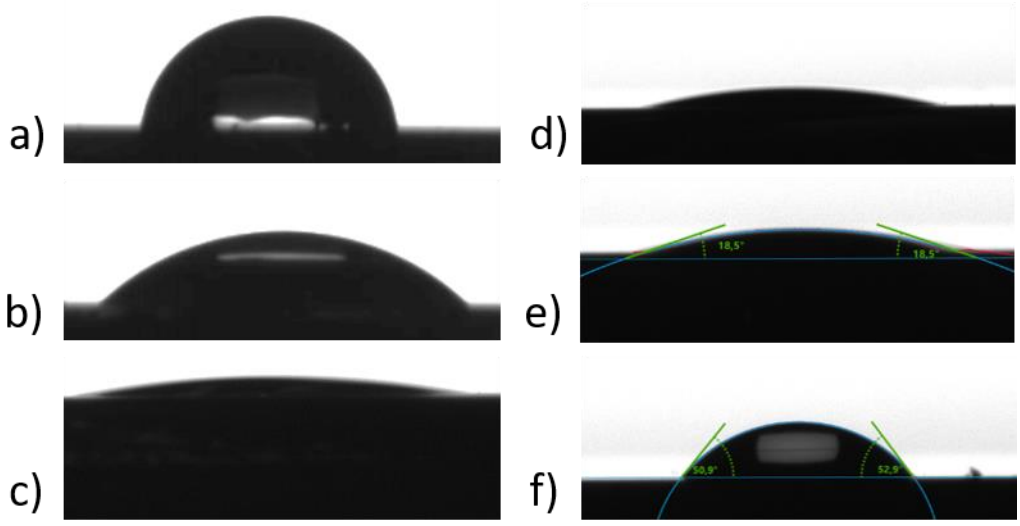

Figure 36: Contact angles of water droplets on TMSC (a) and cellulose (b) as well as after incubation with CMC (c), EDC / NHS (d) BSA (e) and anti-BSA (f) with ellipse for angle determination.

The contact angle of the diiodomethane behaves similarly, decreasing from TMSC to cellulose. For CMC, BSA and Anti-BSA the diiodomethane droplet angle was very stable even beyond the individual films. For the NHS layer, the variation between the measurements on the same slide were most present. The surface energy seems to rise with the amount of polar functional groups as expected. In general, these experimental results indicate some form of chemical change of the surface after incubation with the respective solution. The solutions were salt containing buffers, which could result in sediment particles. Moreover, the rinsing and drying steps afterwards can influence the structure as well. Both these facts introduce an uncertainty considering the roughness of the surface and therefore the resulting contact angle. Calculations suggest the lowest surface energies for TMSC thin films. CMC, NHS and BSA appear to have the highest surface energy. Further investigations could be done dynamically, leading to higher reproducibility. The important aspect of this study however, is the agreement with AFM measurements, which suggested adsorption of CMC and BSA via morphological changes. As the surface roughness changes were limited, the varying surface angle due to morphology can be excluded. Although these results were still not analytical, they support AFM results. The missing chemical information was accessed via IR spectroscopy in the next section to complete the complementary surface characterization.

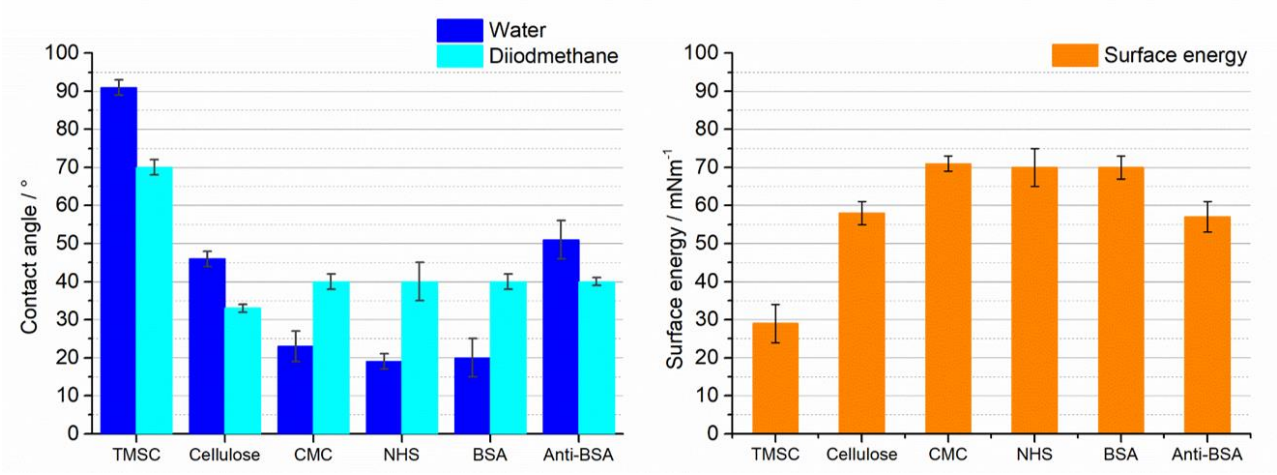

Figure 37: Contact angle of water and diiodmethane droplets on the different layers (left) and the calculated surface energies (right).

4.3 Infrared Spectroscopy

Infrared spectroscopy was carried out for the different layers, namely TMSC, Cellulose, CMC, EDC / NHS, BSA and anti-BSA. Due to instrumental requirements, all samples were prepared on thin Au layers, coated with TMSC (2.23 % in xylene) and subsequently processed as described before. Infrared spectra were gathered between the incubation steps to track the changes. Figure 38 shows obtained spectra for TMSC and globally converted cellulose.

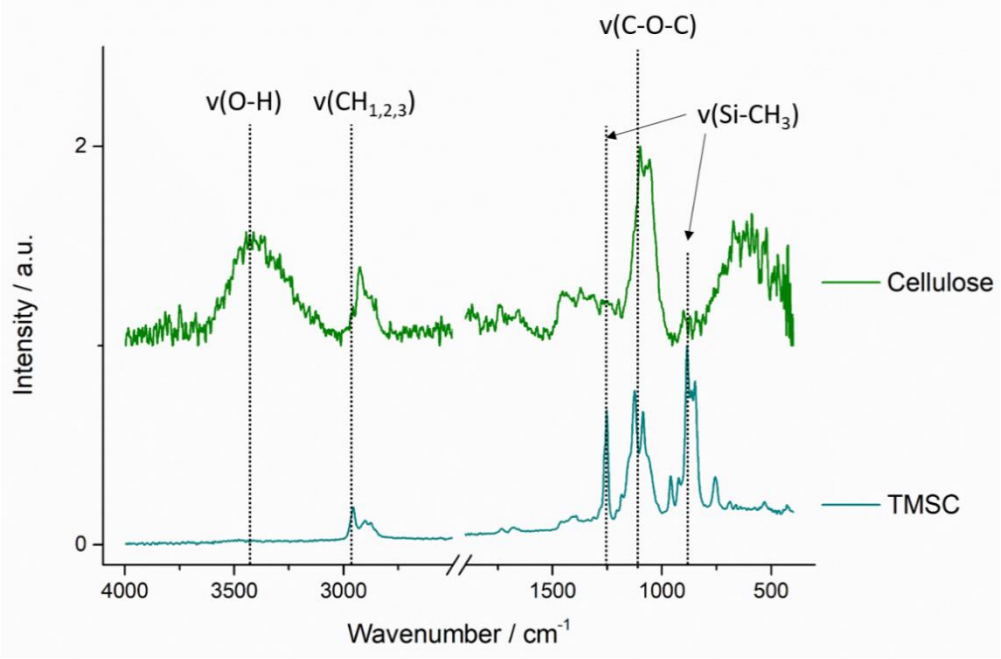

Figure 38: ATR-Infrared spectra of cellulose and TMSC.

Comparing the spectra, two indicators for successful conversion can be found. TMSC has (with a degree of substitution 2.8) trimethylsilyl groups resulting in characteristic Si-CH_3 bands at 1252 cm^{-1} and 885 cm^{-1}, in accordance with literature.[41] The absence of an OH band is another strong indicator for TMSC. After the conversion step the spectra changes significantly. The cellulose spectrum (green) lacks the Si associated vibration modes but show a clear OH band at 3430 cm^{-1} and shows strong similarities to characteristic signals from cellulose.[42] Both show the characteristic C-O-C band at 1122 cm^{-1} and 1056 cm^{-1}. Furthermore the shift of the band associated with C-$H_{1,2,3}$ from 2956 cm^{-1} to 2925 cm^{-1} is reported for regenerated cellulose[18], which clearly indicates the successful transfer.

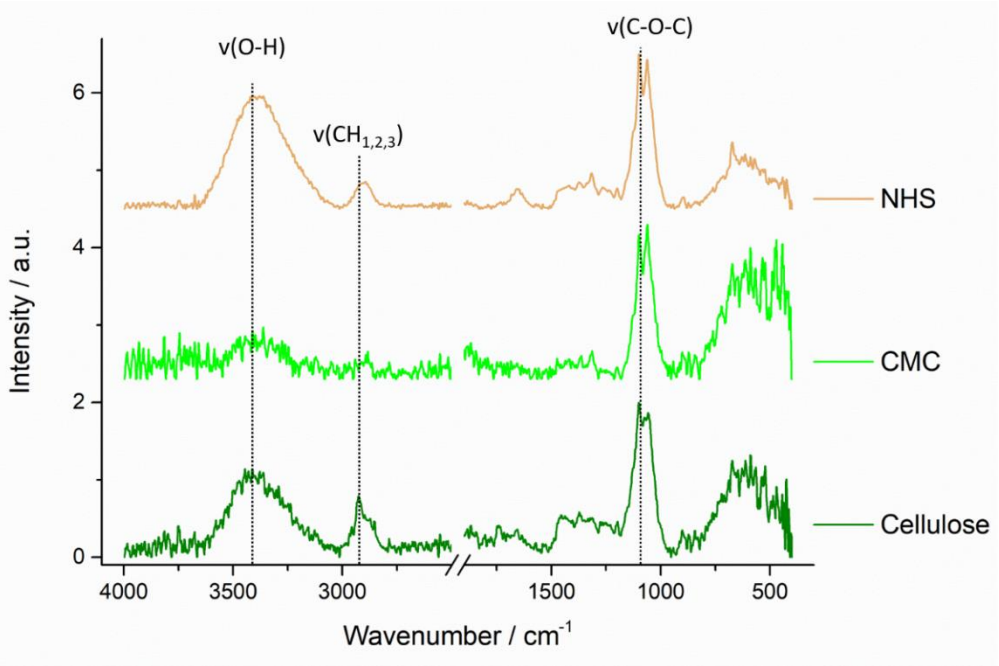

Figure 39: ATR-Infrared spectra of cellulose as well as after CMC and NHS incubation.

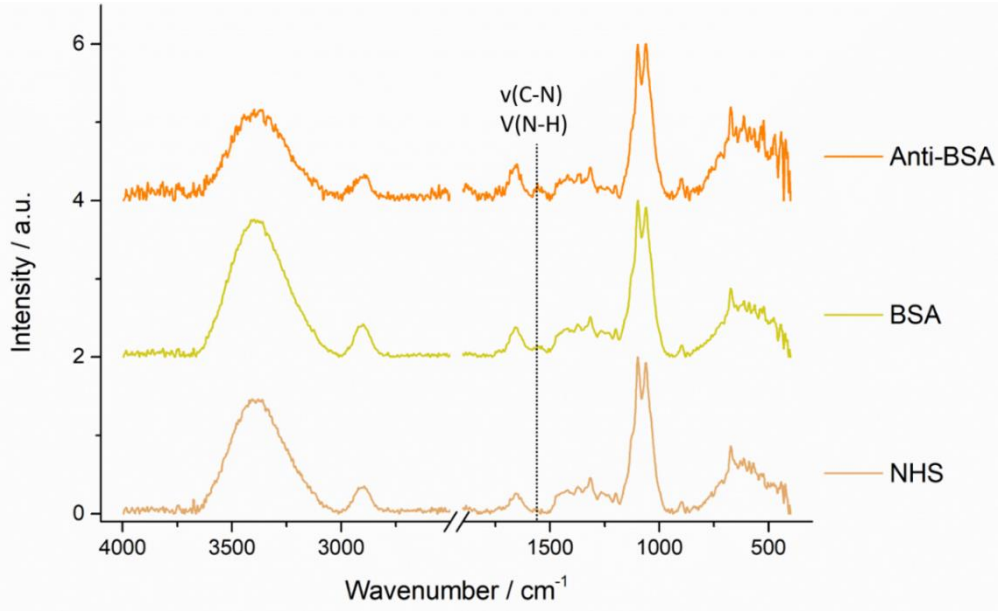

Figure 40: ATR-IR spectra of NHS, BSA and Anti-BSA.

The spectra after CMC and NHS incubation are shown in Figure 39 together with the cellulose spectra for direct comparison. Again, the characteristic cellulose bands at 3406 cm^{-1} (for OH), 2920 cm^{-1} (for C-H) and 1122 cm^{-1} / 1056 cm^{-1} (for C-O-C) can be seen, which is reasonable because cellulose is the basis layer. In the CMC spectrum the band associated with the carboxyl group (C=O) at 1603 cm^{-1} should exist[43], which, however, may be there but hidden in the noise. We attribute this missing signal to the small degree of substitution (DS: 1) and the fact that if it forms a monolayer on top of cellulose, which might be too thin for a clear signal. The spectrum after the EDC / NHS step is compared to NHS spectra because after the nucleophile substitution only the NHS should be present on the surface. Bands corresponding to N-O vibrations at 1660 cm^{-1} and to 1700 cm^{-1} corresponding to C=O oscillations are reported for NHS.[44] In the obtained spectrum a band at 1652 cm^{-1} can be seen, possibly suggesting either of the characteristic bands. However, in the cellulose spectrum a similar band was found. This again indicates a very thin, possibly monolayer of NHS. The NHS modified samples were then incubated with BSA followed by Anti-BSA. The resulting spectra can be seen in Figure 38. Because the BSA and Anti-BSA are adsorbed onto the pre-existing NHS, CMC and cellulose layers, the spectra look quite similar. For proteins, the relevant wavenumbers are reported to be between 1700 cm^{-1} and 1500 cm^{-1}.[45] The obtained spectra for BSA and Anti-BSA show a band at 1556 cm^{-1}, which was not observed for NHS, suggesting protein bonding on the surface. The standardized band appears to be more prominent for ANTI-BSA, with complements the SPR results described below, observing a higher amount of Anti-BSA adsorption than BSA. Occasionally, the measured TMSC films showed bands, which are typical for cellulose. This could stem from a too acidic environment in the laboratory. It also could mean that the methylsilyl groups tend to leave on their own, resulting in an automatic regeneration process of TMSC.

In conclusion, the IR studies further confirm the successful binding of CMC, NHS and eventually BSA as suggested by AFM (morphological) and angle measurements (functional). By that, the adsorption protocol was successfully confirmed and in the next step, layer thicknesses were in focus for the subsequently executed local conversion via focused electron beams.

4.4 Thickness Tuning

As one aim of the study was the local regeneration of TMSC into cellulose via focused electron beam induced conversion (FEBIC), the layer thickness becomes relevant together with the surface morphology after spin casting. The underlying reason is the penetration depth of electrons, which govern the conversion degree as discussed later. To control the layer thickness, spin cast parameter and the used solvents can be varied, both discussed in this section. The investigated organic solvents were chloroform, xylene and toluene. Figure 41 shows the layer thickness as dependence of the TMSC concentration in different solvents with constant spin cast parameters as used before on previously cleaned silicone substrates, see 3.2.1. To access the layer thickness, the films were carefully scratching with a razor blade and the edges measured via AFM. A representative height image is shown at the right side of Figure 41 together with a cross sectional profile underneath.

For concentrations between 0.2 wght. % and 1.0 wght. %, the obtained layer thickness is generally higher for chloroform (green) than for toluene (orange) or xylene (blue). In more detail, it linearly increases from 20 nm (0.2 %) up to 150 nm (1 %). In contrast, toluene and xylene based layers are thinner by a factor of 4 and 6, respectively, while the relative increase is still linear. The reason for that behaviour can be traced back to the polarity index of the solvents, which are 4.1 (chloroform), 2.5

(toluene) and 2.4 (xylene). This leads to preferred solvent – substrate interaction, and by that to stronger wetting behaviour and thicker layers for the most polar chloroform. Prior to a final solvent selection, we focused on the surface roughness, as this was a critical parameter for FEBIC as well. Figure 43 summarizes AFM results for TMSC layers spin cast from all solution by two different scan ranges.

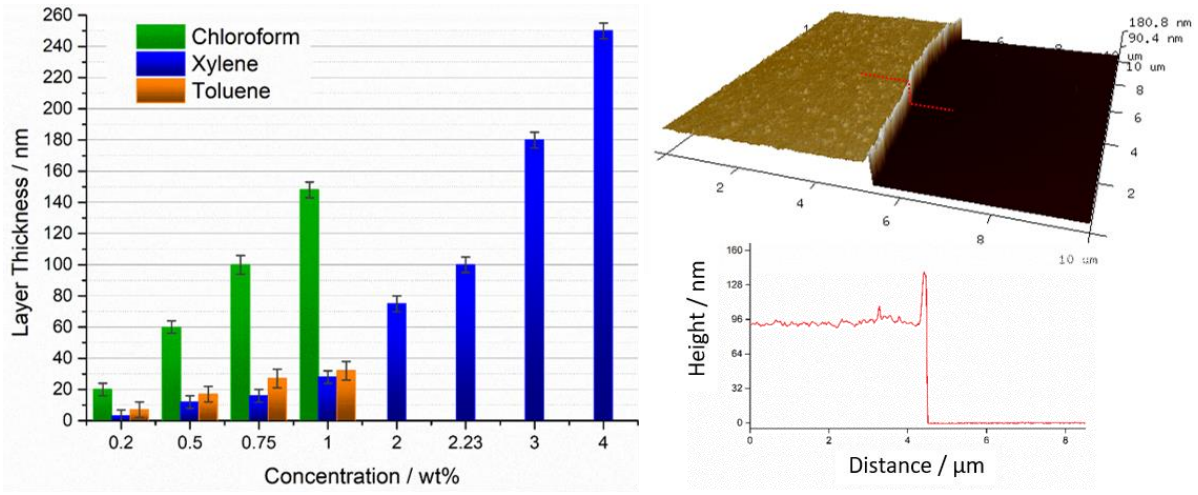

Figure 41: layer thickness of TMSC in dependency on the dissolution concetration for different solvents at constant spin cast parameter (left). The right images shows a representative AFM height image of a scratched surface (top) together with the line indicated profile underneath.

Figure 42 gives a summary of the nominal RMS surface roughness, revealing xylene as the smoothest and chloroform based films as the roughest. The latter has furthermore the largest standard deviation, which can be traced back to the formation of 10 – 20 nm deep pinholes (see bottom row in Figure 43). The background for these features is the comparable low boiling point of chloroform around ~ 61 °C compared to ~ 110 °C and ~ 140 °C for toluene and xylene, respectively. This leads to very fast evaporation where solvent bursts out of the film, leaving back the observed pinholes. Please note, the reduced RMS roughness of chloroform films on Au (see Figure 42), which is attributed to different adhesion to the substrate although the same pinholes were found.

Based on all findings, we decided to use xylene as solvent for all further experiments. To achieve the final target thickness around 100 nm, further thickness tests revealed a concentration of 2.23 wgth. % as appropriate.

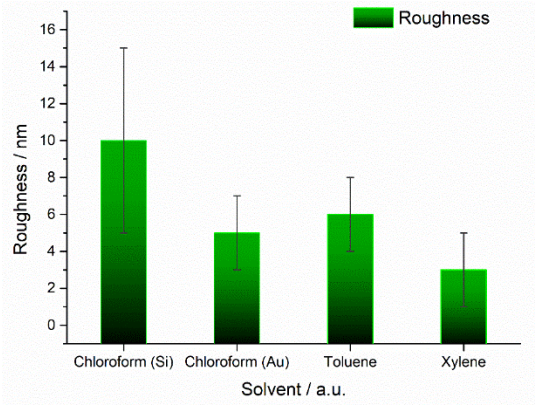

Figure 42: RMS roughness of TMSC films spin cast from different organic solvent on Si and on Au (for chloroform). The analyses were done on 10 µm² areas with a 1st order pre-tilt. Error bars were taken from the analyses software.

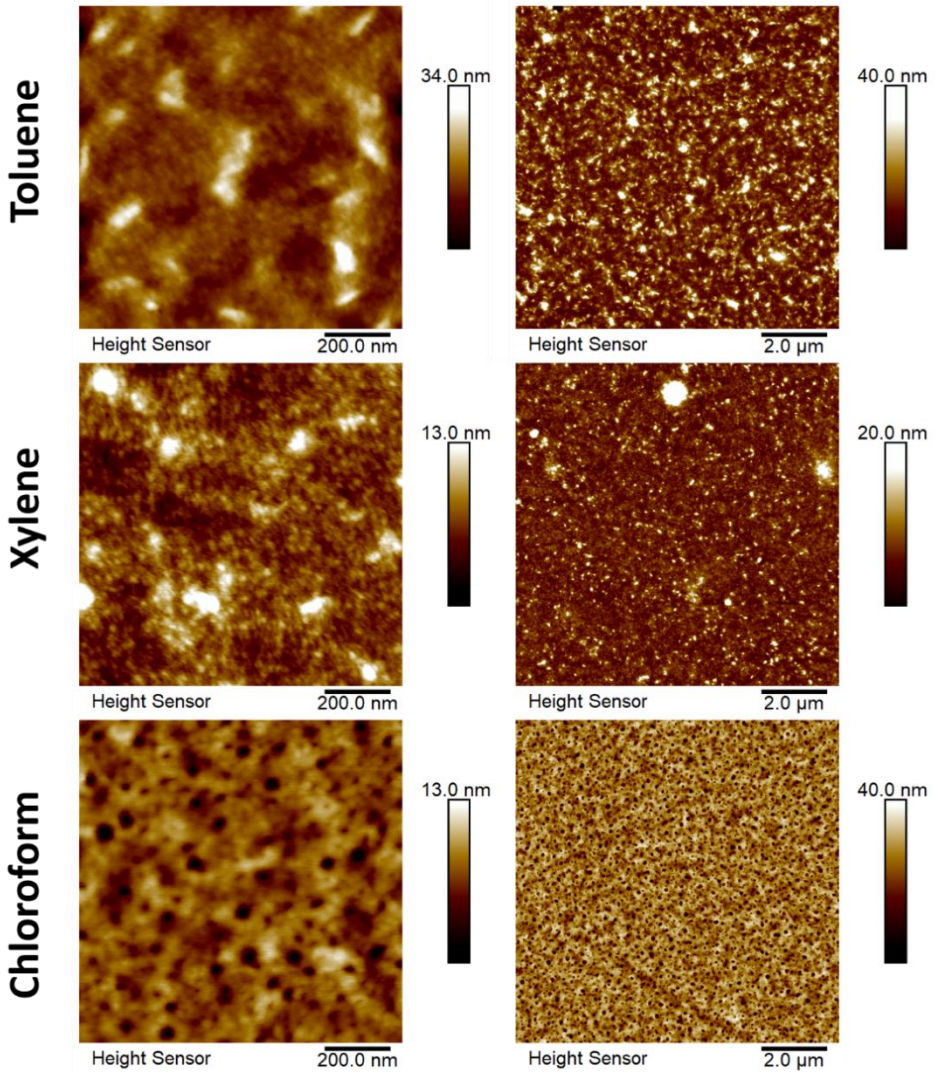

Figure 43: comparison of TMSC surface morphologies, spin cast from different solvents. Left and right columns show details and overview scanes, respetively. Please not the different scale Z ranges, which were chosen for most clear visualization.

4.5 In Situ Adsorption Measurements with SPR

SPR spectroscopy was performed to further investigate the adsorption behaviour of the different layers. Firstly, the BSA adsorption on cellulose was examined by repeatedly injecting and rinsing with a BSA solution. This was followed by experiments introducing a CMC layer before protein adsorption, where BSA and anti-BSA were injected. In the last step, additionally the EDC / NHS layer was introduced to the system. Therefore, mass concentrations between different layer systems can be compared directly.

Gold SPR slides coated with thin, regenerated cellulose (fabricated from chloroform based TMSC layers) were used with NaOAc at pH 7 as flow buffer. After equilibration (around 100 min), 1 g/l of dissolved BSA was injected for 10 min. Rinsing with buffer followed and seemingly resulted in complete dissociation. As soon as a steady state was reached, another 10 min of BSA flushing was done, to confirm the poor binding between cellulose and BSA. A third adsorption experiment was carried out with a BSA solution with similar concentration, but with longer dissolution times (~ 5 h). Figure 44 shows the obtained sensorgram for two different wavelengths relevant for our materials.

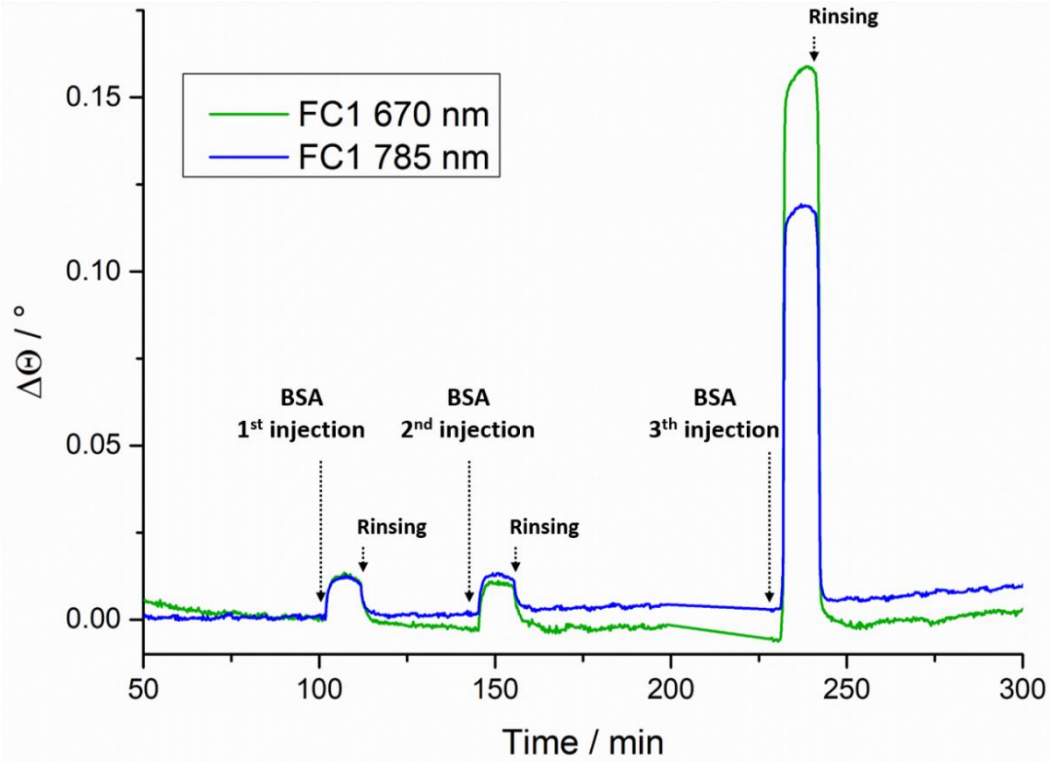

Figure 44: time resolved sensorgram of BSA adsorption (1 g/l, pH 5, adjusted by HCl) on regnerated cellulose, taken at at 670 nm and 785 nm. Both sengorgrams were recorded in the same flowcell for direct comparability.

With injecting the BSA solution, a difference in refractive index between the flow buffer and the bulk results in a quick positive angular shift of the SPR curve. This shift is maintained for the duration of injection. This either means the number of binding events equals the amount of dissociation events or that all the binding sites are already occupied, making it impossible for new arriving molecules to bind. Slow dissociation rates show small slopes upon reaching the steady state, fast dissociation rate is indicated by rapidly reached plateaus. The rinsing after reaching the steady state results for all three cases in strong dissociation, because the signal eventually returns to the baseline. The appearance of the exponential decay is only dependent on the dissociation rate constant. Residual signals after dissociation can indicate a non-specific interaction with the surface. However, this was not the case for BSA on cellulose. That the degree to which the molecule is dissolved influences the adsorption immensely is evident by comparing the first two injections (at 100 min and 145 min) with the third one. This is expected, because bulkier or crumbled up molecules are less likely to interact with a surrounding surface. This also highlights the difference between equilibrium and saturation. A system can be in equilibrium without being saturated. The limited adsorption of BSA at neutral pH values could be improved with changing the pH of the buffer solution, but even then the system reaches its limits.[46]

The angular shift before and after injection is under 0.001 °. Limited by the sensitivity of the used device, the exact mass concentration cannot be calculated, however it is evident that the amount is little to nothing. With the 3rd injection (230 min), the signal shifts 0.007 °. This shift is only slightly above the defined allowed equilibrium shift (0.005 ° per 10 min), therefore again, meaningful calculations regarding the mass concentration were challenging. The prevention of nonspecific adsorption of proteins leads to a met requirement in bio sensing applications. The limited BSA adsorption on cellulose surfaces is reported in literature as well.[46]

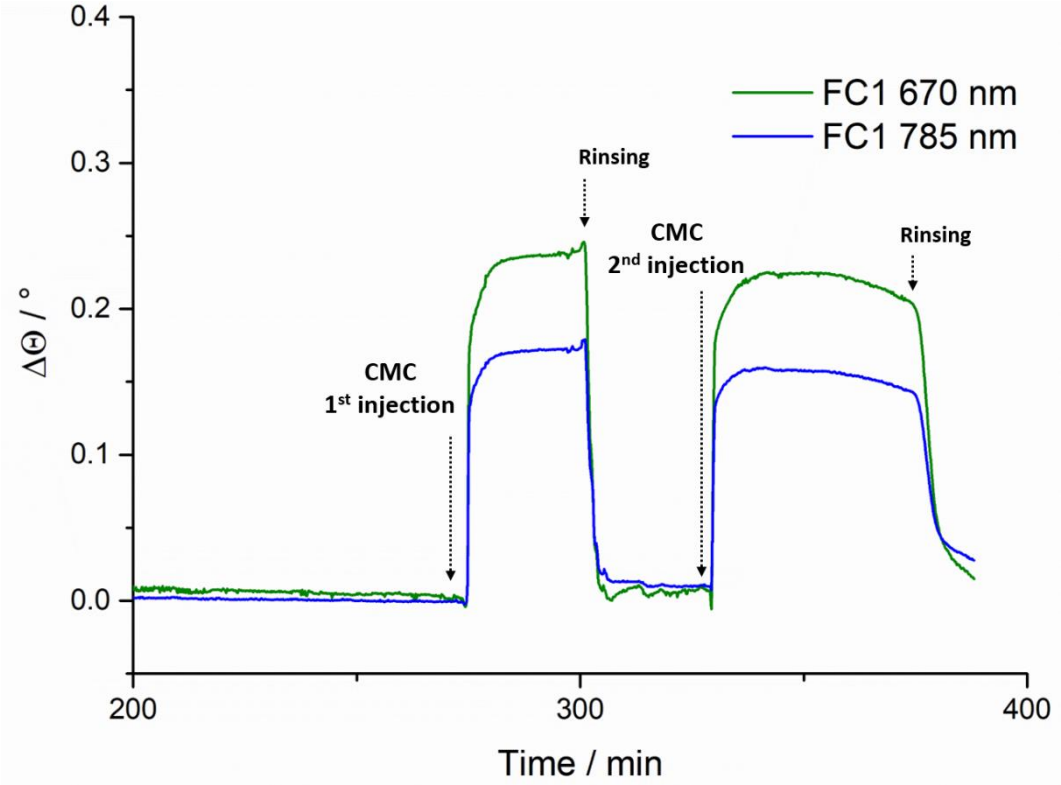

Figure 45: time resolved sensorgram of CMC adsorption on regenerated cellulose, which was initially equilibrated in NaOAc buffer for 12 h.

The enrichment with carboxyl groups enhances the amount of adsorption, therefore the behaviour of a CMC coating was investigated on a similar treated cellulose surface. Prior to the measurement the cellulose layer was stabilized for 12 h in a NaOAc buffer with pH 5 and the CMC was dissolved the same amount of time.[46] After equilibration, CMC was injected for 15 min. Afterwards, the system was flushed with MilliQ water to verify the reported dissociation behaviour.[19] This process was repeated two times to evaluate reproducibility, summarized in Figure 45. The angular shift after the 1st injection is (0.23±0.04) ° for the 670 nm laser, resulting in a calculated surface concentration of (1.5 ± 0.2) mgm^{-2}. Rinsing results in a new shift, of under 0.004 ° in regard to the original baseline, suggesting the reported dissociation of CMC with distilled water. After the 2nd CMC injection (at 328 min), the SPR angle again shifts to values of (0.22±0.04) °indicating similar adsorption concentrations. Reported masses for CMC on cellulose also gained via SPR are (2 ± 0.2) mgm^{-2}[46]. The small difference could be attributed to water coupling of the carboxyl groups. Furthermore buffer jumps and spikes can be seen before the first rinsing step (300 min).[22] Such a behaviour is an indicator of a not perfectly clean tube system, but are not relevant for the mass concentration considerations. When using a NaOAc buffer with pH 4-5, instead of MilliQ, the CMC layer binds irreversibly to the cellulose surface as reported. [19]

To investigate the adsorption behaviour of BSA on CMC, a measurement on a similarly treated cellulose surface was performed. After the CMC adsorption, rinsing with buffer was done until equilibrium was reached. BSA was injected for 15 min followed by equilibrating in buffer. In the last step Anti-BSA was injected. Figure 46 shows the corresponding sensorgram.

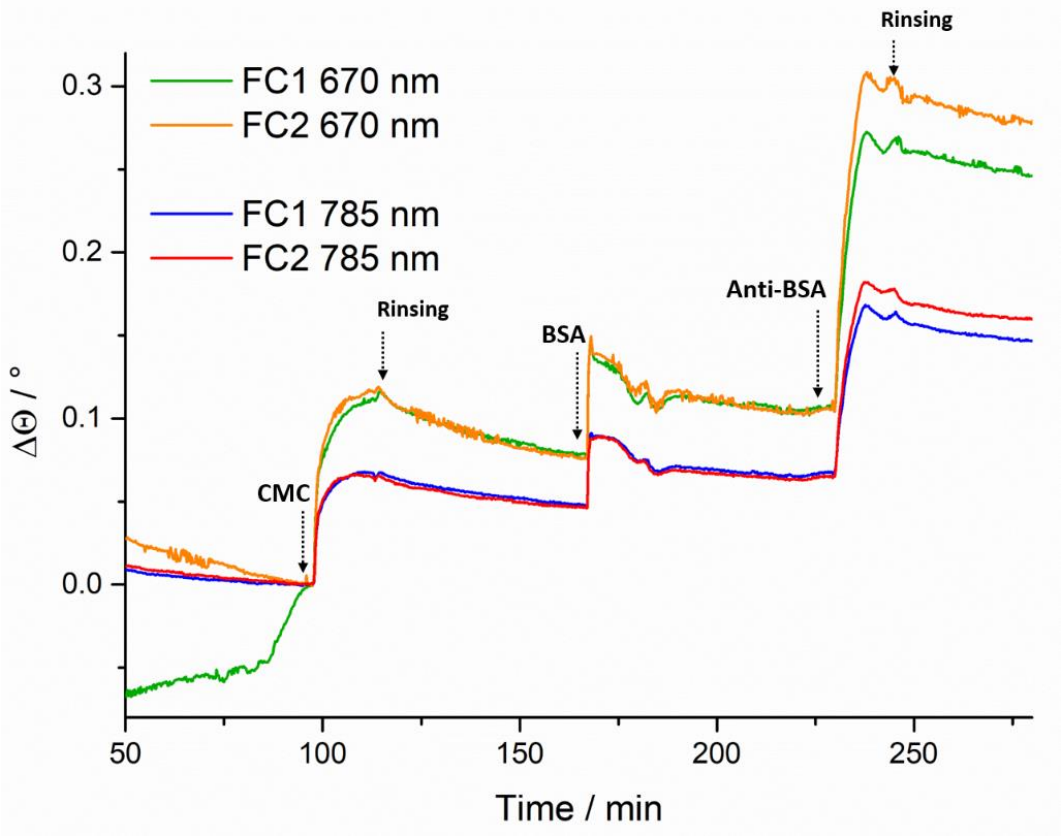

Figure 46: sensorgram of the successive adsorption of CMC, BSA and anti-BSA on a cellulose substrate in NaOAc buffer from both flow cells (FC1 and FC2) and at both laser wave lengths.

CMC injection results in an angular shift of (0.07 ± 0.04) °. This leads to a mass concentration of (0.5 ± 0.3) mgm^{-2}. Compared to the previous adsorption and to the reported surface concentrations, it is significantly lower. After BSA injection, the shift stabilizes at (0.03 ± 0.02) °. Corresponding mass concentration of (0.2 ± 0.1) mgm^{-2}, which is notably more than on the pure cellulose thin film. This demonstrates an influence of the CMC regarding BSA adsorption. Adsorbed masses for similar conditions of approximately 2 mgm^{-2} are reported for BSA on CMC adsorption .[46] Evaluating the absorption of anti-BSA onto the BSA results in a shift of either (0.24 ± 0.01) ° for the first flow cell (green) or (0.27 ± 0.01) °. The difference in signal possibly can be assigned to different equilibrations in the individual flow cells. The concentration of the adsorbed mass of anti-BSA is (0.9 ± 0.2) mgm^{-2}. It is evident, that more anti-BSA than BSA adsorbs on the surface.

Furthermore, regarding the signals themselves following observations can be made. For the 670 nm signal in the FC1, a different equilibration behaviour compared to the others can be observed (up to 100 min). From this point on, both signals from both flow cells overlap. Fast rising during BSA injection (at 170 min) indicates a high association constant. The sinking signal during injection could stem from a mass transfer limit, where the diffusion of the molecules to the surface and the actual binding are not equally fast resulting in a deficit of binding molecules on the surface. During anti-BSA injection, the overlapping of the signals stops, interestingly. Also, the combination of fast association and slow dissociation suggests strong bonding between the two macromolecules. Anti-BSA seems to bind on more than just the BSA macromolecules, or more than one binding event happens per BSA. The last kink

in the anti-BSA adsorption looks similar to the one after BSA, but more pronounced. The change in refractive index from buffer containing molecules to pure buffer could be the cause of it.

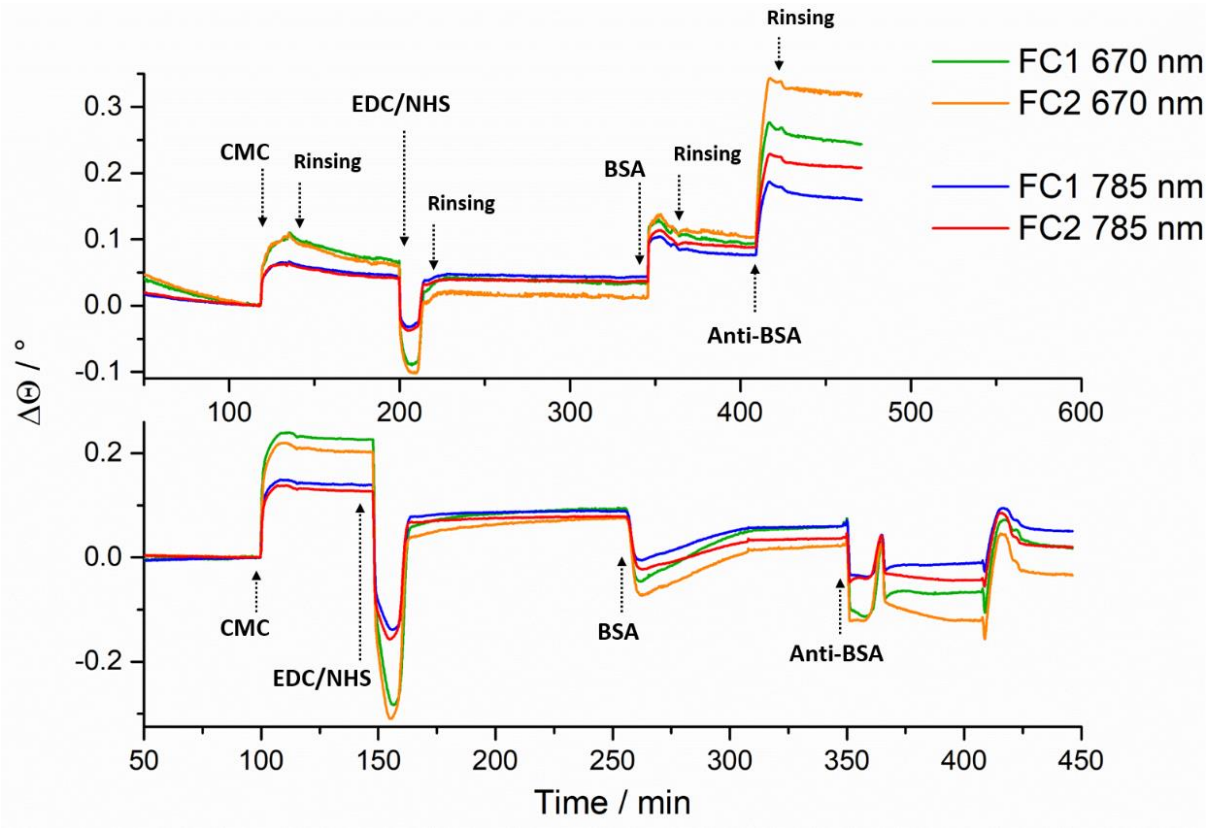

Figure 47: Sensorgram of the successive adsorption of CMC, EDC/NHS, BSA and anti-BSA in NaOAc buffer (top) and $CaCl_2$ buffer (bottom). In both cases the EDC/NHS step failed.

In order to covalently bond BSA on the CMC surface EDC / NHS chemistry was employed as an additional reaction step. Figure 47 shows the sensorgram of two experiments, performed similarly as described above once in NaOAc buffer (top) and $CaCl_2$ buffer (bottom), both with a pH value of 5 (adjusted with HCl). The SPR angle shifts to a lower value than the equilibration line, even though it should be shifted to a higher angle, since EDC and subsequently NHS, was adsorbed onto the thin film. A reason therefore could be the use of an old chemical which was stored at ambient conditions, the EDC might be hydrolysed. In both experiments again, successful adsorption of CMC on cellulose was observed. Using NaOAc buffer led to a shift of (0.07 ± 0.03) °, resulting in a mass concentration of (0.5 ± 0.3) mgm^{-2}, which is in good accordance with previous measurements. The system equilibrated in $CaCl_2$ shifted the SPR angle by (0.21 ± 0.03) ° corresponding to a mass concentration of (1.3 ± 0.3) mgm^{-2}. This again coincides with literature.[19]

The SPR response for EDC / NHS shifts to lower values, which usually happens during regeneration. This is presumably due to a differently changing refractive index. In the case of NaOAc buffer (top), the angle shifts by (0.2 ± 0.1) ° in negative direction during injection and eventually stabilizes at a value between the initial and the CMC-base line at (0.3 ± 0.1) °. This indicates some change on the surface, probably regarding the previously adsorbed CMC. With the $CaCl_2$ buffer the negative shift reaches a maximum at

(0.5 ± 0.1) ° and also stabilizes between the cellulose and CMC bases, meaning that a certain permanent difference in refractive index remains. The CMC layer is clearly influenced due to the hydrolysed EDC.

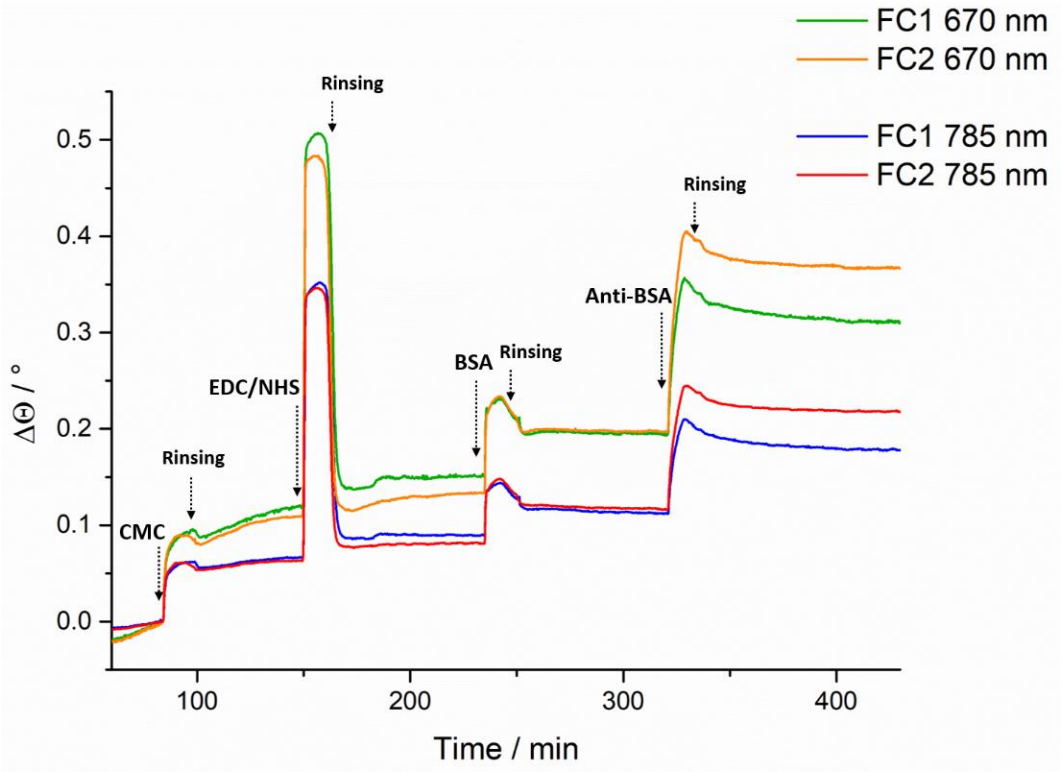

Figure 48: sensorgram of the successive adsorption of CMC, EDC/NHS, BSA and anti-BSA in NaOAc buffer.

To investigate the influence on the protein bonding, in both experiments, BSA followed by anti-BSA injections were performed. In the case of NaOAc buffer, the obtained concentration of BSA on the surface is (0.4 ± 0.3) mgm^{-2}, which is higher, than for the purely with CMC coated surface. In addition, the amount of adsorbed/bonded anti-BSA yields similar values as in the previous experiment, namely (1.1 ± 0.3) mgm^{-2}. Another mutual aspect between this measurement and the one with only CMC is the spreading of the signals during anti-BSA injection. Concerning the system in $CaCl_2$ buffer, a mixture of unspecified chemical and physical interactions happen. The magnitude of the highly undefined reactions challenges meaningful interpretation of the results. In contrast, Figure 48 shows a successful EDC / NHS adsorption under similar conditions in a NaOAc buffer, with newly purchased EDC, which was stored under inert conditions. Followed by the macromolecule adsorptions of BSA and anti-BSA, the layer systems build up can be seen in this graph. At this point, the reproducible adsorption of CMC with a mass concentration of (0.6 ± 0.3) mgm^{-2} is confirmed with the third experiment. After EDC / NHS injection the signal shifts to a maximum of (0.49 ± 0.03) ° and stabilizes at (0.04 ± 0.01) ° after rinsing, with regard to the CMC line. The following BSA injection led to a SPR angle shift of (0.05 ± 0.01) ° corresponding to a mass concentration of (0.3 ± 0.2) mgm^{-2}. Comparison with the measurement without EDC / NHS suggests a slight increase in surface concentration, however within the error range a definite statement is not possible. The shift occurring after anti-BSA is (0.14 ±0.02) °. This leads to a calculated surface concentration of (0.8 ± 0.2) mgm^{-2}. A similar result was obtained in the experiment without EDC / NHS. The shift during injection of EDC / NHS indicates that numerous molecules were in solution,

passing by, thereby changing the refractive index and being flushed away and only a certain amount, possibly a monolayer, sticks irreversibly to the surface. Once again, the spreading of the signals during anti-BSA injection can be seen. This interesting change in signal was observed in every measurement where anti-BSA was absorbed. Although this could indicate a not evenly adsorption of the macromolecules onto the already bonded BSA proteins, but the fact that always the same laser gives either the higher or lower signal could also stem from a measurement system related issue. To compare if the surface roughness changes the adsorption behaviour in any way, the experiment was repeated with a regenerated TMSC film, which was dissolved in xylene and was therefore smoother (see 4.4). The procedure of the measurement was analogous to the above described one. Figure 49 shows the resulting SPR signal.

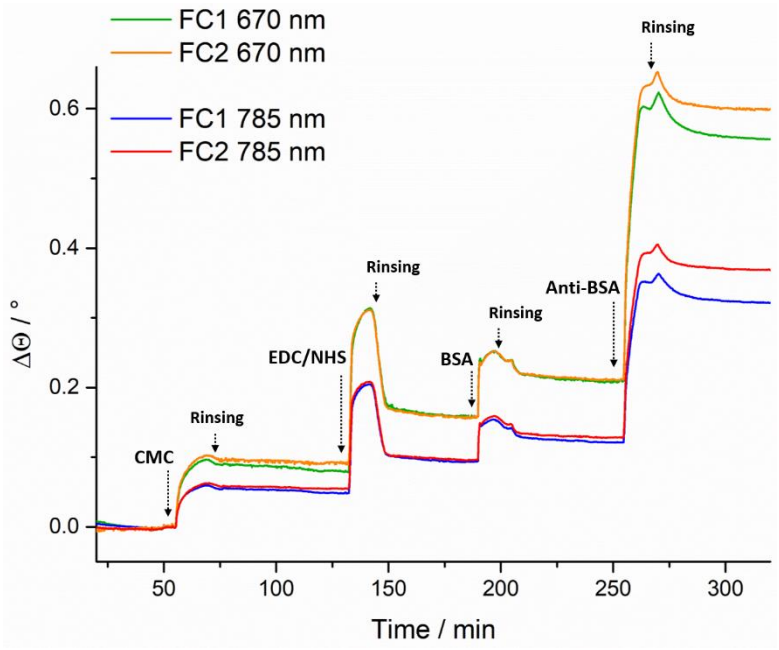

Figure 49 sensorgram of the successive adsorption of CMC, EDC/NHS, BSA and anti-BSA in NaOAc buffer on a cellulose substrate originally dissolved in xylene (2.23 wght%) instead of chloroform (0.75 wght%)..

The surface roughness did not seem to affect the CMC adsorption, since the angular shift again is (0.08±0.03) ° leading again to a surface concentration of (0.6 ± 0.2) mgm^{-2}. Regarding the EDC / NHS step, whilst the maximum shift of the angle is smaller in comparison, namely (0.22 ±0.03) °, the shift after rinsing and equilibration is (0.07 ± 0.01) ° and therefore higher in contrast to the previous measurement. The BSA turns again out to be (0.3 ± 0.1) mgm^{-2}, calculated from the recorded shift of (0.05 ± 0.01) ° after rinsing. Injection anti-BSA led to the highest surface concentration so far of (2.1 ± 0.1) mgm^{-2}.

Overall, the surface seems to react differently to the EDC / NHS adsorption. That the overall shift deflection was not as high as in the measurement depicted in Figure 48 can be because the weighing process in the glove box was subject to a fair amount of error. Therefore, the concentration of the solution was not the same and therefore the system equilibrates without being in real saturation. Because the angular shift is directly proportional to the mass per area, but not the thickness of the adsorbed layer. Again, the split of the signals only during anti-BSA bonding can be seen. It can be concluded that, successful adsorption/bonding of BSA and anti-BSA macromolecules was achieved with the used set up. Whilst absorption on cellulose resulted in no notable mass concentration of BSA,

introducing the CMC layer increased the absorption events to (0.6 ± 0.2) mgm^{-2} for every measurement. Introducing the EDC / NHS layer resulted possibly in a slightly higher mass concentration; however, the confidence interval limits conclusions that are more definitive. Interestingly, in any case, even with the failed EDC / NHS layer, the amount of bonded BSA remains similar. In addition, the anti-BSA surface concentrations stayed consistent throughout the measurements. Only in the case of the measurement on the smoothest surface (TMSC dissolved in xylene), the anti-BSA bonding doubled. Figure 50 summarizes these findings.

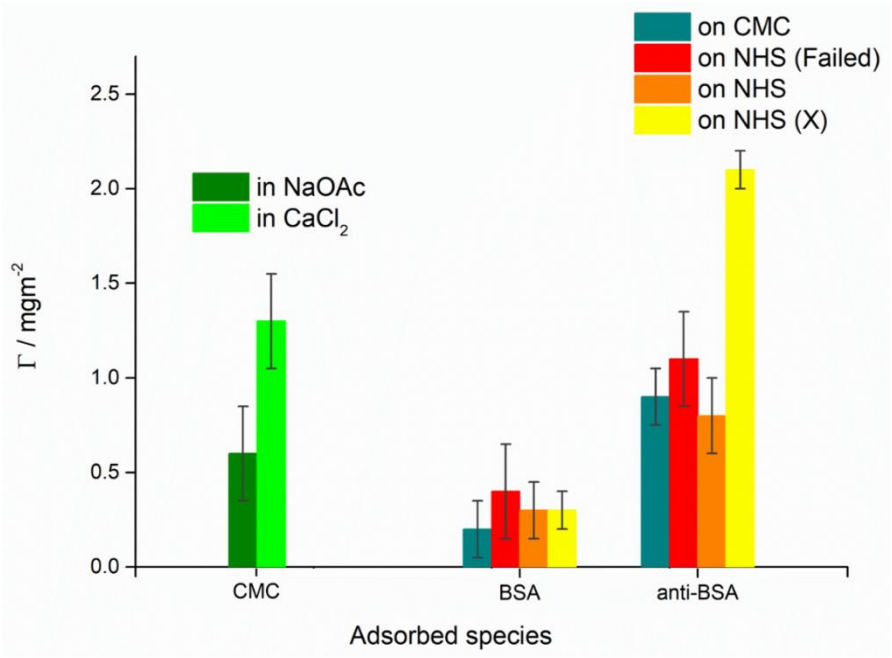

Figure 50: Summarized calculated surface concentrations. Amount of adsorbed CMC in a NaOAc buffer (dark green), in a $CaCl_2$ buffer (light green), amount of BSA and anti-BSA on CMC substrate (dark cyan), on the surface after failed EDC/NHS functionalization (red), on a successfully functionalized EDC/NHS surface (orange) and on a successfully functionalized surface on top of a cellulose basis, originally dissolved in xylene (yellow).

4.6 Liquid AFM Measurements at Different Adsorption States

While the chemical adsorption of individual layers has successfully been proven by SPR measurements, presented in the previous section, we now focus on morphological peculiarities using liquid AFM. First step on this route was the visualization of CMC adsorption on regenerated cellulose. Figure 51 shows the results in comparison to the original cellulose. Although the phase image does not indicate any changes caused by the scanning of the surface, looking at the recorded friction image of the largest scan size, the previously scanned area can be seen. Figure 52 shows the friction image of the 10 µm scan. In contact mode, the torque of the cantilever is dependent on the friction coefficient of the area it scans. In general, a higher signal correlates to a “stickier” surface then a lower signal. In this case, measuring in tapping mode, the interpretation of the obtained image is more challenging. However, qualitative adhesion/friction like changes were clearly observed after scanning an area, meaning some property of the surface was altered by the measurement itself. Investigating this interesting effect in more detail could complement current understanding of tip sample interactions. In comparison, the firstly scanned 500 nm image shows the friction like image during the primary measurement.

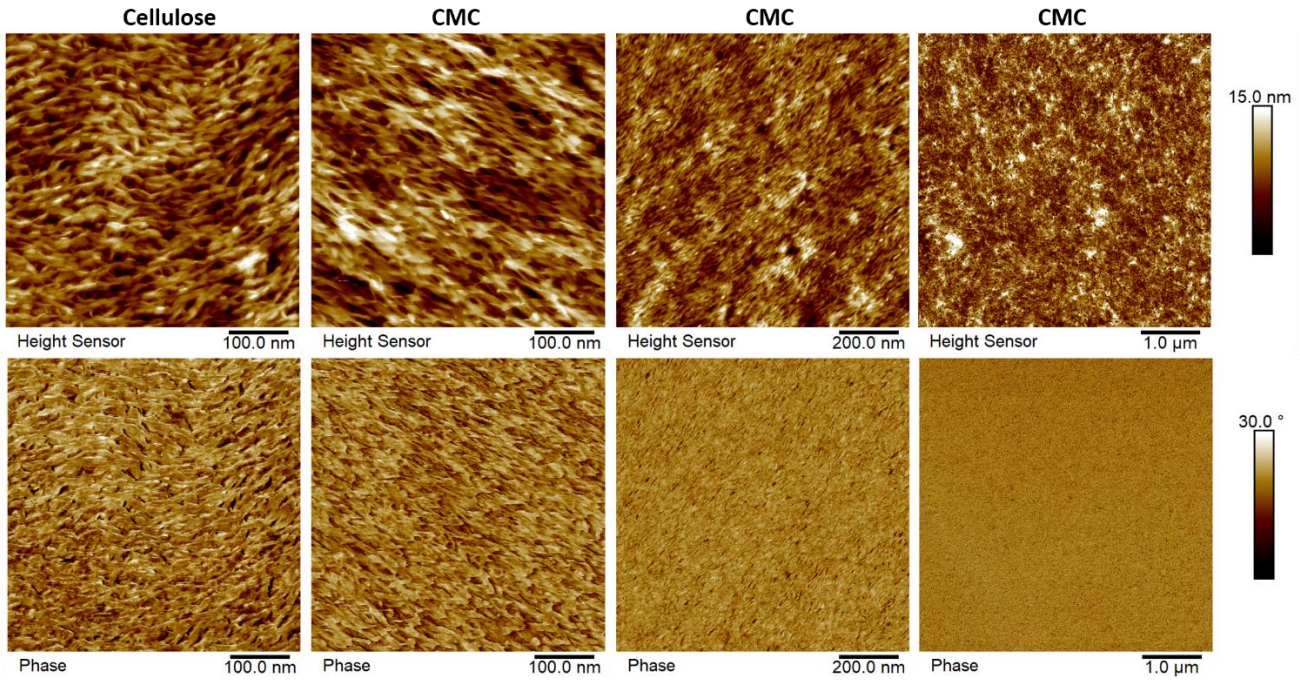

Figure 51: liquid AFM measurements height (upper row) and phase images (lower row) of regenerated cellulose and CMC modified surfaces (see frame indications) at different scan sizes for a general overview.

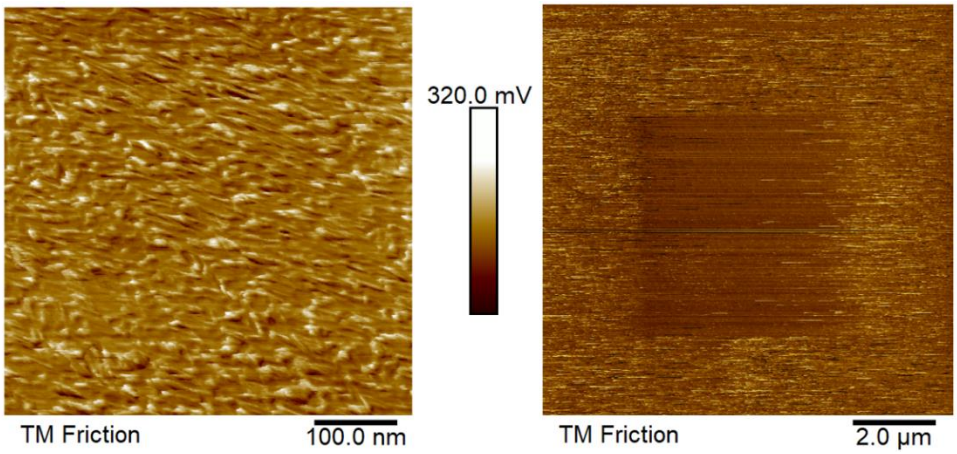

Figure 52 Left: Friction image of the 500 nm scan. Right: Arithmetically processed data of obtained friction image. Every data point (pixel) of the retrace and trace image was added, resulting in the displayed image, with a scan size of 10 µm.

Next, the samples were incubated with EDC / NHS solutions for 15 min, followed by AFM imaging, as summarized in Figure 53. As evident, slightly elongated features appear on the surface (see arrows) while the overall RMS roughness decreases from 2 nm to 1 nm. These features are 17 nm - 30 nm in lengths. Interestingly, the phase images do not show strong changes at related areas (see corresponding regions indicated by the arrows), which suggests that the entire surface was modified by EDC / NHS. To substantiate this assumption, a closer look on the morphology is given in Figure 54 by a side-to-side, in-scale comparison before and after EDC / NHS adsorption of CMC modified cellulose surfaces. As evident, the fine fibrils are widely gone, which supports the hypothesis that EDC / NHS is adsorbed across the entire surface as suggested by AFM phase image shown in Figure 53. In the next step, the film was incubated with a BSA solution for 15 min. Figure 55 shows the AFM results at two different scan ranges.

First, AFM imaging after BSA incubation turned out to be very complicated, reflected by many horizontal streak (see red arrows). Interestingly, however, was the observation that individual particles, which are often related to the streaks (see green arrows), were stable in their position and dimensions during multiple AFM scans. This strongly indicates loosely bound protein molecules, which are dragged and elongated but not removed by the AFM tip. This behaviour is not unusual for such tips and would require specific, chemical tip modification for prevention, which is beyond the topic of this master thesis.

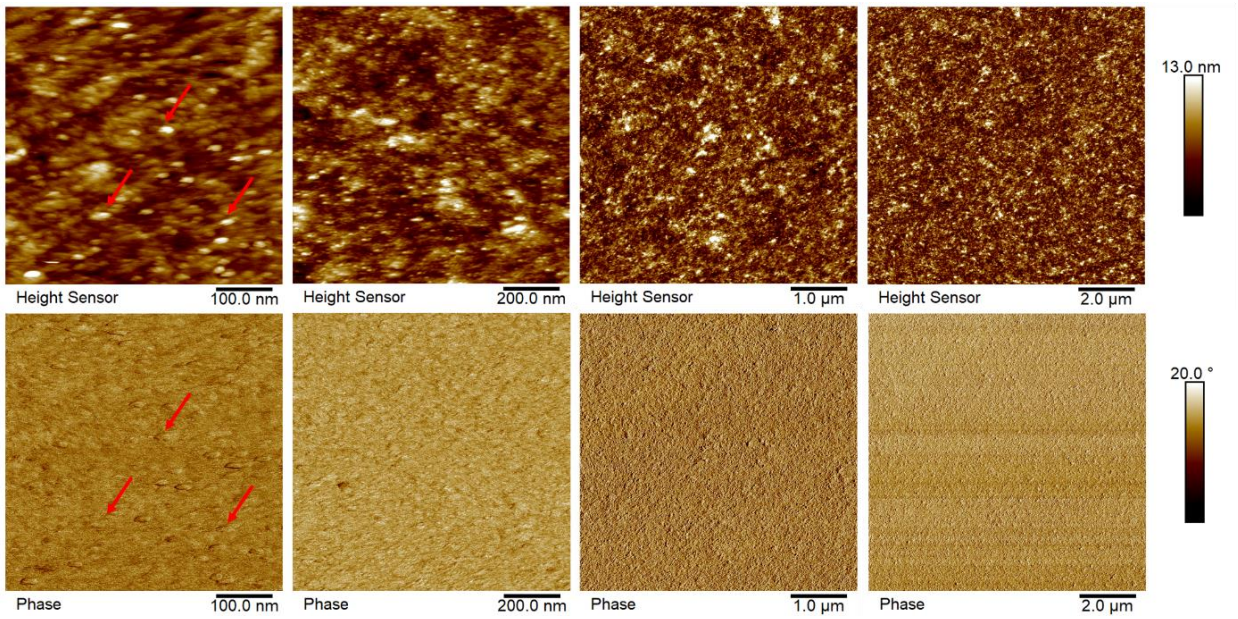

Figure 53: liquid AFM measurements height (upper row) and phase images (lower row) of CMC modified surfaces and after EDC / NHS adsorption for 15 min. (see frame indications) at different scan sizes for a general overview.

A close look at the phase image, however, reveal clear object shapes in agreement with the larger objects in height (see correlated green arrows). The slightly higher phase signals furthermore suggest those features to be different in chemistry. Measuring the dimensions reveal diameters in the range of 13 – 23 nm, which agrees with the reported BSA widths around 14 nm[12]. Together with the flying tip features, we can therefore assign the particles to adsorbed BSA molecules, which seem to be chemically bound as their position did not change.

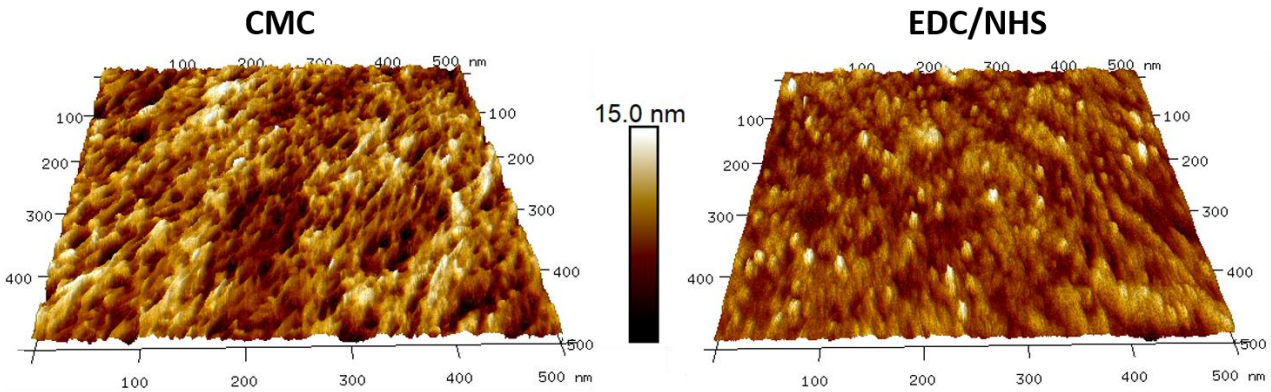

Figure 54: morphological in-scale comparison before (left) and after EDC / NHS incubation (right) of a CMC modified cellulose surface.

The involuntary interaction between the tip and a macromolecule imposes significant challenges during measurement. The change of surface or material of the tip can possibly result in a minimizing of this effect. Therefore, as mentioned before, chemical tip modification could result in better observability due to reduced measurement artefacts because of interactions, as reported in literature.[47–49]

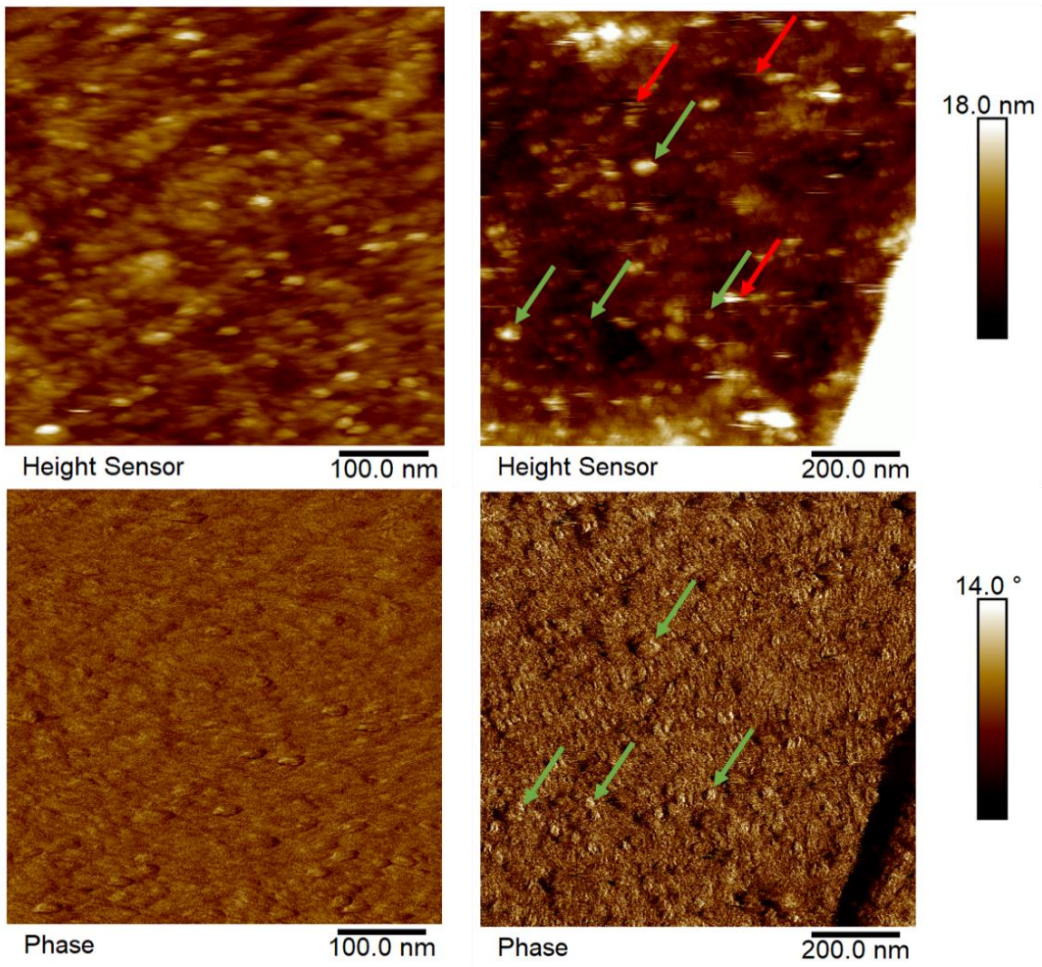

Figure 55: liquid AFM height (top) and phase (bottom) images before (left) and after BSA incubation (right) for direct comparison.

4.7 Nano patterning with Focused electron beam

In the last step, the local TMSC – cellulose conversion via focused electron beams was investigated as first demonstrated by Thomas Ganner[18]. As discussed in chapter 3.3.5, the advantage of this approach lies in the local vs. global regeneration character via electron beams and traditional HCL vapour conversion, respectively. As the process is complex, and different TMSC source materials were used by Ganner et al., we had to perform initial boundary test for confining the parameter sweet spot during focused electron beam induced conversion (FEBIC). In more detail, we first focused on the dose vs. conversion dependencies to estimate doses with under- and over-conversion. For this, TMSC is dissolved in chloroform with a concentration of 0.75 % and spin coated as described in 3.2.2 and 3.3.1. FEBIC pattern / array design and process parameters followed those by Ganner et al. and are listed in Table 2.

Table 2 FEBIC parameter

FEBIC Parameter		
primary electron energy	2	*keV*
beam current	53	*pA*
pattern sizes	2	μm^2
point pitch	10.39	*nm*
dwell times	0.1	*µs*
loop range	1 - 32	*passes*
doses	0.05 – 1.58	$C.m^{-2}$

Each patterning array consisted of 2 patterning fields with gradually increasing total doses ranging from 0.05 $C.m^{-2}$ to 1.58 $C.m^{-2}$, split in two 4 x 4 arrangement corresponding to doses of 0.05 $C.m^{-2}$ → 0.8 $C.m^{-2}$ and 0.8 $C.m^{-2}$ → 1.6 $C.m^{-2}$ (32 fields in total). As TMSC layers were very sensitive to e-beam exposure all patterns were exposed in a bling strategy, which required subsequent optical microscopy analysis, as representatively shown in Figure 56.

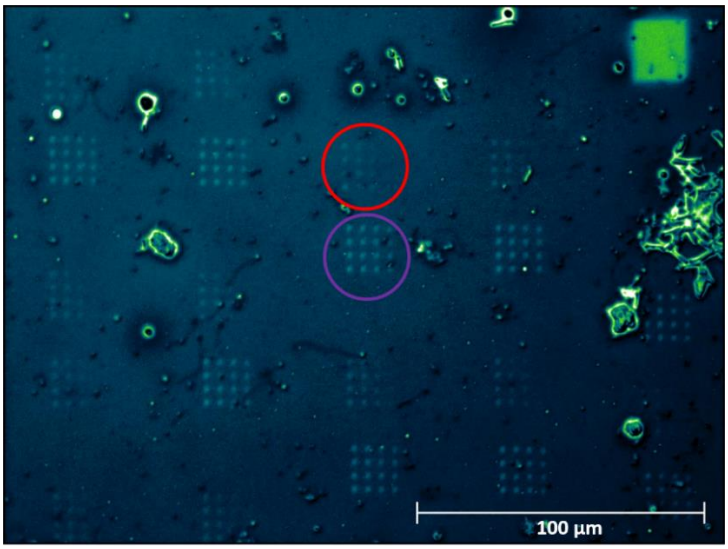

Figure 56: light microscopy image of a FEBIC processed TMSC layer, where the 4x4 patterning arrays are clearly visible. Each experiment consisted of two 4x4 arrays with low (purple) and high doses (red).

The low dose arrays are always above the high dose arrays. One of each is exemplarily marked with a circle (low dose: 0.05 $C.m^{-2}$ to 0.8 $C.m^{-2}$ (red), high dose: 0.8 $C.m^{-2}$ to 1.6 $C.m^{-2}$ (purple)). First observation was the optical change of all fields, which indicate the successful conversion away from TMSC although the low dose field is partly hardly visible (very low conversion). Furthermore, a purposely over regenerated area in the top right corner can be seen, which was done as an initial pre-test. To correlate the used doses with the amount of converted cellulose, we started with the film thickness characterization after FEBIC via AFM, representatively shown in Figure 57.

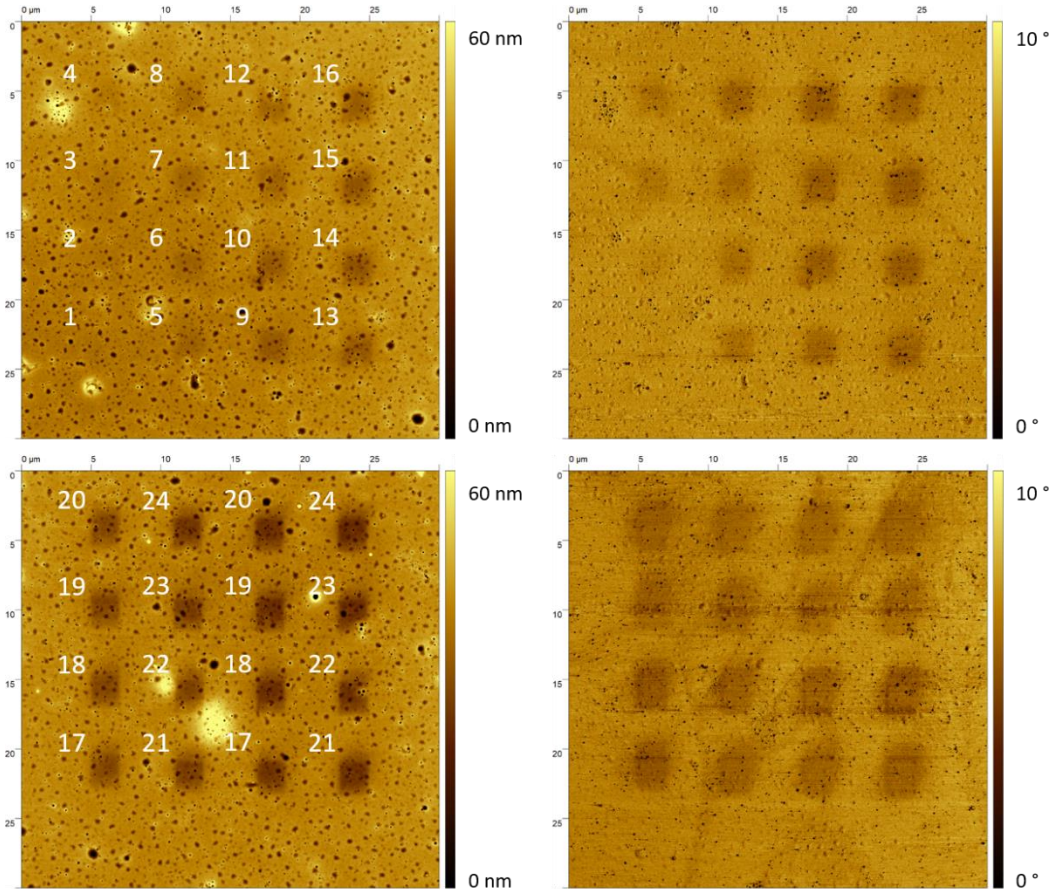

Figure 57: AFM height (left) and phase images (right) of a 100 nm thick, chloroform based TMSC layer after FEBIC with different doses. While the upper row shows the low doses of 0.05 – 0.8 C.m^{-2}., the lower row gives the results for the high dose range from 0.8 – 1.6 C.m^{-2}. The numbers give the increasing dose for orientation.

The arrays are clearly visible in both. As expected very low doses (1) result in almost no height loss, whereas higher doses gradually shrink, which is expected for the cellulose conversion process.[1] The material conversion effect is also reflected by the changing phase signal (right images). However, measuring reliable height losses was challenging due to two reasons. Firstly, the very porous nature of the TMSC film introduces a roughness, which, especially at low doses, exceeds the actual depth of the area. Additionally, the bottom regions of the patterned areas were sometimes slightly tilted, as clearly evident in a close up analyses in Figure 58 (red and green lines in the right hand graph). Therefore, assumptions about the average depth must be critically evaluated in the following. For further measurements, every array was divided into four subarrays and measured with a tip velocity of 5 µm/s. The height profiles of the arrays were measured horizontally and vertically, averaged over 45 pixels. Because of the high porosity, straight-forward line profile analysis was not possible, therefore, every profile was fitted with a Gaussian function and double checked with each cross section to provide highest possible reliability for this situation.

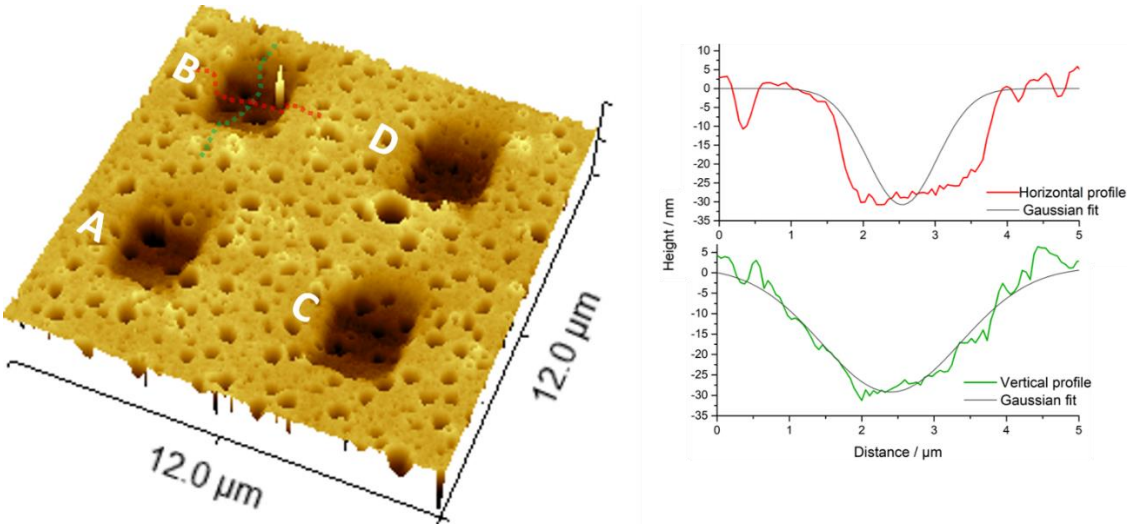

Figure 58: 3D AFM height image of 4 FEBIC patterns corresponding to 0.84 C.m-2(A), 0.88 C.m-2(B), 1.08 C.m-2(C) and 1.14 C.m-2(D). The cross section profiles of field B are shown at the right, together with the fit routine for depth determination.

The mean peak of the Gaussian fit was then taken as determined depth. Figure 58 shows an 3D image of the doses 0.84 $C.m^{-2}$(A), 0.88 $C.m^{-2}$(B), 1.08 $C.m^{-2}$(C) and 1.14 $C.m^{-2}$(D). For the dosage 0.88 $C.m^{-2}$, the evaluation of the depth of an array is shown in two different directions (red and green line), quantitatively shown in the right graphs. As evident, that the surface roughness, in particular the unavoidable pin-holes, complicates and eventually limits the accuracy of the obtained data. Moreover, it can be seen, that measuring the height profile horizontally results in steeper and smother walls compared to the vertically measured ones. This was observed for every dosage and can be attributed to charge drift effects during FEBIC.

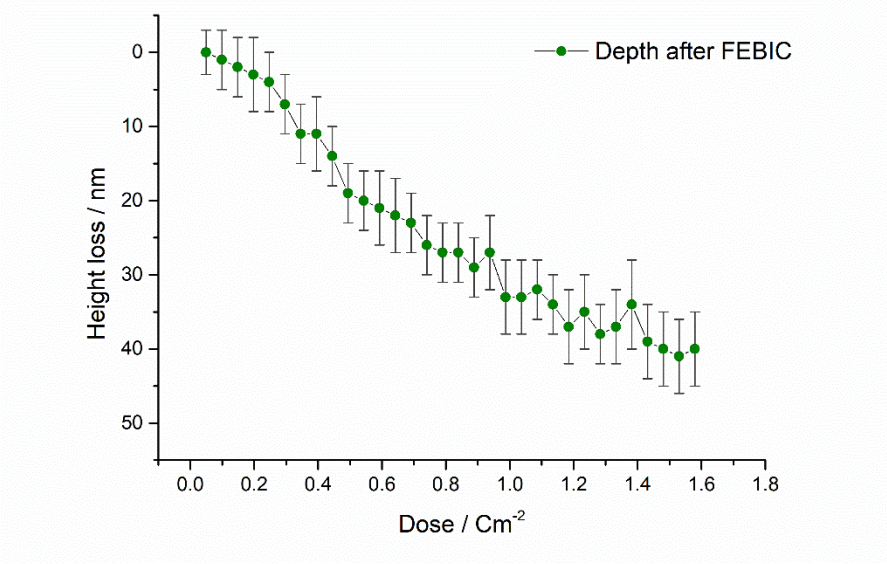

Figure 59 Height loss versus applied electron dose.

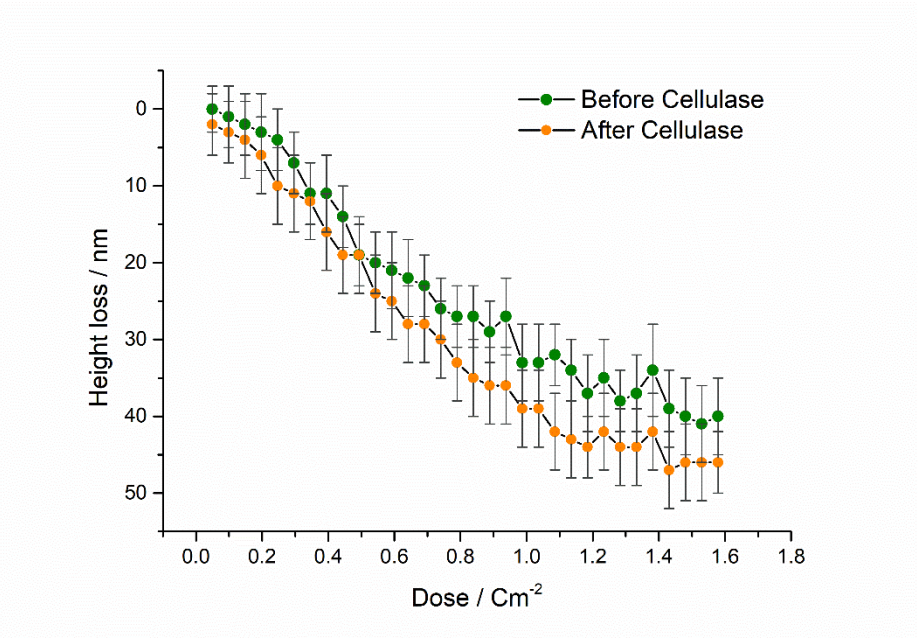

Figure 60: Height loss vs. electron dose before (green) and after (orange) cellulase incubation for 12 h.

After evaluating all patterns, one obtains a height loss vs. dose graph, as shown in Figure 59. Although the height loss reveals slight saturation tendencies above 1.4 $C.m^{-2}$, it is not possible to determine either the ideal dose or the point of over conversion, due to the large error bars. The steep height loss up to 0.5 $C.m^{-2}$ and an ideal electron dose at which the maximum of conversion happens at 0.8±0.2 $C.m^{-2}$ are reported by Ganner et al. as well.[18] Despite this slightly different result (no clear saturation is found), we next incubated the converted fields with a cellulase solution (SVG17 diluted 1:10 in NaOAc with pH 5) for 12 h. This enzyme only disassembles pure cellulose, while leaving TMSC completely unaffected. Hence, any additional height loss can be clearly attributed to the converted cellulose and by that to a successful FEBIC process. The comparison of the first experimental run is shown in Figure 60. It seems that the cellulose enzyme dismantles some amount of the FEBIC treated material as intended. Additionally, it can be seen, that the increase in depth stops at around 1.4 $C.m^{-2}$ as already suspected before. This would indicate the point at which over-conversion leads to some other carbon structure than cellulose, indigestible by the cellulase. As mentioned before, the high insecurity stems from the pin-hole morphology, which is a typical feature in chloroform films. Following the findings in chapter in chapter 4.4, we therefore, repeated the experiments with xylene based TMSC films using the high concentration of 2.23 wgth. % to realize the 100 nm film thickness. Furthermore, we expanded the upper dose range to 2.37 $C.m^{-2}$ based on the weak saturation tendencies without a clear minimum in the first chloroform run. The biggest difference in the surface properties in comparison to TMSC dissolved in chloroform, was the smoother overall character without any pin-holes as shown in Figure 61 by an AFM height image after FEBIC for a dose range of 0.8.X $C.m^{-2}$ → 1.6 $C.m^{-2}$, indicated by A → P.

After incubating such films with cellulase under same conditions as for the chloroform based TMSC films, AFM was again used for accessing the height losses before and after. The result is shown in Figure 62, now revealing a much clearer view on the conversion situation.

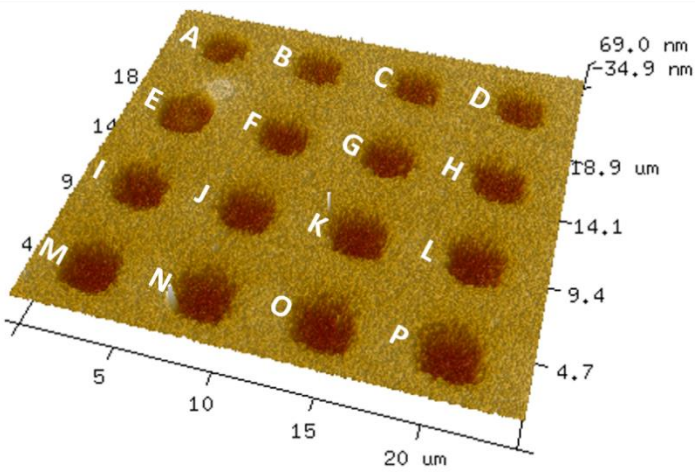

Figure 61: 3D AFM height image of a 100 nm xylene based TMSC film after FEBIC. The doses ranges from 0.8 C.m^{-2} -1.6 C.m^{-2} as indicated by the latters (A → P).

As evident, there is now a clear trend: first, the curves are lying over each other up to a dose around 0.3 C.m^{-2}, indicating no cellulase activity and by that the absence of cellulose materials converted by the e-beam. After that threshold, depths shear apart until it gets constant around a dose of 1.4 C.m^{-2}. This is a clear indication that the FEBIC worked out the intended way in agreement with previous experiments. The ideal dose can therefore be found in this region. For even higher doses, the cellulase is apparently not causing any more height loss, which clearly reflects an over-conversion in non-cellulosic materials. Nevertheless, there are small decreasing tendencies even at higher doses, which we attribute to the formation of small carbon fragments, which were washed away during cellulose rinsing. This idea is supported by the fact that the AFM measurements of the individual arrays turn out to be challenging due to constant tip contamination and unstable phase despite high enough force, which tends to happen with loose particles. Figure 69 shows a different representation of the results. The relative height losses over the used doses can be seen, taking the initial height loss after FEBIC as base. For more detail, see below.

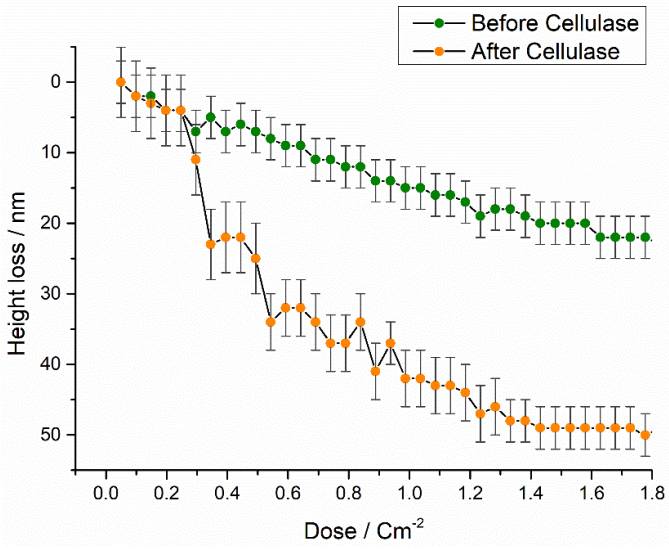

Figure 62: height loss vs. FEBIC doses based on AFM evaluation before (green) and after cellulase incubation (orange). As evident, there are three different ranges (identical → decay → saturation) as discussed in the main text

Another interesting effect can be observed when having a close look at the morphology of high-dose FEBIC patterns. Figure 63 shows 4 patterns between 2.0 C.m^{-2} and 2.3 C.m^{-2} before (left) and after (right) cellulase incubation. As evident, not only the actual pattern regions but also areas around them were degraded by the enzymes. This effect can be attributed to backscattered electrons during FEBIC, which re-exits outside of the pattern, leading to additional conversion into cellulose. The dose in that region is clearly lower than within the pattern, meaning that the conversion degree is lower than for central areas. As evident, the outside regions were clearly attacked, which confirm the conversion into cellulose as expected. The reason why we present this data is the fact that backscattered electrons limit the achievable lateral resolution as suggested by Ganner et al.[18] As discussed later, reducing the primary electron energy is one possible route to reduce lateral broadening, thus increasing the achievable resolution during FEBIC.

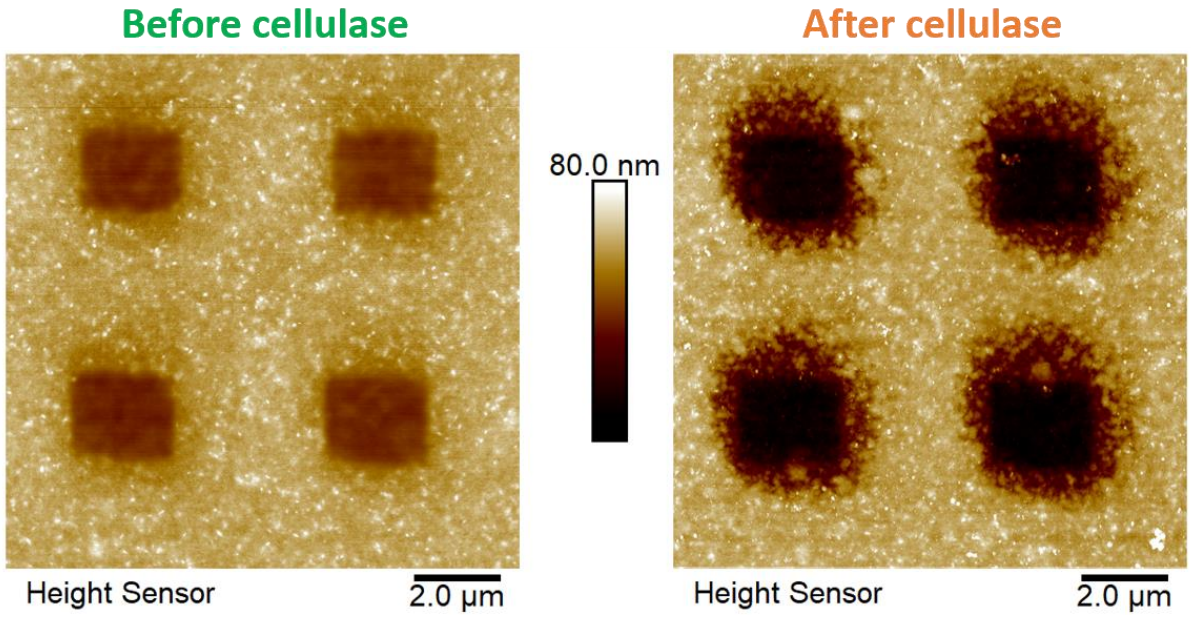

Figure 63: AFM height comparison of xylene based TMSC films after FEBIC processing at doses between 2.0 C.m^{-2} – 2.3 C.m^{-2}. While the left image shows the film after FEBIC, the right image gives the result after cellulase incubation, which reveals degradation outside the intended pattern region as a consequence of backscattered electron induced conversion.

Next, we studied the chemical signatures of the converted films at different FEBIC doses. For that, TMSC films were spin cast on gold substrate, and exposed to selected FEBIC doses on large areas of 80 x 80 µm^2. Each of them has then be characterized via infrared spectroscopy, summarized in Figure 64 by offset spectra for more clear comparison.

The intention here was to reveal at which doses the patterns lose the bands, primarily focusing on reduced Si vibrations (TMSC splitting) and increasing OH bands (cellulose formation). As evident, even the Si-O-C and Si-C vibrations at 800 cm^{-1} and 1250 cm^{-1} do not entirely disappear even for high doses around 1.57 C.m^{-2}. Additionally, an OH vibration band arises and gets larger for higher doses. This indicates, that independently of the dose, there were always TMSC but also cellulose components in the FEBIC patterned areas although the ratios may change. Interestingly, another C=O vibration band

appears at 1750 cm^{-1}, which can neither be found in TMSC nor in cellulose, because neither structure contains double bonded oxygen.

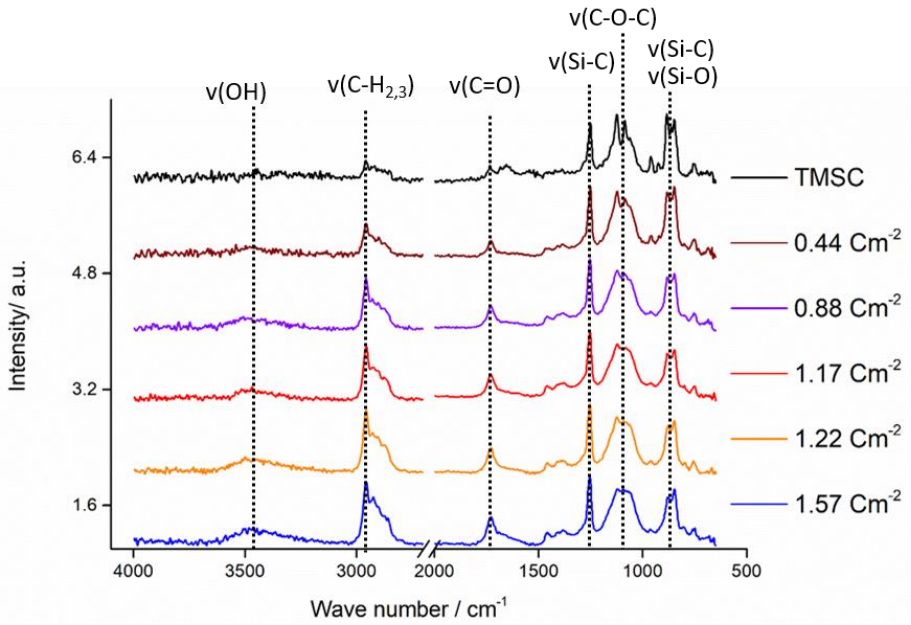

Figure 64: IR spectra of FEBIC processed 80 x 80 µm² areas at selected e-beam doses.

As this band is also present in the lower doses, it is not very likely that it is an effect of over conversion. More likely, additional processes take place, creating double bonded oxygen as by-product. For this thesis, however, we ignore this bands and shift a detailed study to a follow-up master thesis. The bands at 1000 cm^{-1} and 2950 cm^{-1} are both associable with either TMSC or cellulose and are expected because of the cellulose backbone. To compare the patterning technique with the window mode (see methods), the doses were patterned again into the substrate, using the whole imaging window instead of a small window.

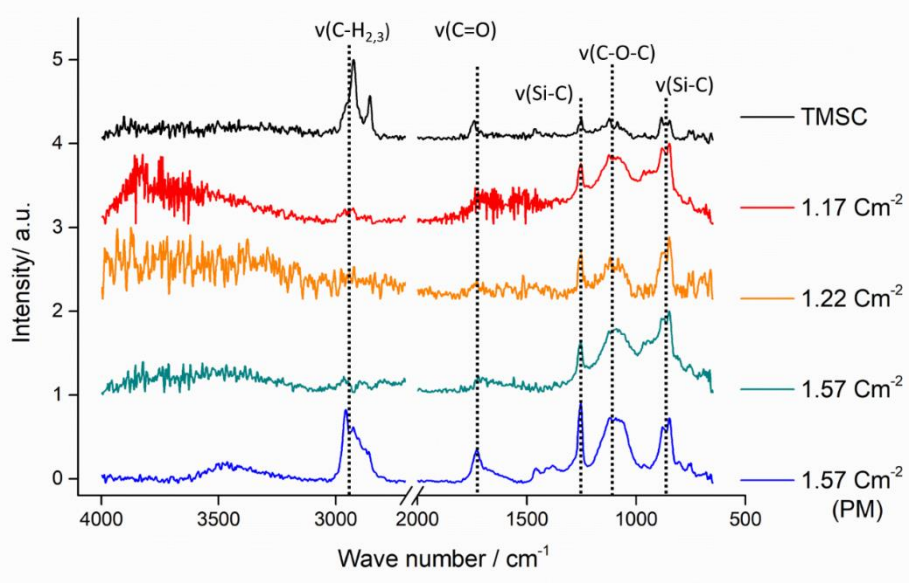

Figure 65: selected IR spectra of structures applied with the window mode instead of specific region patterning (1.57 Cm^{-2} in patterning mode (PM) spectrum for comparison in blue).

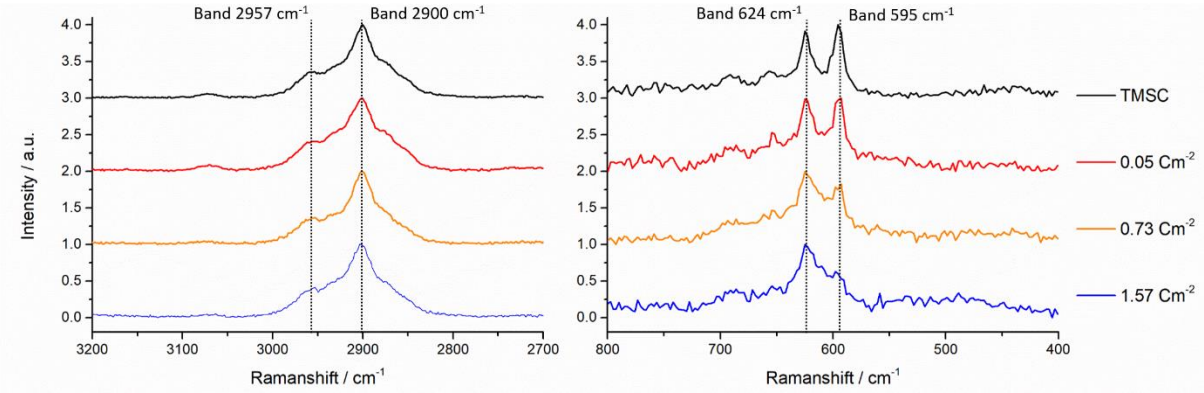

Figure 66: Raman spectra of 80 x 80 µm² large FEBIC processed regions at different doses.

Figure 65 shows the collected spectra together with a selected region pattern (shown in blue). The strongest difference between patterning and window mode is found at the 2925 cm^{-1} band, corresponding to CH_3 vibrations. While in the patterning mode, that band is still there for 1.17 $C.m^{-2}$, it cannot be found for the window mode. Hence, the latter seems to result in a more homogeneously pad of converted cellulose. This is most probably due to the limitation of the number of points, which can be addressed by the patterning engine. Additionally, the approach of stringing together squares introduces over lapping areas as well as possibly skipped areas, which explains the overall differences very well.

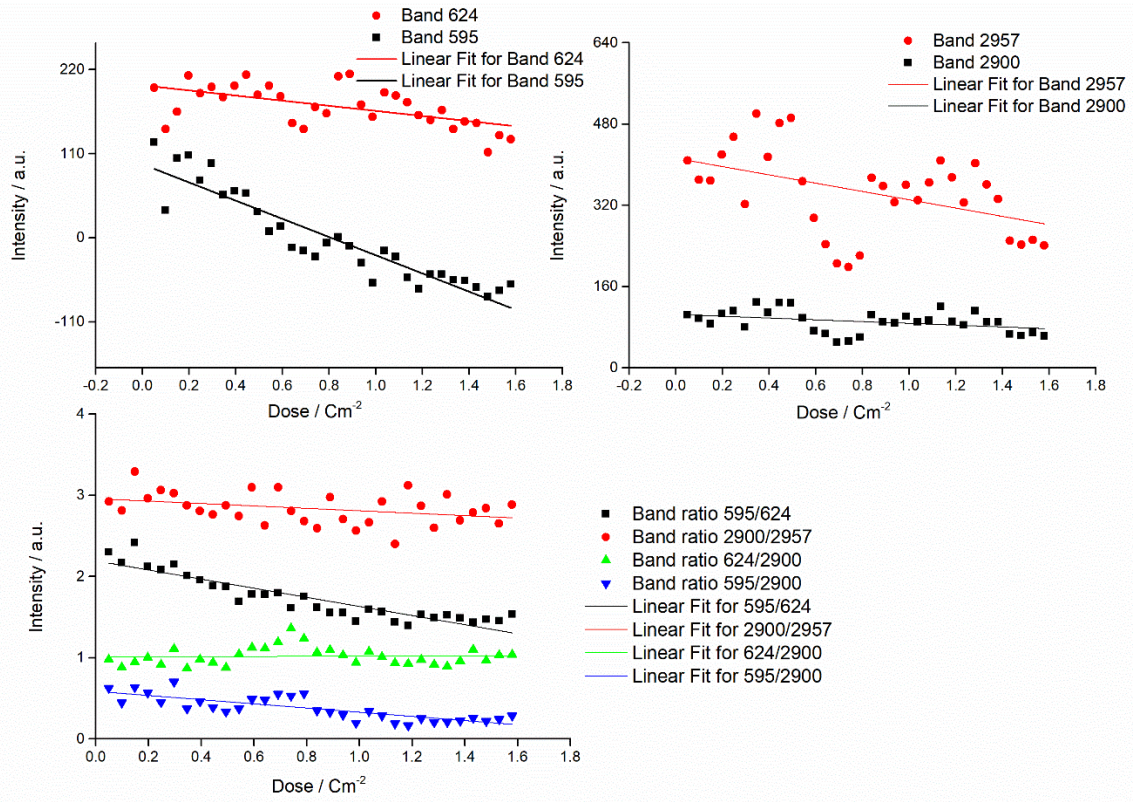

Figure 67: Band intensities of the identified stretches over the FEBIC dose. Absolute lowering of the bands at 624 cm^{-1} and 595 cm^{-1} with linear fit (top left). Absolute reduction of the bands at 2900 cm^{-1} and 2957 cm^{-1} with linear fit (top right). Different ratios between the obtained band intensities (bottom).

To study the chemical situation even further, we applied Raman spectroscopy for the same patterns. Measuring the spectra was challenging because they partly changed during recording them. This was only observed with the red laser (633 nm). It is possible that some surface effects were reinforced at this wavelength, because hanging to the blue laser (473 nm) resulted in stable signals. Here, the bands between 400 cm^{-1} and 800 cm^{-1} were no longer recordable. Therefore, the bands at high shifts were recorded with the blue laser first. After that the lower bands were measured with the red laser. The most relevant spectra are compared in Figure 66. Again, it can be seen, that low / high doses produce a uniform layer of cellulose. The bands at 2900 cm^{-1} and 2957 cm^{-1} are the symmetric and asymmetric stretches of C-H in a CH_3 structure[50], which only occurs in TMSC but not in cellulose. Also the bands at 624 cm^{-1} and 595 cm^{-1} can be attributed to TMSC, being asymmetric Si-(CH_3) stretching[51]. Figure 67 shows the normalized intensities of the bands at different doses. Furthermore, the ratios between different bands versus the doses can be seen.

Looking at the slope of the linear fit, the Si-(CH_3) stretching (bands 624 and 595) decreases with increasing doses, which means that the number of methylsilyl groups is indeed becoming less with more electron exposure (Figure 67, top left). The C-H stretches (2900 and 2957) seem to reach a minimum around 0.7 Cm^{-2} and the linear fit suggests an overall decrease (Figure 67, top right). Because the film thickness has an influence on the absolute intensity, it is often helpful to rather look at the ratios between bands (Figure 67, bottom). The slopes of the ratios 2990/2957, 624/2900 and 595/2900 show only slight reduction. The ratio 595/624 shows the biggest change, allowing the conclusion that the amount of TMSC definitely shrinks, but never disappears.

So far, we have AFM data which suggests a very good conversion into cellulose for specific doses, confirmed by the increasing and eventually stopping height decrease after cellulase incubation. On the other hand, IR and Raman spectroscopy suggest remaining TMSC as well as over-converted material in the patterned areas for a very wide range of doses. Keeping in mind, that spectroscopy is a method, which integrates the signatures along the entire Z axis, we can set up the hypothesis, that there might be a vertical gradient of under-, ideal- and over-converted TMSC. This requires a closer look to the FEBIC process. Considering the geometry of the interaction volume of the electrons in the TMSC layer, and the effect of backscattered electrons it is very likely, that there is a certain distance in Z at which ideal doses are generated. However, this also means that above and below this specific area under- and / or over-conversion takes place. This is in agreement that spectroscopy is not able to differ between vertical gradient, therefore having both signals in the same spectrum. To investigate this idea, a Monte Carlo simulation was done for a 100 nm TMSC layer on a Si substrate. 5000 electrons were simulated, to study the statistical distribution of stopping electrons along Z. The simulation is shown in Figure 68 at the left, showing a side view of electron trajectories with differentiation of re-exiting backscattered electrons in red. A statistical distribution is shown by histograms at the right, which reveals the maximum around 70 - 80 nm from top (20 – 30 nm from the bottom). From the histogram it becomes immediately evident that there is an electron density gradient along Z, which has to have implications on conversion. Now assuming a low overall dose, this could lead to the case of ideal conversion in the peak range, shaded green, while regions above and below are under-converted (shaded blue). Once the dose gets very high, the distribution remains widely the same, but the quantitative number of electrons increase. This could then lead to over-conversion in the peak range (shaded red), followed by ideal converted regions (green shade) and eventually under-converted regions. The result is a vertical gradient of the conversion degree and can explain the existence of all individual signatures in the IR / Raman spectra.

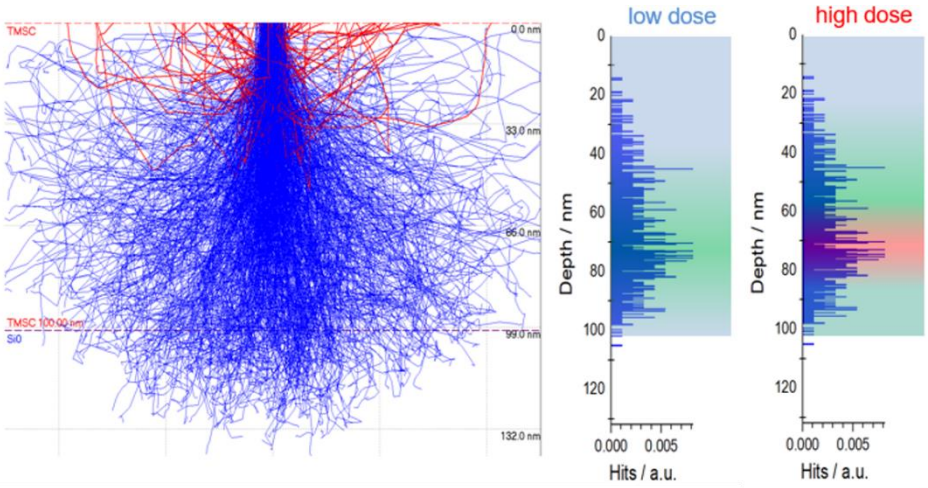

Figure 68: Monte Carlo simulation of electron paths in TMSC on Si substrates. The left image shows the electron trajectories in a cross sectional view with re-exiting backscattered electron in red. The right histogram is a statistic analyses of the Monte Carlo simulation revealing the stopping position of electrons, associated with lowest energies and by that with the highest conversion probability [REF]. The different shading (blue – green – red) is explained in the main text.

With this vertical gradient aspect in mind, we revisited the height loss data from Figure 62. Figure 69 gives the relative height losses vs. FEBIC dose after cellulase, which are corrected by the initial height loss after FEBIC (representing the new base before enzyme exposure). The three regions are immediately evident: 1) no height loss at very low doses, 2) strong height loss at intermediate doses and 3) saturation at doses around 0.8 $C.m^{-2}$ and 1 $C.m^{-2}$. The blue curve (left ordinate) gives the height loss rate with a distinct maximum around 0.3 $C.m^{-2}$. Both together can be interpreted as a lower and upper dose range for ideal conversion based on the vertical conversion convolution due to the before mentioned electron trajectory processes (see also right parts in Figure 68). Hence, it is safe to say that the ideal doses are somewhere between 0.3 $C.m^{-2}$ and 1 $C.m^{-2}$. The broad range is a consequence of the electron trajectories and barely avoidable with the here studied conditions. One way to narrow this dose band is the increase if primary electron energies, which should lead to a strongly reduced, though present, vertical conversion gradient, which will be in focus in a future master thesis.

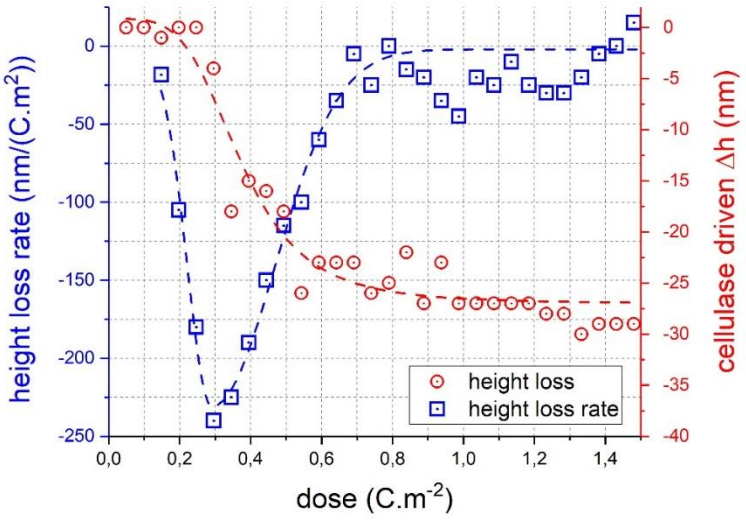

Figure 69: height loss and height loss rate analyses of Figure 62. The red curve (right ordinate) shows the cellulase driven height loss after subtraction of the initial FEBIC related height loss revealing a saturation behaviour starting between 0.8 Cm^{-2} and 1 Cm^{-2}. The blue curve gives the height loss rate, revealing a distinct minimum around 0.3 Cm^{-2}. The values are discussed in the main text.

Nevertheless, we tried to find the optimum dose for the here presented conditions as a first step. Background for these activities is the fact that the surface is more relevant than the underlying volume for our purposes, as we focus on the surface adsorption of BSA in the final stage. To find this, a FEBIC pattern was designed, where every shape can be directly associated with one specific dose. Again, the whole dose range of 0.05 Cm^{-2} to 1.6 Cm^{-2} was investigated. After FEBIC processing, the unconverted, remaining TMSC was washed away with the original solvent (chloroform or xylene). Ideally, only those patterns are washed away which "stand" on a TMSC base. This should leave only pattern where either cellulose or some over converted carbon structure as surface. In the next step, the structures should be measured via AFM for accessing height and shape information. As before, incubation with cellulase and comparison of the heights could indicate where cellulose is at the surface.

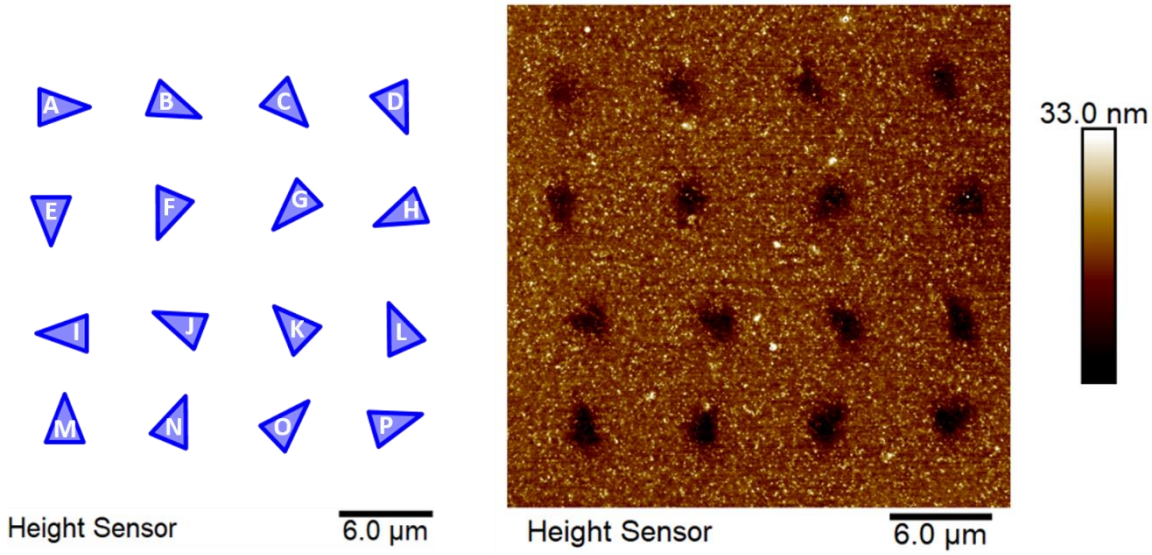

Figure 70: Advanced patterning design for subsequent identification of different FEBIC doses (left) and its appearance after FEBIC on xylene based TMSC films. The letters indicate the increasing doses ranging from 0.8 $C.m^{-2}$ (A) → 1.6 $C.m^{-2}$ (P).

Figure 70 shows the named pattern design (left) with increasing doses from 0.8 $C.m^{-2}$ to 1.6 $C.m^{-2}$, indicated by the letters A → P. The right part of Figure 70 shows the morphology after FEBIC processing using the triangular design. As evident, the triangles were recognisable for higher doses, while complicated to identify for low FEBIC doses. What is already evident are smeared out edges, which we traced back to unforeseen charging problems of the Si substrates. Nevertheless, we proceeded with the next step, which was removing the unexposed TMSC layer around the triangle by chloroform (not shown) and xylene. In more detail we exposed the samples for 12 h in the respective solution while slowly rotating to ensure a suitable flow. Finally, the film is carefully rinsed with MilliQ water and dried with CO_2. Remeasurement of the structure resulted in the unexpected outcome, that the triangle structures were still deeper than the surrounding surface, as shown in Figure 71 by height (left), phase (right) and cross-sectional profiles (bottom). The depth of the "structure" seems independent of the dose. Additionally, the roughness of the surrounding surface, being 4 nm, indicates, that residue TMSC is still on the surface. The phase image suggests qualitative material differences for the bottom row. Multiple reasons suggest themselves for the residue TMSC and the deeper structures. Possibly, this

particular batch of TMSC was dissolving differently because of a slight substitution degree variation. The more likely explanation, however, is that the material changes in ambient environment in a manner that prevents complete dissolution. The depth of the structures before the washing step and afterwards does not change significantly. This is a further indication for the resistance of the TMSC against dissolution.

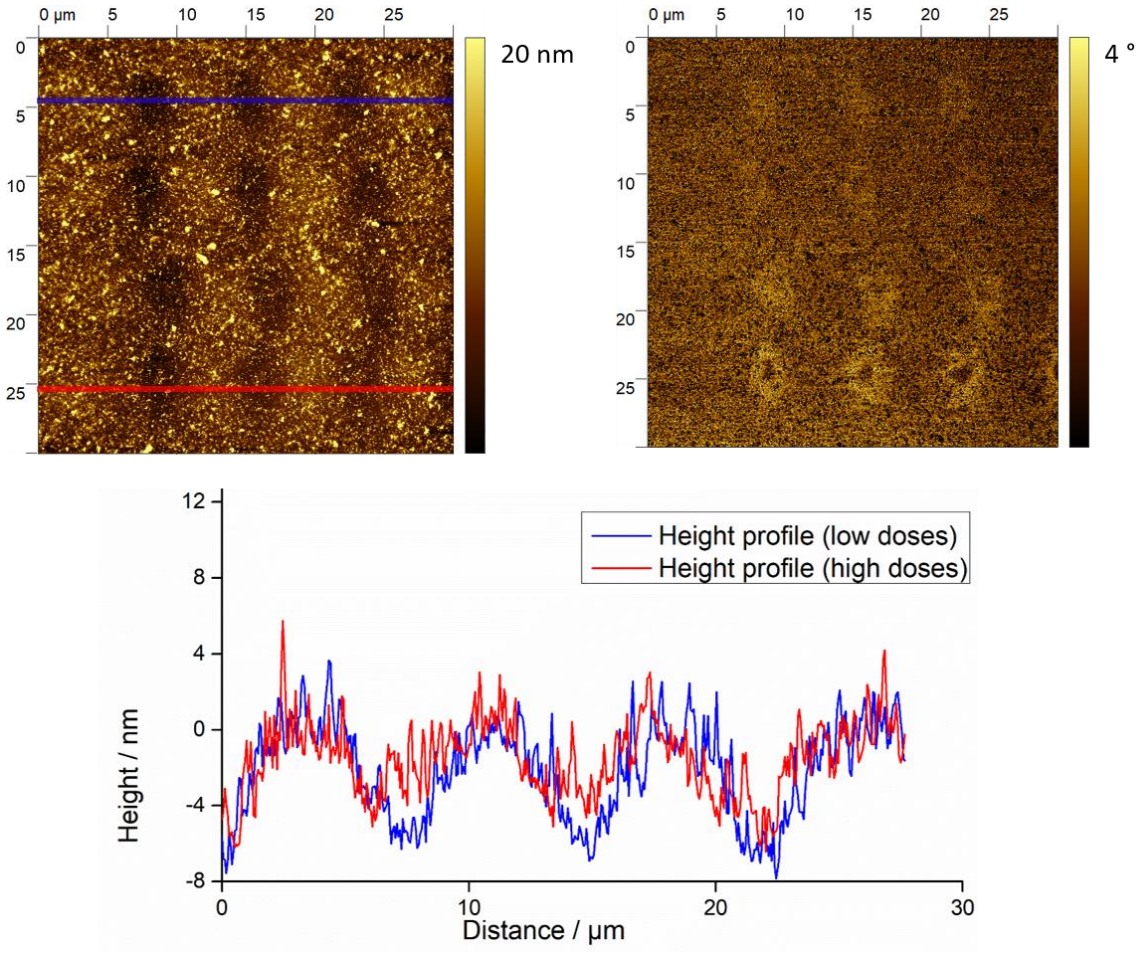

Figure 71. AFM analyses via height (top left) and phase imaging (top right) together with cross sectional profiles (bottom) taken at the indicated lines top left. Corresponding doses for the latter were 0.05 C.m^{-2} (red) and 0.79 C.m^{-2} (blue).

In short conclusion for this section, we can state that the conversion process for a 100 nm thick TMSC layer works best at doses between 0.3 C.m^{-2} and 1 C.m^{-2} for primary electron energies of 2 keV. The specific finding in this thesis, however, were the indices that the conversion process reveals a vertical gradient, which stems from the interaction volume related electron density gradient in Z. Although the subsequent TMSC removal experiments were not successful, these findings clearly form the base for a future thesis in which electron energies will be gradually increased to achieve higher conformity within the TMSC layer. This is expected to enable both, a clear detection of the ideal doses and an increased vertical homogeneity of the conversion process. The washing experiments also indicate another conversion process reflected by the TMSC remaining on the surface. Nevertheless, this study gives first fundamental insight, indispensably needed for further progress in the area of FEBIC.

5 Conclusion and Outlook

The overall aim of this master thesis was to study specific protein interactions on cellulose surfaces. Two main approaches were chosen to perform this task. As basis, cellulose thin films were produced by spin coating a soluble cellulose derivative (TMSC) followed by regeneration to cellulose. The latter was performed for the whole substrate via exposure to acidic HCl vapour and locally by the exposure to a focused electron beam. To ensure covalent bonding of the proteins on the surface, a chemical multi-layer system was introduced on top of globally / locally regenerated thin films by incubating with another cellulose derivative (CMC) and subsequent immobilization of EDC/NHS. This enabled the controlled bonding of BSA and investigation of the interacting behaviour with the counter protein anti-BSA. Every single functionalization step was monitored via different measurement techniques to gain comprehensive insights in film formation and surface functionality.

Static contact angle measurements indicated chemical changes on the surfaces after every incubation step. Obtained static contact angles for TMSC were in accordance with reported values. The unusually high contact angles for regenerated cellulose hint to a certain amount of crystallinity in the produced cellulose structures. CMC, EDC / NHS and BSA resulted in low contact angles as expected. The surfaces exposed to anti-BSA resulted in higher contact angles. For this layer, we observed partly strong contact angle variations for different samples and even at different sites on identical samples, which indicates a strong preparation dependency. This suggests an inhomogeneous protein distribution on the surface, which was further substantiated by AFM measurements, revealing high surface roughness with strong variations from sample to sample and from site to site. Confinement in preparation protocols led to acceptable homogeneity in film formation for further experiments.

ATR-IR spectroscopy after every incubation step confirmed successful regeneration from TMSC to cellulose. A clear indication for the presence of CMC and EDC / NHS was not possible, which suggested the formation of a very thin surface film, not detectable by this method. Complementary data from other techniques finally confirmed this assumption. In contrast, both proteins could be detected on the surfaces as intended, which indirectly confirms the adsorption of CMC and EDC / NHS as they were required for bonding from a chemical point of view.

Surface plasmon resonance was used to quantitatively measure adsorption in every step. BSA adsorption on untreated cellulose was limited. Adsorption of BSA on CMC was reproducibly confirmed. The introduction of the immobilization molecules led to a moderately increase of surface concentration of BSA. Interestingly, anti-BSA adsorbed/bonded in high amounts, compared to the other molecules.

Atomic force microscopy was used to complement these findings with morphological and functional information via height and phase imaging, respectively. Primary investigations of the arrangement and swelling behaviour of TMSC and cellulose micro fibrils in liquid environment suggested a certain amount of crystallinity within the structure, which was consistent with the contact angle measurements. Furthermore, the obtained topological results strongly suggested successful CMC, EDC / NHS and BSA adsorption as a clear difference was found. Even though BSA led to complicated and unwanted interactions between tip and sample, the permanent remaining of the proteins on the same place, even after multiple scans, further indicated irreversible covalent bonding between the protein and the functionalized surface.

Overall, a protocol to successful protein BSA immobilization onto a cellulose thin film was developed, substantiated by multi-technique characterization approaches for comprehensive and consistent insights in film formation and surface properties.

In the second part, the focus lied on the possibility of local TMSC conversion in cellulose by utilizing a focused electron beam. Initial patterning experiments were performed on TMSC films spin cast from chloroform solutions. The height loss, which reportedly accompanies the conversion process, was evaluated with AFM and found to be in agreement with literature. Such locally converted films were then exposed to highly specific cellulase solutions for indirect proof of a successful conversion into cellulose, reflected by further height losses. In this first run, however, the high surface roughness of chloroform based TMSC films prevented reliable analyses. Nevertheless, it was proven, that the height loss is dose dependent up to a value around 1.4 $C.m^{-2}$, were over-conversion led to other, undefined carbon structures. Investigations regarding the production of a smoother TMSC film led to dissolution of TMSC in xylene instead of chloroform, resulting in a more favourable nominal RMS surface roughness. Systematic AFM measurements before and after cellulase exposure for electron beam processed patterns showed a clear trend. Not only was it proven that the FEBIC treatment worked as initially intended, but also dose ranges regarding the amount of converted cellulose were identified, consistent with the previous measurement. At low doses, up to 0.3 Cm^{-2} no or only partially converted cellulose was found. The ideal dose was found between 0.3 $C.m^{-2}$ and 1.4 $C.m^{-2}$, while higher doses clearly led to over-conversion. Characteristic spectra of TMSC and cellulose were exploited to further investigate the conversion in the individual areas. ATR-IR and Raman spectroscopy of the pads revealed the presence of signature vibration bands of TMSC as well as bands corresponding to over converted material, over a broad range of doses. This led to the idea of an inhomogeneous conversion in vertical direction (along Z). This vertical conversion gradient was attributed to the interaction volume of the electrons and the effect of backscattered electrons, resulting in regions of under- ideally- and over converted cellulose along the Z-axis. With this hypothesis, it was possible to correlate the height loss rate with the doses, narrowing the region of the ideal dose down being between 0.3 $C.m^{-2}$ and 1.0 $C.m^{-2}$. As this aspect was not considered in previous activities, the here presented findings represent an important step forward in the fundamental understanding.

Future research aiming to deepen the understanding of cellulose structured by electrons could contain a detailed inspection of the systems behaviour at higher primary electron energies. This is expected to reduce the effect of the vertical conversion gradient. Furthermore, an improved investigation of infrared spectra corresponding to the different doses could enhance the understanding of the actually formed structures in the case of over-conversion. Once vertically homogenous conversion is achieved, similar immobilization steps, as described above, could be implemented on small structured cellulose. The patterning would be followed by washing of the remaining TMSC and by performing the already known incubation steps and techniques, introducing a highly versatile basis for bio sensors on the micro scale, as protein adsorption sites could be designed with a high degree of spatial control.

6 References

[1] M. Schaub, G. Wenz, G. Wegner, A. Stein, D. Klemm, *Adv. Mater.* 1993, *5*, 919.

[2] © Harald Plank, Institute of Electron Microscopy and Nanoanalysis TU Graz 2019.

[3] *https://www.kruss-scientific.com/de/service/schulung-theorie/glossar/kontaktwinkel/; ©A.KRÜSS Optronic GmbH*.

[4] D. K. Owens, R. C. Wendt, *J. Appl. Polym. Sci.* 1969, *13*, 1741.

[5] A. C. O'SULLIVAN, *Cellulose* 1997, *4*, 173.

[6] D. Klemm, B. Heublein, H.-P. Fink, A. Bohn, *Angewandte Chemie (International ed. in English)* 2005, *44*, 3358.

[7] M. Mhd Haniffa, Y. Ching, L. Abdullah, S. Poh, C. Chuah, *Polymers* 2016, *8*, 246.

[8] E. Kontturi, P. C. Thüne, J. W. Niemantsverdriet, *Polymer* 2003, *44*, 3621.

[9] R. Kargl, T. Mohan, M. Bračič, M. Kulterer, A. Doliška, K. Stana-Kleinschek, V. Ribitsch, *Langmuir the ACS journal of surfaces and colloids* 2012, *28*, 11440.

[10] S. N. Timasheff, G. D. Fasman, *Structure and stability of biological macromolecules*, Dekker 1969.

[11] R. Jain, D. Calderon, P. R. Kierski, M. J. Schurr, C. J. Czuprynski, C. J. Murphy, J. F. McAnulty, N. L. Abbott, *Analytical chemistry* 2014, *86*, 3764.

[12] B. Friedrichs, *Nahrung* 1997, *41*, 382.

[13] N. Kossovsky, A. Nguyen, K. Sukiassians, A. Festekjian, A. Gelman, E. Sponsler, *Journal of Colloid and Interface Science* 1994, *166*, 350.

[14] Matthew Zimmerman, Marek Grabowski, Wladek Minor, Helen M. Berman, Margaret J. Gabanyi, Robert Lowe, Raship Shah, Wendy Yi-Ping Tao, John D. Westbrook, Protein Structure Initiative network of investigators, *Protein Structure Initiative Publications, 2000-2016*, Zenodo.

[15] C. Puttharugsa, T. Wangkam, N. Houngkamhang, S. Yodmongkol, O. Gajanandana, O. Himananto, B. Sutapun, R. Amarit, A. Somboonkaew, T. Srikhirin, *Current Applied Physics* 2013, *13*, 1008.

[16] M. Rabe, D. Verdes, S. Seeger, *Advances in colloid and interface science* 2011, *162*, 87.

[17] T. Mohan, S. Spirk, R. Kargl, A. Doliška, A. Vesel, I. Salzmann, R. Resel, V. Ribitsch, K. Stana-Kleinschek, *Soft Matter* 2012, *8*, 9807.

[18] T. Ganner, J. Sattelkow, B. Rumpf, M. Eibinger, D. Reishofer, R. Winkler, B. Nidetzky, S. Spirk, H. Plank, *Scientific reports* 2016, *6*, 32451.

[19] H. Orelma, T. Teerinen, L.-S. Johansson, S. Holappa, J. Laine, *Biomacromolecules* 2012, *13*, 1051.

[20] D. Breitwieser, S. Spirk, H. Fasl, H. M. A. Ehmann, A. Chemelli, V. E. Reichel, C. Gspan, K. Stana-Kleinschek, V. Ribitsch, *J. Mater. Chem. B* 2013, *1*, 2022.

[21] N. J. d. Mol, M. J.E. Fischer (Eds.), *Surface Plasmon Resonance: Methods and Protocols*, Humana Press, Totowa 2010.

[22] R. B. M. Schasfoort, *Handbook of Surface Plasmon Resonance*, Royal Society of Chemistry, Cambridge 2017.

[23] J. R. Sambles, *Journal of Physics and Chemistry of Solids* 1989, *50*, 1.

[24] *http://www.bionavis.com/en/life-science/technology/; ©2019 Bionavis*.

[25] J. A. de Feijter, J. Benjamins, F. A. Veer, *Biopolymers* 1978, *17*, 1759.

[26] T. Mohan, K. Niegelhell, C. S. P. Zarth, R. Kargl, S. Köstler, V. Ribitsch, T. Heinze, S. Spirk, K. Stana-Kleinschek, *Biomacromolecules* 2014, *15*, 3931.

[27] S. Strasser, K. Niegelhell, M. Kaschowitz, S. Markus, R. Kargl, K. Stana-Kleinschek, C. Slugovc, T. Mohan, S. Spirk, *Biomacromolecules* 2016, *17*, 1083.

[28] A. Theisen, *Refractive increment data-book for polymer and biomolecular scientists*, Nottingham University Press, Nottingham 2000.

[29] K. Niegelhell, M. Süßenbacher, J. Sattelkow, H. Plank, Y. Wang, K. Zhang, S. Spirk, *Biomacromolecules* 2017, *18*, 4224.

[30] T. Tumolo, L. Angnes, M. S. Baptista, *Analytical biochemistry* 2004, *333*, 273.

[31] *http://www.gel.usherbrooke.ca/casino/index.html; Dominique Drouin, Ph.D., B. Ing; Université de Sherbrooke*.

[32] *https://www.brukerafmprobes.com/p-3759-fastscan-a.aspx; ©2019 Bruker Nano Inc.*

[33] *https://www.brukerafmprobes.com/p-3816-fastscan-d.aspx; ©2019 Bruker Nano Inc.*

[34] J. D. Adams, B. W. Erickson, J. Grossenbacher, J. Brugger, A. Nievergelt, G. E. Fantner, *Nature nanotechnology* 2016, *11*, 147.

[35] R. Garcia, *Amplitude Modulation Atomic Force Microscopy*, Wiley-VCH, s.l. 2011.

[36] A. M. Baró, R. G. Reifenberger, *Atomic force microscopy in liquid: Biological applications*, Wiley-VCH, Weinheim, Germany 2012.

[37] Y. Nishiyama, P. Langan, H. Chanzy, *J. Am. Chem. Soc.* 2002, *124*, 9074.

[38] T. Tammelin, R. Abburi, M. Gestranius, C. Laine, H. Setälä, M. Österberg, *Soft Matter* 2015, *11*, 4273.

[39] J. George, S. N. Sabapathi, *Nanotechnology, science and applications* 2015, *8*, 45.

[40] R. Kargl, T. Mohan, S. Köstler, S. Spirk, A. Doliška, K. Stana-Kleinschek, V. Ribitsch, *Adv. Funct. Mater.* 2013, *23*, 308.

[41] S. Köhler, T. Liebert, T. Heinze, *J. Polym. Sci. A Polym. Chem.* 2008, *46*, 4070.

[42] *https://spectrabase.com/spectrum/GCfuNCaAZkn; SpectraBase™*.

[43] D. R. Biswal, R. P. Singh, *Carbohydrate Polymers* 2004, *57*, 379.

[44] Y. Zu, Q. Zhao, X. Zhao, S. Zu, L. Meng, *International journal of nanomedicine* 2011, *6*, 3429.

[45] *https://www.coriolis-pharma.com/contract-analytical-services/fourier-transform-infrared-(ftir)-spectroscopy/; © 2019 Coriolis Pharma*.

[46] H. Orelma, I. Filpponen, L.-S. Johansson, J. Laine, O. J. Rojas, *Biomacromolecules* 2011, *12*, 4311.

[47] T. Eastman, D.-M. Zhu, *Langmuir* 1996, *12*, 2859.

[48] S. S. Wong, E. Joselevich, A. T. Woolley, C. L. Cheung, C. M. Lieber, *Nature* 1998, *394*, 52 EP -.

[49] R. D. Piner, S. Hong, C. A. Mirkin, *Langmuir* 1999, *15*, 5457.

[50] P. J. Larkin, *Infrared and Raman spectroscopy: Principles and spectral interpretation*, Elsevier professional, s.l. 2011.

[51] D. Lin-Vien, N. B. Colthup, W. G. Fateley, J. G. Grasselli, *The handbook of infrared and Raman characteristic frequencies of organic molecules*, Elsevier 1991.